The tracker in the trigger of LHCb

Hommels, L.B.A.

Publication date
2006
Document Version
Final published version

The Tracker in the Trigger of LHCb

The Tracker in the Trigger of LHCb

ACADEMISCH PROEFSCHRIFT

ter verkrijging van de graad van doctor
aan de Universiteit van Amsterdam
op gezag van de Rector Magnificus
prof. mr. P.F. van der Heijden
ten overstaan van een door het college voor promoties
ingestelde commissie, in het openbaar te verdedigen
in de Aula der Universiteit
op woensdag 18 oktober 2006, te 14.00 uur

door

Leonard Bart Anton Hommels

geboren te Rotterdam.

Promotor: prof.dr. M.H.M. Merk
Co-promotor: dr. N. Tuning

Faculteit der Natuurwetenschappen, Wiskunde en Informatica

ISBN: 978-0-9553948-0-5
Published by: L.B.A. Hommels
Printed by: Cambridge Printing, Cambridge

The work described in this thesis is part of the research program of 'het Nationaal Instituut voor Kernfysica en Hoge-Energiefysica' (NIKHEF) in Amsterdam, the Netherlands. The author was financially supported by the 'Stichting Fundamenteel Onderzoek der Materie' (FOM).

Contents

Introduction

Of the elementary particles known today, the electron was discovered first, by Thomson in 1897. The existence of its anti-particle, the positron, was predicted from theory by Dirac in 1928, and experimentally confirmed by Anderson in 1932. Ever since, research is conducted to look for fundamental differences between the laws of physics for matter and anti-matter.

From observations, the Universe appears to be matter dominated. To explain the absence of antimatter, in 1967 Sakharov posed three requirements, one of which is the violation of charge-parity (CP) symmetry. In 1964, CP symmetry violating effects were observed in the decay of neutral K mesons. More recently, CP violation in the B meson system is observed.

B mesons will be produced in abundance at the Large Hadron Collider (LHC), a circular proton-proton collider which is currently being constructed at CERN in Geneva, Switzerland. Benefiting from the possibility to study B mesons with high statistics, the LHCb experiment aims to measure CP violating effects in B meson decays with unprecedented precision.

The high rate of proton-proton collisions at the LHC, and the low cross-section for B meson production demands for an efficient separation of events containing a B meson decay and background events. A multistage on-line triggering system is deployed to select events containing a B decay and reduce the initial data output of the experiment to a rate at which event data can be written to mass storage devices for off-line analysis.

Events containing the decay of a B meson are selected on two main characteristics: a relatively long lifetime and high mass. The B meson lifetime is extracted from the distance between the production and decay vertices, using a precise tracking detector surrounding the primary interaction point. For a proper reconstruction of the B meson mass, and thus an efficient rejection of background events, the momentum of its decay particles must be measured with high precision.

To obtain the best estimate on the momentum of a particle, its trajectory is reconstructed before and after it traverses the magnetic field by using the main tracker detectors. Triggering algorithms use momentum information; including main tracker data in triggering algorithms improves their performance. In this thesis, particular

attention is paid to the detector covering the larger part of the main tracking detectors, the Outer Tracker (OT). The detector requirements, construction and readout are presented, and the feasibility of reading the detector data for use in the trigger is discussed.

The remainder of this thesis is subdivided in the following chapters:
Chapter 1 reviews the main properties used to distinguish B decay events from background events. Of four benchmark B meson decay channels, the event signature and its selection is discussed in more detail.

Chapter 2 describes the LHC and the properties of the interaction point where the LHCb experiment is situated. The subdetectors of LHCb are presented individually, as well as the layout of the readout electronics and data acquisition system.

Chapter 3 focuses on the Outer Tracker subdetector. The requirements and the consequences for the OT design are presented. Thereafter, the detector technology is discussed: the working principles and properties of gas-filled straw tubes are described. The chapter concludes with a presentation of the overall detector design and construction.

Chapter 4 contains a description of the Outer Tracker readout. Firstly, the properties of the detector channels are presented. Secondly, the interface of the detector channels with the front-end electronics is described. Thirdly, the repercussions of the channel properties and the implementation of the readout system for the physics performance of the detector is discussed. Finally, the readout stage performing the signal digitisation and readout is presented.

Chapter 5 discusses an algorithm for online reconstruction of particle trajectories, from which the momentum is estimated, using the Inner Tracker and Outer Tracker detectors. The working principles, implementation and possible applications are explained. Finally, the performance of the algorithm is illustrated by using it to find continuations in the main tracker stations of track segments reconstructed in the vertex and muon subdetectors.

Chapter 6 shows the application of the online tracking algorithm in Level-1 triggering algorithms in LHCb. Both the application in an exclusive trigger as well as an inclusive muon trigger are discussed. Finally, the last section summaries the trigger performance for the benchmark channels and draws conclusions on the use of the online tracking algorithms in the LHCb trigger.

Chapter 1

LHCb: B Meson Decay Measurement

The Standard Model provides an accurate description of the elementary particles and their interactions. It accommodates fermions and bosons, of which the bosons mediate the interactions between the fermions: gluons (g) for the strong force, photons (γ) for the electromagnetic force and the Z^0 and $W^{\pm}$ bosons for the weak force.

The fermions are subdivided in two types: leptons and quarks. All fermions are susceptible to the electromagnetic and weak force; the quarks, additionally, to the strong force. Each type consists of three generations with increasing mass, each generation in its turn contains both fermion types. In total, the Standard Model comprises charged leptons and uncharged neutrinos of the electron (e), muon (μ) and tau (τ) type. Six quark flavours exist, ranging from light to heavy: up, down, strange, charm, bottom and top, abbreviated as u, d, s, c, b, and t. The d, s, b quarks, carrying -$\frac{1}{3}$ unit charge, are of the down-type, whereas the up-type consist of the $+\frac{2}{3}$ charged quarks u, c, and t. For each fermion, an antiparticle with opposite charge exists.

This thesis is focused on the detection of (anti-)B mesons, since several B decays are well suited to measure CP violation, a phenomenon that distinguishes matter from anti-matter. Mesons are composed of two quarks; in B mesons, one of the quarks is of the b or anti-b ($\overline{b}$) flavour.

Following the initial observation of the dimuon decay of $\Upsilon(b\overline{b})$ mesons by the E0288 collaboration at Fermilab [1], the lifetime of mesons containing a b quark was measured by the MAC [2] and MARK II [3] collaborations. In contrast to the expectations at that time, the lifetime proved to be relatively long. In retrospect, the B meson lifetime is understood from the small amplitude for a b quark to decay to the quark with the next lower mass, the c quark. In Table 1.1, the lifetimes and masses for the various B mesons are listed.

The long lifetime of the B meson is what makes it particularly suitable to study CP-violation. During their lifetime, the apparent mixing of neutral B mesons, first observed by the ARGUS [4] collaboration, provides an opportunity for measurement of parameters relevant to CP violation. Manifestations of CP violation can be subdivided

in the following ways:

- *CP violation in decay.* Occurring both in neutral and charged meson decays, CP violation parameters are extracted from the different magnitudes of the amplitudes for a B decay and its CP conjugate process: $A(B \to f) \neq \overline{A}(\overline{B} \to \overline{f})$.

- *CP violation in mixing.* Here, CP violation is observed from the asymmetry in the oscillation probabilities for $B^0 \to \overline{B}^0$ and $\overline{B}^0 \to B^0$ (or, equally, for B_s^0). In contrast to the Kaon system where CP violation was first observed, theoretical expectations indicate that CP violation in mixing in the B system is very small, in the order $\mathcal{O}(10^{-2})$ [5].

- *CP violation in interference.* Apart from the CP violation in the schemes mentioned above, it can occur in the interference between decay ($B \to f$) amplitudes and mixed decay ($B \to \overline{B} \to f$) amplitudes. If these amplitudes have a different phase for the B and $\overline{B}$ decays, CP violation due to interference occurs.

From the latter method, CP violating effects are already measured by the BABAR [6] and BELLE [7] experiments from comparison of the B^0 and the oscillated $\overline{B}^0$ decaying into the J/ψ K_S^0 final state. Also, CP violation in decay has been observed by these experiments, for example by comparing the amplitude of the $B^0 \to K^+\pi^-$ decay and its CP conjugated decay: $\overline{B}^0 \to K^-\pi^+$ [8, 9].

In the experiments mentioned above, B mesons are produced from e^+e^- collisions with a centre-of-mass energy tuned to the $\Upsilon(4S)$ resonance. From the produced $b\overline{b}$ pair, coherent pairs of B^0 and $\overline{B}^0$, or B^+ and B^- mesons are formed in equal amounts. The LHCb experiment is situated at the LHC, a proton-proton collider. Here, many non-coherent B hadrons are produced. LHCb is geared for a precision measurement of CP violating effects in the decay of charged, and both neutral B^0 ($\overline{B}^0$) and B_s^0 ($\overline{B}_s^0$) mesons. The various B mesons and their quark composition are listed in Table 1.1.

B meson	Quark Content	Mass (MeV)	Lifetime (ps)	Production Fraction
B_u	$\overline{b}\ u$	5279.0±0.5	1.674±0.018	40%
B_d	$\overline{b}\ d$	5279.4±0.5	1.542±0.016	40%
B_s	$\overline{b}\ s$	5369.6±2.4	1.461±0.057	12%
B_c	$\overline{b}\ c$	6.4±0.4	$0.46^{+0.18}_{-0.16}$±0.03	<0.1%

Table 1.1: B meson quark composition, measured mass, lifetime [5], and production fractions from $\overline{b}$ quarks at LHCb. Identical production fractions are assumed for the charge-conjugated states. b-baryons account for the remaining 8% of the production fraction [10].

1.1 Selection of B Meson Decays at LHCb

In a pp collision, a great variety of hadronic particles are produced. To distinguish B meson decays from other particles produced in an event, use is made of its two main characteristics: the large mass and long lifetime. This thesis focuses on trigger systems for the online selection of B decay containing events.

1.1.1 B Meson Production Rate

The total sample of events resulting from inelastic pp collisions are referred to as the minimum-bias sample. The cross sections for all inelastic processes and for $b\bar{b}$ production in pp collisions at beam energies of the LHC (see Section 2.1) are expected to rate 160 to 1. Taking into account the luminosity and interaction rate, a 100 kHz $b\bar{b}$ pair production rate is expected. The production ratios of the various B hadrons from $\bar{b}$ quarks are listed in Table 1.1.

For $b\bar{b}$ production at the LHC, the angular distribution of the b and $\bar{b}$ hadrons is strongly correlated and is expected to peak in the forward directions, as is seen from the histogram in Fig. 1.1. For a large coverage at a moderate cost, the LHCb experiment, described in more detail in the next chapter, is designed as a single-arm spectrometer. Of all $b\bar{b}$ events, 15.1% have both b-hadrons in the LHCb acceptance [11]. Minimum-bias events without B meson decays in the acceptance are considered background and must be rejected.

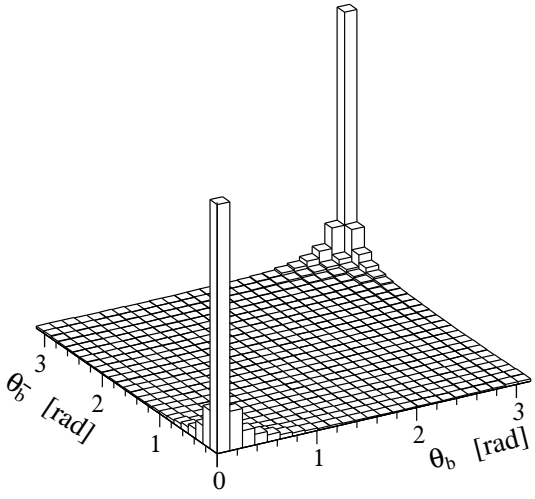

Figure 1.1: Distribution of the polar angles (θ) of simulated production of b and $\bar{b}$ hadrons at the LHC, from Ref. [10].

The branching fractions of the B decay channels which are vital to the measurement of CP violation are tiny, typically in the order of $\mathcal{O}(10^{-4} - 10^{-5})$. For a high precision measurement of CP violating effects, these B decays must be efficiently selected over background events to minimise the statistical uncertainties.

1.1.2 Identification of B Decays

The B meson mass is low compared to the 7 TeV nominal energy of the colliding protons at the LHC. As a result, B mesons have a large boost, of $\beta\gamma \simeq 15$, and propagate mainly along the beamline. Due to its long lifetime, the decay of the B meson takes place at considerable distance from its production vertex, up to a few cm. Ref. [5] lists over 400 possible B decay modes. In many of these decays, a large difference between the summed mass of the decay particles and the B meson mass exists, resulting in large opening angles between the decay particles. Combined with the long B lifetime, the decay particles have a large impact parameter (IP) with respect to the production vertex of the B meson. The plotted distribution of the particle IP from simulated B decays is shown in Fig. 1.2.

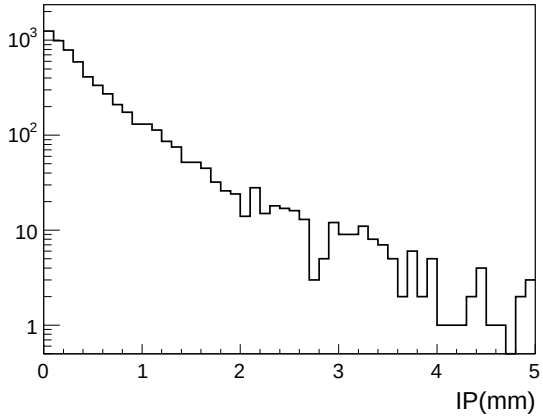

Figure 1.2: Histogram of the impact parameter (IP) of particles originating from simulated generic B decays in the LHCb acceptance.

Fig. 1.3 contains a histogram of the highest particle transverse momentum (p_T) for simulated minimum-bias and $b\bar{b}$ events. The transverse momentum distribution of B decay particles is independent of their IP. Consequently, events containing a B decay are distinguished from background events by tracks with a significant IP and large p_T.

The number of charged particles, or multiplicity, in the LHCb detector acceptance is higher for events containing a B decay than for minimum-bias events, as is shown in the

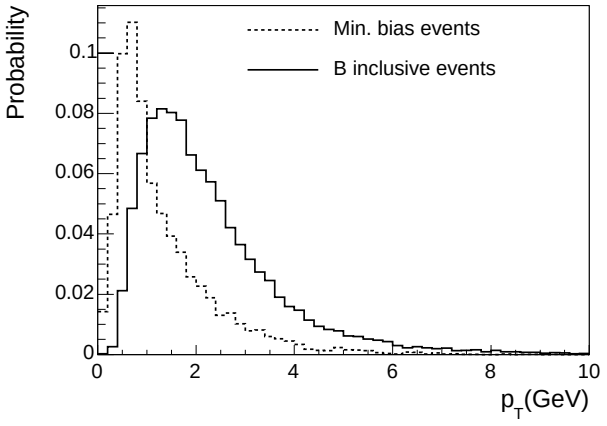

Figure 1.3: Histograms of the highest particle transverse momentum (p_T) for simulated minimum-bias and $b\bar{b}$ containing events.

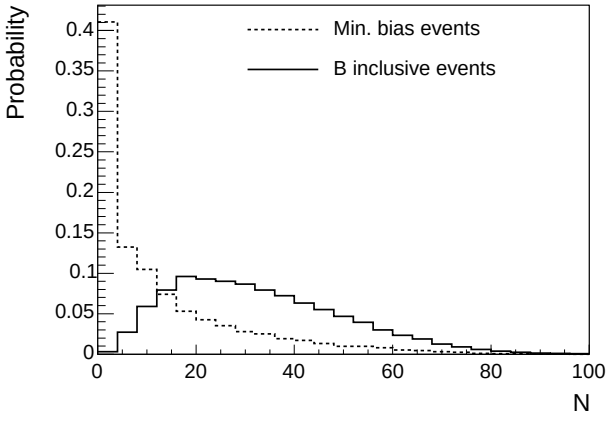

Figure 1.4: Histograms of the charged particle multiplicity (N) in the LHCb acceptance for simulated minimum-bias and $b\bar{b}$ containing events.

histograms in Fig. 1.4. To properly select the B decay particles from the total particle count in the detector, a high track reconstruction efficiency is mandatory.

1.2 Properties of Benchmark B Decay Channels

To evaluate the trigger capabilities of LHCb in Chapter 6, four benchmark B decay channels presented in the following section are used. For each decay, the main characteristics used for its selection are discussed and the annual event yield is calculated.

$B^0 \rightarrow J/\psi(\mu^+\mu^-)K^0_S$

In the $B^0 \rightarrow J/\psi K^0_S$ decay, both the B^0 and $\overline{B}^0$ can decay to the same final state: a CP eigenstate. This allows for a straightforward extraction of parameters relevant to CP violation from two decay rates. Therefore, this decay is the prime channel used by BABAR and BELLE for the measurement of the CP violation parameter $\sin(2\beta)$ [6,12].

In the LHCb experiment, muon identification is relatively straightforward. By reconstruction of the J/ψ invariant mass from a $\mu^+\mu^-$ pair, $B^0 \rightarrow J/\psi(\mu\mu)X$ inclusive decays are efficiently selected. The high J/ψ mass of 3097 MeV, and its narrow decay width below 0.1 MeV are instrumental in the rejection of background events containing two muons. K^0_S particles are reconstructed from their main decay channel $K^0_S \rightarrow \pi^+\pi^-$. The total and partial branching fractions for the $B^0 \rightarrow J/\psi(\mu^+\mu^-)K^0_S(\pi^+\pi^-)$ decay are listed in Table 1.2.

Decay	Branching Fraction
$B^0 \rightarrow J/\psi K^0$	$8.7\pm0.5\times10^{-4}$
$B^0 \rightarrow J/\psi K^0_S$	$4.4\pm0.3\times10^{-4}$
$B^0 \rightarrow J/\psi(\mu^+\mu^-)K^0_S$	$2.6\pm0.3\times10^{-5}$
$B^0 \rightarrow J/\psi(\mu^+\mu^-)K^0_S(\pi^+\pi^-)$	$1.8\pm0.3\times10^{-5}$

Table 1.2: Branching fractions for the $B^0 \rightarrow J/\psi(\mu^+\mu^-)K^0_S(\pi^+\pi^-)$ decay.

The total efficiency for a decay channel ϵ_{tot} is established from multiplication of the partial efficiencies:

$$\epsilon_{\text{tot}} = \epsilon_{\text{det}} \times \epsilon_{\text{rec/det}} \times \epsilon_{\text{sel/rec}} \times \epsilon_{\text{trg/sel}}. \tag{1.1}$$

Where ϵ_{det} is the percentage of B decays of which all decay products are reconstructible taking the LHCb acceptance into account, and $\epsilon_{\text{rec/det}}$ is the efficiency that these decay products are actually reconstructed. $\epsilon_{\text{sel/rec}}$ is the efficiency that the event is selected offline, and $\epsilon_{\text{trg/sel}}$ corresponds to the trigger efficiencies of the L0 and L1 trigger. Table 1.3 contains the partial and total efficiencies for three benchmark decay channels.

For the $B^0 \rightarrow J/\psi(\mu^+\mu^-)K^0_S$ channel, ϵ_{tot}= 1.39%. Multiplication of the efficiency with the branching fraction and the 80 kHz total rate at which B^0 and $\overline{B}^0$ are produced from $b\bar{b}$ events, results in an annual ($10^7 s$) yield of 220k events.

To observe CP violation with these events, the B meson state at the time of its production must be correctly identified, or 'tagged'. The tagging efficiency for $B^0 \rightarrow J/\psi(\mu^+\mu^-)K^0_S$ events accounts 45.1±1.3% [13]. However the rate of mis-tagged events

Decay Channel	ϵ_{det}	$\epsilon_{\text{rec/det}}$	$\epsilon_{\text{sel/rec}}$	$\epsilon_{\text{trg/sel}}$	ϵ_{tot}
$B^0 \to J/\psi(\mu^+\mu^-)K^0_S$	6.5	66.5	53.5	60.5	1.39
$B^0_s \to D^\mp_s K^\pm$	5.4	82.0	20.6	29.5	0.269
$B^0 \to \mu^+\mu^- K^*$	7.2	82.4	16.1	73.5	0.704

Table 1.3: Total efficiency ϵ_{tot} and the breakdown of its components for three of the benchmark B decay channels. All efficiency numbers are quoted in percentages (%) and are taken from Ref. [13].

($\omega = 36.7 \pm 1.9\%$) limits the statistical power of the collected event sample to the equivalent of 7k perfectly tagged events per year.

It is expected that the resulting statistical errors on the CP violation parameter $\sin(2\beta)$ extracted from the event sample acquired in one year of data-taking are comparable to the errors from the 5k events used for the determination of $\sin(2\beta)$ by the BaBar collaboration [14]. Besides an accurate determination of CP violation parameters, this channel is valuable to provide a benchmark of the LHCb performance and systematics against the established performance figures of the B factories.

$B^0_s \to D^\mp_s K^\pm$

The final state of the $B^0_s \to D^\mp_s K^\pm$ decay is not a CP eigenstate. Although both the B^0 and $\overline{B}^0$ can decay to the same final state, the decay processes are not invariant under CP conjugation. This gives rise to four distinct decay amplitudes, from which the CP violation parameter $\gamma - 2\chi$ can be extracted [15]. The decay amplitudes of B^0_s or $\overline{B}^0_s$ into $D^-_s\ K^+$ are expected to be of the same order of magnitude, allowing for a precise measurement of CP violating effects.

LHCb is unique in the ability to access this decay mode. The final state consists of multiple hadrons sharing the transverse energies from the B decay, making the selection of these decays over background events particularly challenging. As a result, the efficiencies quoted in Table 1.3 for this channel are low compared to other benchmark decays. Multiplication of the total efficiency with the total B^0_s and $\overline{B}^0_s$ production rate of 24 kHz and the branching fraction of 1×10^{-5}, results in an annual yield of 5.4k events.

The tagging power for B^0_s mesons is estimated to be higher than for B^0 mesons [13]: for a B^0_s, a same-side Kaon provides an additional tagging possibility compared to B^0 tagging. As a result, the annual $B^0_s \to D^\mp_s K^\pm$ yield is equivalent with 350 perfectly tagged events per year.

For a proper extraction of CP violation parameters from $B^0_s \to D^\mp_s K^\pm$ events, care must be taken that the decay selection is not polluted with mis-identified $B^0_s \to D^\mp_s \pi^\pm$ events. For the nontrivial task of separating $\pi^\pm$ from $K^\pm$ particles, the LHCb experiment comprises dedicated particle identification systems, described in Section 2.6.

For leptons, and particularly muons, the particle identification is more straightforward. By triggering on a muon, an efficient tag is obtained without biasing the selection. The high-multiplicity, hadronic $B^0_s \to D^\mp_s K^\pm$ decay is used as an example to determine

the efficiency of a muon trigger presented in Chapter 6. Here, no high-p_T muons are expected to originate from the decay of the signal B, hence a trigger on a high-p_T, high IP muon selects semi-leptonic decays of the 'opposite-side' B.

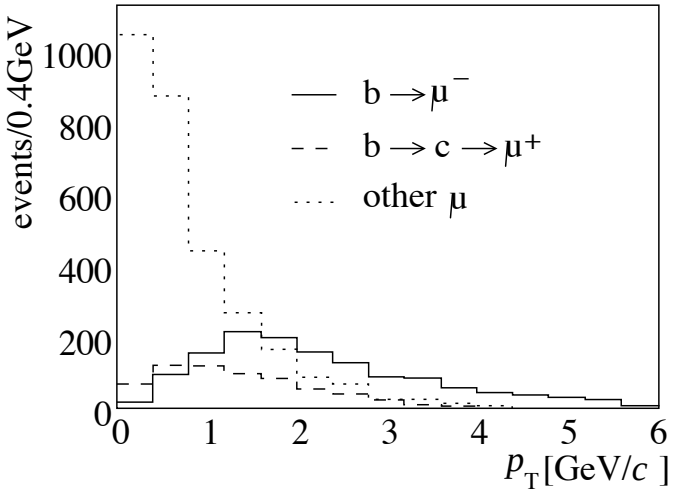

Figure 1.5: p_T distribution for opposite-side muon tag candidates, with $p > 5\,\text{GeV}$, from Ref. [13].

The branching fraction of $B \to \mu X$ is about 10%. The main background of high-IP, high-p_T muons stems from the $B \to D \to \mu$ decay chain. Compared to muons from semileptonic B decays, muons from D decays carry an opposite charge. Using these muons accidentally for B tagging would yield an incorrect tag, therefore they must be rejected. In Fig. 1.5, the p_T of opposite-side muon tag candidates is plotted. As is seen from the plot, above 2 GeV the dominant fraction of the muons are originating from B decays.

The selection of $B_s^0 \to D_s^{\mp} K^{\pm}$ events from a high-p_T muon inside the acceptance, originating from the decay of the opposite-side B has a low overall efficiency and thus a meagre event yield. It is used as a benchmark for the performance of a single-muon trigger, presented in Section 6.3.3.

$B_s^0 \to \mu^+\mu^-$

Besides the unambiguous measurement of CP violation parameters, the LHCb experiment is dedicated to the measurement of 'rare decays' of the B meson. The $B_s^0 \to \mu^+\mu^-$ branching ratio predicted from the standard model accounts 3.9×10^{-9} [16], an experimental upper limit is determined at 2×10^{-7} [17], with preliminary results indicating a reduction by a factor 2 [18]. Concurrent decay diagrams involving yet undiscovered

particles can enhance the branching fraction up to two orders of magnitude, making this particular channel a very sensitive probe for physics beyond the Standard Model.

The foreseen annual event yield is calculated similarly to the two decay channels mentioned previously. Since no dedicated efficiency study has been carried out yet for this channel, the total efficiency is estimated from the partial efficiencies from B decay channels with similar topology, and is assumed at 1.4%

Using the Standard Model branching ratio, the expected annual yield is approximately 13 events. According to recent studies [16], background events are not negligible due the low event yield of this channel. However, a reliable estimation of the background at branching ratios of $\mathcal{O}(10^{-10})$ is difficult due to the limited amount of simulated events.

$B^0 \to \mu^+\mu^- K^*$

The branching fraction of this rare decay is $(1.3 \pm 0.4) \times 10^{-6}$. The decay topology with the accordingly small branching ratio make this decay sensitive to processes involving physics beyond the standard model. The invariant mass spectrum from the dimuon covers a large range due to the decay kinematics. Aside from an enhancement of the branching fraction, deviations between the observed dimuon invariant mass spectrum and its standard model prediction are a probe for new physics processes [19].

The upper limit on the dimuon mass is given by the 4.4 GeV mass difference between the B^0 and the K^*. The predicted dimuon invariant mass spectrum is plotted in Fig. 1.6, taking into account short-distance and long-distance effects according to various theoretical models. The apparent peaks in the spectrum originate from long-distance effects and are attributed to resonances corresponding to J/ψ and ψ particles.

The dimuon invariant mass provides a handle to efficiently select these events: by the requirement of a positive IP of the muon tracks, dimuons from B decays are selected over dimuons originating from Drell-Yan processes. To suppress the large background from $B^0 \to J/\psi\,(\mu\mu)X$ decays, a range around the J/ψ mass is excluded from the selection, resulting in a low overall efficiency of 0.704%, see Table 1.3.

The yield for this decay is obtained by multiplication of the 80 kHz B^0 and $\overline{B}^0$ production rate with the branching fraction and the overall efficiency. The yield strongly depends on the muon trigger efficiency. Currently, an annual accumulation of 4.4k events is expected.

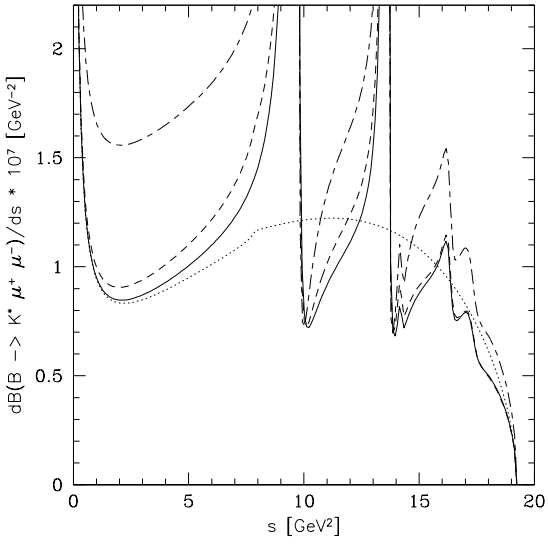

Figure 1.6: Predicted dimuon invariant mass spectrum in $B^0 \to \mu^+\mu^- K^*$ decays, from Ref. [20]. The solid and dashed lines correspond to two independent predictions from the Standard Model, including short and long distance effects. The dotted curve results from Standard Model short-distance effects only. The dash-dotted curve results from a possible new physics scenario, involving supersymmetry.

Chapter 2

The LHCb Experiment

In this chapter, the LHCb experiment [10] is outlined. The first two sections contain a description of the LHC accelerator and the interaction point where LHCb will be situated. Subsequently, the overall layout of the experiment is presented, followed by sections on individual sub-detectors. Finally, the trigger architecture and readout system are discussed.

2.1 The Large Hadron Collider

The Large Hadron Collider (LHC) is currently being built at CERN, Geneva. It will be used to look for physics beyond the standard model, and is due to commence operation in the course of 2007. The LHC is a circular proton-proton (pp) collider of 26.7 km circumference, with two separate beams running in opposite directions [21]. Its design parameters are summarised in Table 2.1. The magnetic field needed to reach the $\sqrt{s}$ =14 TeV centre of mass energy with proton beams is provided by 1232 superconducting dipole magnets.

LHC design parameters		
LHC circumference	26.66	km
Proton beam energy	2×7	TeV
Dipole field	8.3	T
Revolution frequency	11.2	kHz
Bunch crossing frequency	40	MHz
Total number of bunches	3564	
Number of filled bunches	2808	
Number of particles per bunch	1.15×10^{11}	
Nominal Luminosity	1×10^{34}	$\mathrm{cm}^{-2}\mathrm{s}^{-1}$

Table 2.1: Design parameters of the LHC accelerator.

The LHC has four interaction regions indicated with IP1, IP2, IP5, and IP8, occupied by the experiments ATLAS [22], ALICE [23], CMS [24] and LHCb, respectively. In

Fig. 2.1, the arrangement of the experiments around the LHC ring is sketched.

To study physics processes with small cross sections and to perform measurements with high statistical precision, the LHC is designed to deliver a high luminosity of $1{\times}10^{34}\,\mathrm{cm}^{-2}\mathrm{s}^{-1}$.

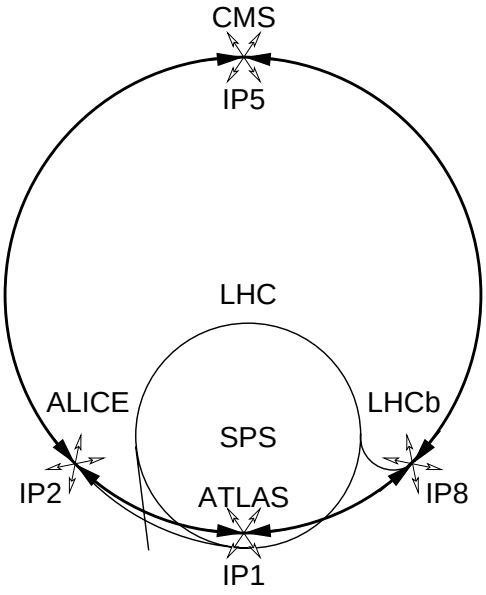

Figure 2.1: Sketch of the LHC accelerator geometry with its interaction points and the location of the main experiments. LHC injection beams are provided by the SPS accelerator.

2.2 Luminosity at the IP8 Interaction Point

The LHC offers an excellent facility to study B-physics since it is a copious source of $b\bar{b}$ quark pairs [25]. For an experiment to measure B meson decay distances, the production and decay vertices need to be correctly identified. This task is simplified when only a single pp collision takes place when two proton bunches cross.

Not all bunches at the LHC are filled with protons. A full LHC cycle contains 3564 bunch slots. However due to the revolution frequency ratios of the synchrotron accelerators generating the LHC injection beams and demands on beam quality [26], only 2808 slots are filled with proton bunches arranged in a bunch structure as shown in Fig. 2.2. Relative to the CMS and ATLAS experiments, the LHC beam at IP8 is 1/8 cycle out of phase due to its location. As a consequence some bunches cross empty bunch slots, and at the IP8 point, the LHC cycle has 2622 bunch crossings with both

bunches filled with protons. For LHCb, the fraction of filled bunch crossings R_{filled} therefore equals $2622/3564 \simeq 0.736$.

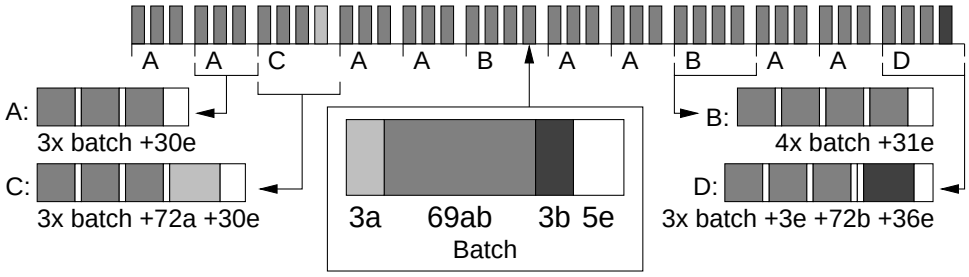

Figure 2.2: LHC bunch structure for one revolution at the IP8 interaction point. Bunch crossings can have two filled (ab) or empty (e) bunches, as well as one filled and one empty bunch (a,b).

In a pp collision with an average of μ interactions, the probability $P(n, \mu)$ of having n interactions is described by a Poisson distribution:

$$P(n, \mu) = \frac{\mu^n}{n!} e^{-\mu}. \tag{2.1}$$

An expression for μ is given by:

$$\mu = \frac{\sigma_{inel}\ \mathcal{L}}{R_{filled}\ f_{LHC}}. \tag{2.2}$$

Where the LHC bunch crossing frequency f_{LHC} is 40 MHz. For the pp inelastic cross section σ_{inel}, 80 mb is assumed. Fig. 2.3 shows the probability for having n inelastic pp interactions in a single bunch crossing as a function of the luminosity $\mathcal{L}$.

The nominal luminosity the LHC is able to deliver exceeds the demands of LHCb. By tuning the beam optics at IP8, the luminosity is adjusted to the needs of the experiment.

The luminosity is primarily limited by the radiation tolerance of the detectors. Taking the detector lifetime into account, a luminosity of $\mathcal{L}= 2\times10^{32}\,\mathrm{cm}^{-2}\mathrm{s}^{-1}$ is determined to be optimal for physics data taking, considering triggering efficiencies and available bandwidth. Although this is the preferred luminosity, the detector, its triggering and data-acquisition systems are designed to operate at $\mathcal{L}= 5\times10^{32}\,\mathrm{cm}^{-2}\mathrm{s}^{-1}$.

At the optimal luminosity, about 1×10^{12} $b\bar{b}$ pairs per year ($10^7 s$) will be produced assuming a $b\bar{b}$ cross-section of 500 μb at $\sqrt{s}$=14 TeV. Even for typical channels relevant for CP measurements, with a branching fractions of the order of $\mathcal{O}(10^{-4} - 10^{-5})$, taking into account an average 1% overall efficiency of the experiment (see [13]), several thousand events per year are selected. In Chapter 1, the branching fractions, reconstruction efficiencies and annual event yields are given for four B decay channels, used as a benchmark throughout this thesis.

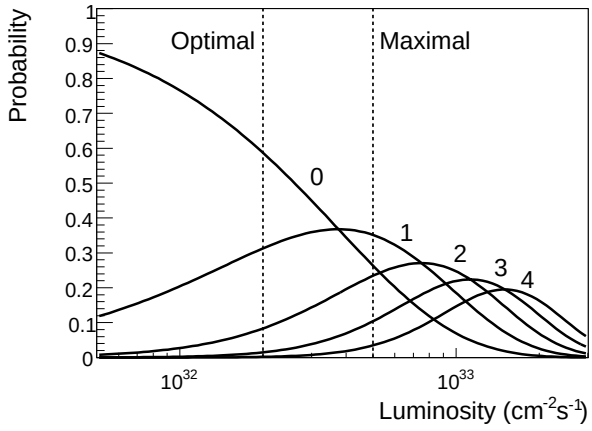

Figure 2.3: Probability curves of having 0, 1, 2, 3 or 4 pp interactions per bunch crossing versus luminosity. Vertical lines indicate the optimal and maximally tolerable luminosities (see text).

2.3 The LHCb Detector Design

The LHCb experiment is optimised to measure CP-violation by studying the B meson system. Since production of $b\bar{b}$ pairs at the LHC will be strongly peaked at small angles with the beamline, LHCb is designed as a single-arm spectrometer. The acceptance covers 15 mrad to 300 (250) mrad in the horizontal (vertical) plane. A cross-section view of the LHCb detector is included in Fig. 2.4.

In LHCb, a right-handed coordinate system is defined with the z-axis along the beamline. The y-axis is defined in upward direction and the x-axis is pointing to the outside of the LHC ring (into Fig. 2.4). The magnetic field of the dipole magnet is oriented along the y axis, therefore the x-z and y-z planes are referred to as the bending and non-bending planes, respectively. The positive and negative z directions are referred to as 'downstream' and 'upstream' respectively.

The design of the LHCb experiment is optimised for $b\bar{b}$ reconstruction:

- To reject the large background of non-$b\bar{b}$ events, the trigger is optimised with respect to speed and efficiency.
- To correctly reconstruct the B mesons, a precise determination of the invariant mass is necessary. Therefore the tracking system is designed for a high momentum resolution of typically $\delta p/p = 0.5\%$.
- To measure B_s oscillations, excellent vertexing and decay-time resolution is required. The vertex locator detector is optimised for this task and has a proper time resolution of 40 fs.

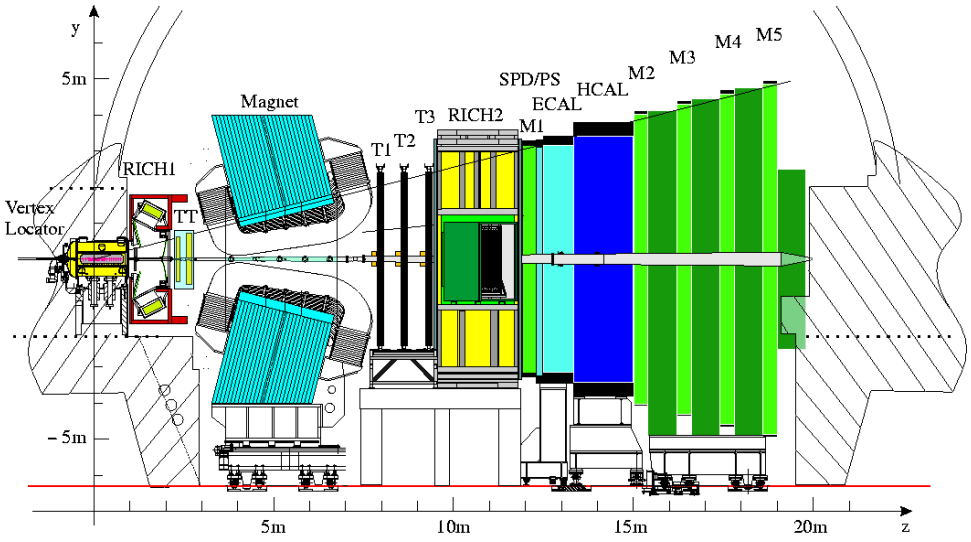

Figure 2.4: A cross-section in the y-z plane of the LHCb detector in its cavern. On the left, the Vertex Locator is situated around the interaction point. TT and T1 to T3 indicate the trigger tracker and main tracker stations respectively. The RICH1 and RICH2 are the two Čerenkov detectors. The calorimeter system consists of the SPD/PS, ECAL and HCAL. The muon detector stations are labelled M1 to M5.

- To identify different B meson decays with identical topology, a good particle identification (PID) is necessary. In LHCb, the following detectors contribute to the PID:
  - Two Čerenkov (RICH) detectors are deployed to achieve $K^{\pm}$-$\pi^{\pm}$ separation for momenta up to 100 GeV/c.
  - Hadrons are separated from electrons using the HCAL and ECAL calorimeters. In addition, two layers of preshower detectors are installed to enable electron-photon (e-γ) separation and reject background pions.
  - Muon identification is obtained using the stand-alone muon system which comprises five stations with projective geometry w.r.t. the interaction point. The Level-0 trigger uses the muon system to efficiently identify muons with a transverse momentum above 1.3 GeV.
- To minimise multiple scattering effects and not to deteriorate electron and photon detection, as little material as possible should be present in the acceptance region. In LHCb, an effort is made to limit the contribution of the material introduced by the tracking detectors and foremost RICH detector to half a radiation length [13].

In the following sections, the sub-detectors will be discussed individually.

2.4 Vertex Locator

To reconstruct the primary vertex and measure the impact parameter (IP) of tracks from a B meson decay, the vertex locator (VELO) is optimised for the measurement of track coordinates close to the interaction region.

The VELO embodies 21 stations, each consisting of 2 layers of silicon detectors. The detectors are of half-circle shape, and are arranged perpendicular to the beamline. To reconstruct particle tracks with high spatial resolution, the VELO stations approach the beam as close as 7 mm. The detectors are separated from the primary LHC vacuum by a corrugated aluminium foil allowing a small overlap between station halves for proper alignment. In the secondary vacuum, the stations reside on a common support structure, which can be retracted as a whole to avoid damage during LHC injection.

The width and the small crossing angle of the LHC bunches results in a spread σ=5.3 cm along z of the pp interaction point. The VELO stations are positioned such that even with the large spread in the z direction of the primary interaction, 99.9% of the tracks traverse at least 3 stations within the acceptance from 15 to 390 mrad [13]. Fig. 2.5 contains a schematic cross-section view of the station arrangement of the VELO.

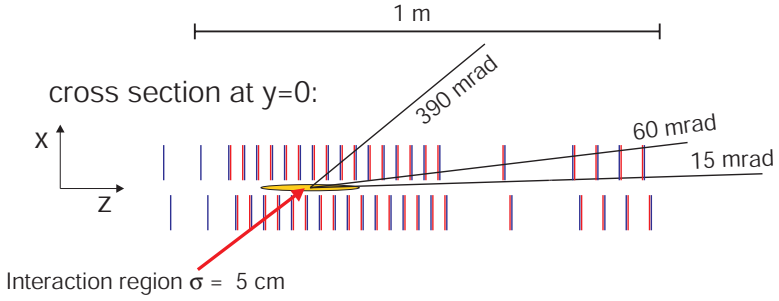

Figure 2.5: A schematic picture of the VELO detector, showing a top view of the station layout; vertical lines indicate the station positions.

The two detector layers in a station are separated by 2 mm in z. One detector layer has a 'r' layout: strips have a constant radius at a pitch varying from 40 μm at the inside to 103 μm at the outside. The other has a 'ϕ' layout: the strips are arranged radially with a stereo angle (10° and 20°), the pitch is 35.5 μm at the inside and 96.6 μm at the outside. Sensors with a r and ϕ layout are depicted in Fig. 2.6. The r-ϕ layout offers the following advantages:

- Due to the large Lorentz boost, the projection of the impact parameter (IP) of B meson decay products with respect to the primary vertex is large in the r-z plane.

Therefore, tracking in 2 dimensions suffices to accurately estimate the track IP. This is used in the trigger, see paragraph 2.9.2.

- The smallest strip pitch, hence the best resolution, is closest to the beam axis where it contributes most to the accuracy of the track position and slope measurement.

The first two stations at the upstream side of the VELO are dedicated to be used as a Pile-Up trigger detector and consist of r-type sensors only.

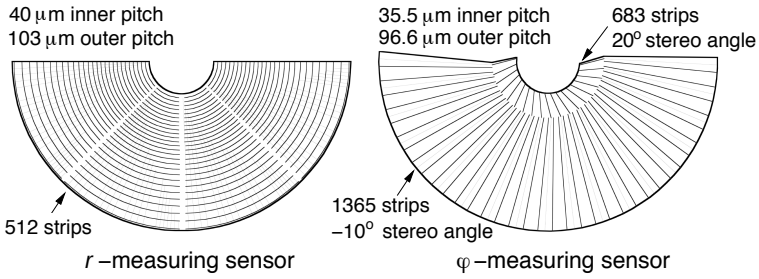

Figure 2.6: Layout of the VELO silicon sensors. Detectors halves with r and ϕ layout are depicted on the left and right respectively.

2.5 Tracking Detectors and the Magnet

The tracking detectors are used to reconstruct the B meson mass by measuring the momentum of its decay particles. With a precise mass reconstruction, background events are efficiently rejected. To reconstruct decays with high track multiplicities, the track finding efficiency must be high.

The main task of the tracking system in LHCb is to find charged particle tracks in the region between the VELO and the calorimeters and measure the particle momenta. Measurements of the tracking stations are used to link track segments from the VELO detector to calorimeter clusters and tracks in the muon detectors. Furthermore, information on the direction of track segments pointing into the RICH detectors is used for particle identification.

The track bending power required for a momentum resolution of 0.3-0.6% for particles with momenta up to 150 GeV/c is about 4 Tm assuming a few hundred μm spatial resolution for the tracking detector [27].

In addition, good uniformity of the integrated magnetic field versus the track slope is required for the muon momentum estimation in the muon trigger algorithm. In LHCb, a warm-coil dipole magnet is deployed to fulfill this task. The field is oriented perpendicular to the x-z plane, referred to as the bending plane. The field strength at the z-axis is plotted in Fig. 2.7.

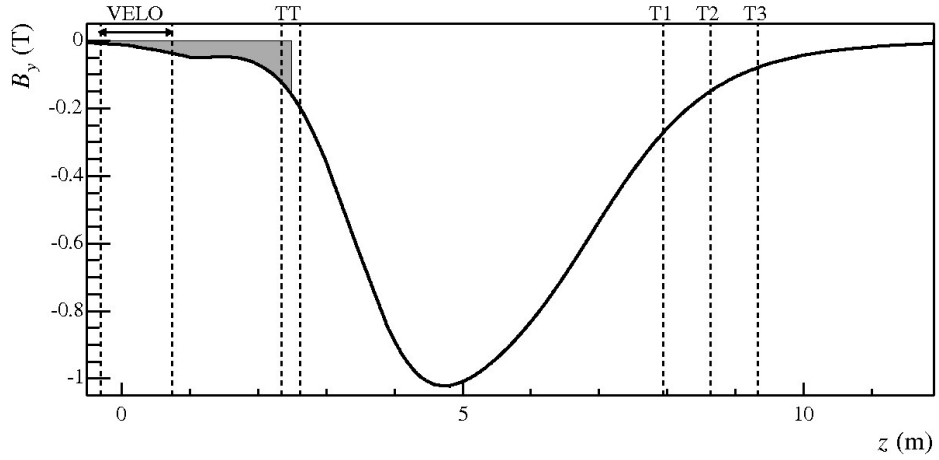

Figure 2.7: Magnetic field strength at the z-axis. The position of the VELO, TT and T stations is indicated with vertical lines. The shaded area covers an integrated field of $\int B\,\mathrm{d}z = 0.15$ Tm between the VELO and the TT.

The particle momentum is measured by fitting a track trajectory to the tracker measurements. A more simple but less accurate way of track momentum estimation is the p_T-kick method: the track deflection ('kink') in the magnetic field is estimated by measuring the track slopes in the low-field regions up- and downstream of the magnet. On the upstream side this task is performed by the VELO detector and a tracker station which is also used for triggering purposes, the Trigger Tracker (TT). Downstream of the magnet, three stations are positioned in the low-field region. These stations are labelled T1-T3 and make up the main tracking volume.

Particle fluxes in LHCb are very high near the beampipe but fall off rapidly as distance to the beam axis increases. To limit detector occupancy, the main tracking stations are subdivided in an Inner Tracker (IT) detector with small channel pitch and a coarser grained Outer Tracker (OT) detector. The tracking detectors are composed of four detection layers. The wires or strips of individual layers have angles of 0°, -5°, +5° and 0° with the vertical y axis and are referred to as x, u, v and x layers respectively. Each station embodies 4 layers, this provides the highest resolution in the bending plane while the stereo angles allow for a 3D reconstruction of the tracks. In the following paragraphs, the TT, IT and OT detectors are presented individually.

Trigger Tracker

Using the TT station, track momentum information can be obtained at trigger level. Between the VELO detector and the TT station an integrated magnetic field of 0.15 Tm is present, indicated by the shaded area in Fig. 2.7. By reconstruction of the small

deflection of high-momentum tracks, the track transverse momentum can be estimated with a resolution of $\delta p_T/p_T = 25\%$ at $p_T = 1\,\text{GeV}$ [28]. To facilitate measurement of the track slope, the pairs of xu and vx layers are separated by a 30 cm gap.

The second task for the TT station is to aid in the reconstruction of particle decays outside the VELO detector and measure the trajectories of low-momentum particles which are bended out of the acceptance by the magnetic field.

A TT detector layer is composed of silicon microstrip sensors which measure 96 $\times$ 94 mm^2 and contain 512 strips at a 183 μm pitch. To keep the number of readout channels, hence the cost, at a reasonable level, multiple strips are connected in series vertically and read out by a single preamplifier channel if allowed by the occupancy. From beam test measurements [29], it is found that noise considerations limit the number of strips per input channel to 4. Furthermore, a sensor thickness of 500 μm is mandatory to have a sufficiently high signal to noise ratio for operation with fast shaping times as required in LHCb.

To minimise dead material in the acceptance region of LHCb, low-mass Kapton cables are used for the transport of the inner sensor signals to the readout electronics, positioned at the horizontal edges of the station. The station dimensions, sensor arrangement, and readout connection scheme for a single TT layer is depicted in Fig. 2.8.

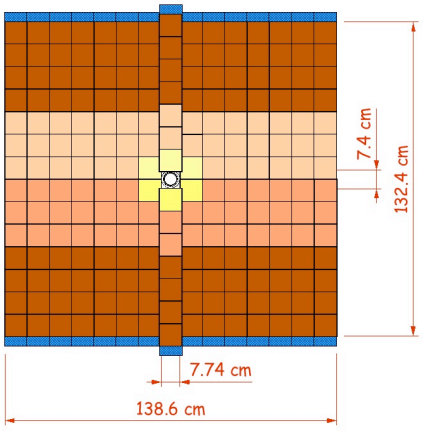

Figure 2.8: Layout of the upstream x layer of the TT station. The sensor arrangement is shown; the strips on sensors with equal grey-shades are connected in series in vertical direction to a single readout channel. The signals of the inner sensors are transported through Kapton cables (not shown).

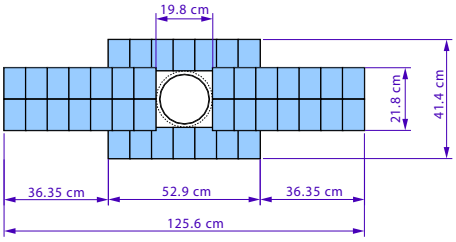

Figure 2.9: *X*-layer of an Inner tracker station. The 4 boxes arranged around the beampipe and the individual sensors inside the boxes are shown.

Inner Tracker

In the T1-T3 stations, the IT covers the regions around the beampipe where the particle flux is highest. A cross-shaped geometry optimises the coverage while conserving surface. Each station consists of four independent detector boxes arranged as depicted in Fig. 2.9.

The IT consists of silicon strip sensors with 78 mm width and 110 mm length. The strip pitch is 198 μm. The sensors are mounted on ladder structures. To ensure full coverage, ladders are staggered in z, allowing a small overlap between neighbouring sensors. 7 ladders form a station layer, 4 layers are mounted in a single box in $xuvx$ arrangement. The side boxes have 2 ladders with strips of the lower sensor connected in series with strips of the upper sensor to a single readout channel, where the top and bottom boxes have single-sensor ladders. To ensure a sufficiently large signal over noise ratio, the sensor thickness is 320 μm for single sensor ladders and 410 μm for two-sensor ladders. A detailed description of the Inner Tracker design and performance can be found in Ref. [30].

Outer Tracker

The OT is a gas-filled straw tube detector, covering about 99% of the summed surface of the T1-T3 tracker stations. The boundaries between the OT and the IT were optimised with respect to detector occupancy and track reconstruction efficiency [31]. Allowing for some overlap between the OT and IT detectors for alignment, and taking some safety margin into account, the OT extends as far as the occupancy limits imposed by the tracking algorithms allows it to, thereby conserving IT surface.

Each of the four layers of the OT stations is composed of modules housing two staggered monolayers of 64 straw tubes each, as is depicted in Fig. 2.10. Straw tubes are separated at the $y = 0$ plane to limit channel occupancy. To avoid an insensitive zone in the OT, the point where the straw tubes are separated is staggered throughout the detector.

The greater part of the modules stretches along the full height of the station and has equal dimensions. Covering the area around the IT requires modules of different sizes as

can be seen from Fig. 2.11. Each module is mechanically stable, gas tight and capable of stand-alone operation.

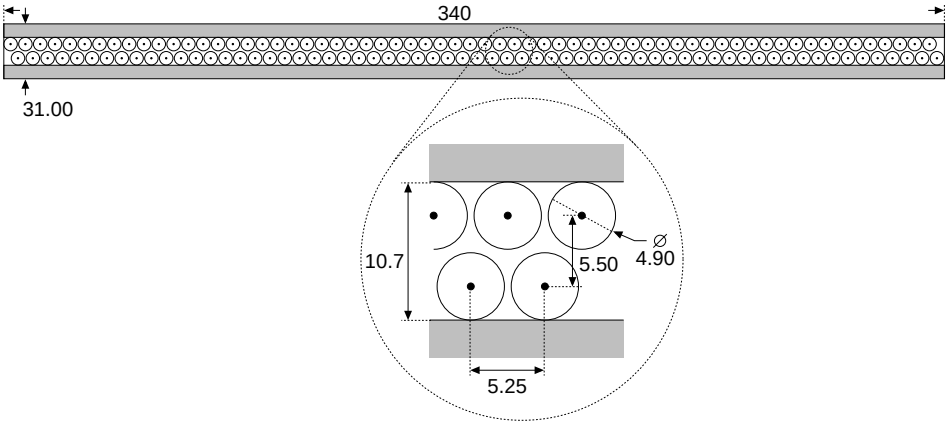

Figure 2.10: Cross-section of an Outer Tracker module. The inset shows the arrangement of 2 monolayers of straw tubes inside a module. All dimensions are in mm.

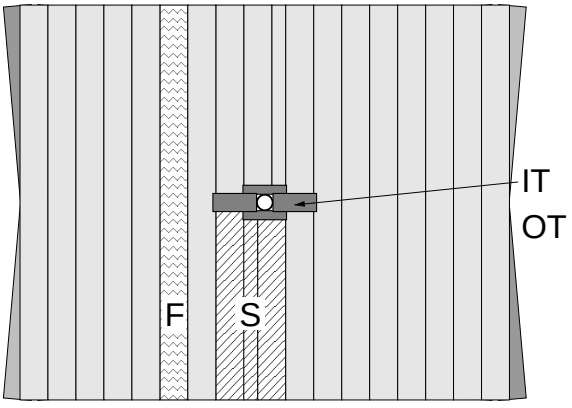

Figure 2.11: Arrangement of Outer Tracker modules in a station. The F and S module types are outlined. IT indicates the Inner Tracker station with its module layout.

Straw tubes have an inner diameter of 4.9 mm and are wound of two layers of polyimide foil (Kapton). Kapton is known for its radiation hardness. The inner foil layer

is conductive carbon-doped Kapton XC, which acts as a cathode. The outer Kapton layer is laminated with an aluminium layer to provide shielding between neighbouring channels. At the tube ends, and every 80 cm in between, locator pieces support and centre the anode wire with a precision better then 100 μm.

Straw tubes are read out at the upper and lower edges of the stations. Unlike the other subdetectors, the OT measures drift times rather than pulse heights. The readout time window exceeds a single LHC bunch crossing interval due to the limited drift speed of the counting gas. Using a mixture of argon and carbon dioxide as counting gas, the OT resolution is better then 200 μm.

In this thesis, a discussion on the requirements, design and production of the OT is included in Chapter 3. Subsequently, Chapter 4 focuses on the electrical properties of the straw tubes and readout electronics of the OT detector.

2.6 RICH Detectors

Particle identification is necessary to differentiate between different CP-violating decays with identical topologies. To properly identify (semi-)leptonic B meson decays, the calorimeter and muon systems are used for e-μ identification. To study $B \to DK$ and $B \to D\pi$ decays, an adequate K-π separation is crucial.

Čerenkov detectors are used to distinguish between charged hadrons with different mass. Charged particles emit electromagnetic (Čerenkov) radiation when they traverse a material with a velocity v exceeding the local phase velocity of light in that material. This radiation is emitted on a cone with an angle θ_C which relates to the particle velocity $\beta = v/c$ as:

$$\cos\,\theta_C = \frac{1}{\beta n}\,, \tag{2.3}$$

where n is the refractive index of the material traversed. Knowing the particle velocity and momentum, the mass can be extracted.

Čerenkov radiation is emitted at nonzero angles θ if the particle velocity exceeds the threshold of $\beta = 1/n$. For very high velocities, $\beta \sim 1$ and the Čerenkov angle saturates at $\cos\,\theta_C = 1/n$.

In Ring Imaging Čerenkov (RICH) detectors, materials with different refractive indexes (radiators) are used to generate the Čerenkov photons. The photons emitted along the particle trajectory are projected as a ring on a planar array of photodetectors through reflective optics. The radius of the ring is proportional to θ_C. In LHCb, two of these detectors are installed. Table 2.2 contains the refractive indexes of the used radiators with the corresponding saturation angles and threshold energies for pions and kaons.

Both RICH detectors use pixellated hybrid photodiodes (HPD) for photon detection. The use of HPDs is dissuaded when the magnetic field strength exceeds 1 mT [32]. For both RICH detectors, shielding structures are designed to reduce the magnetic field strength to acceptable levels.

Radiator		Aerogel	C_4F_{10}	CF_4
n		1.03	1.0014	1.0005
θ_{max}	[mrad]	242	53	23
$p_{th}(\pi)$	[GeV]	0.6	2.6	4.4
$p_{th}(K)$	[GeV]	2.0	9.3	15.6

Table 2.2: Refractive index n, saturation angle θ_{max} and threshold momentum p_{th} for pions (π) and kaons (K) for the three radiators in the RICH detectors.

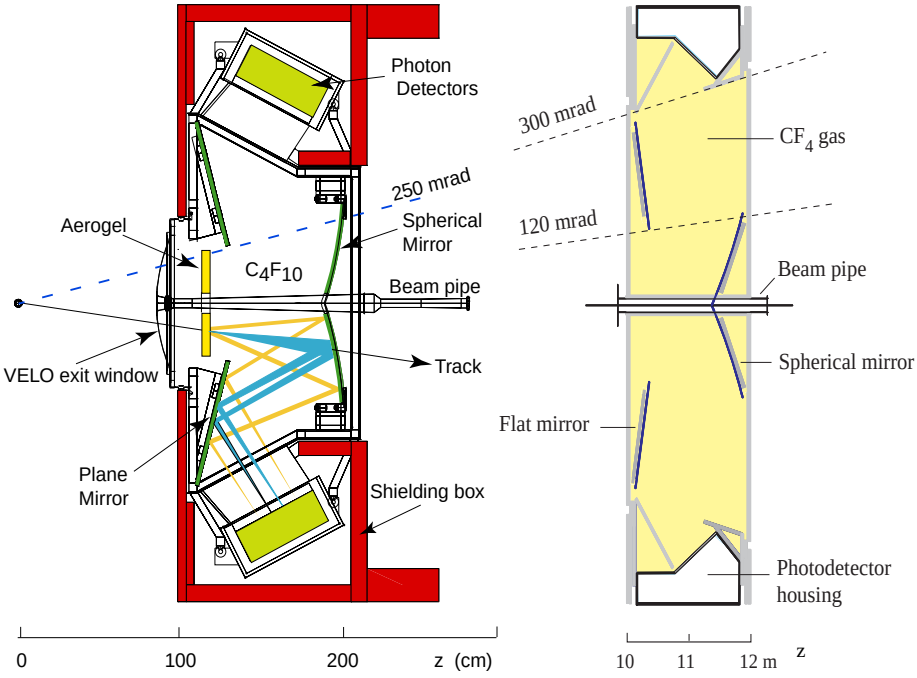

Figure 2.12: Cross-section view of the two RICH detectors. On the left, RICH 1 is depicted in a side-view, where the RICH 2 detector on the right is seen from the top. The left picture features rays of radiated light being projected on the photodetectors.

The RICH1 is located upstream of the magnet. It identifies lower momentum particles up to about 60 GeV/c, using both aerogel and C_4F_{10} gas as radiators. Its acceptance starts at 25 mrad and extends to the full LHCb acceptance of 250 mrad and 300 mrad in vertical and horizontal direction, respectively.

Further downstream, in front of the calorimeter, RICH2 is installed. This detector has a smaller angular acceptance, from 15 mrad to 120(100) mrad horizontally (verti-

cally). In the RICH2, CF_4 gas is used as a radiator for particle identification up to 100 GeV/c. The RICH system is capable to separate kaons from pions with 90% efficieny while misidentifying a pion as a kaon in 10% of the cases for momenta up to 100 GeV/c [13].

2.7 Calorimeters

Due to their high mass, a B-hadron decay produces leptons, hadrons or photons with a large transverse energy E_T. The calorimeter is used for the measurement of the energy and position of the decay products. This information is vital to the L0 trigger as described in paragraph 2.9.1, therefore it has to be provided with sufficient selectivity within a few μs. Another essential function of the calorimeter system is the detection of photons to enable the reconstruction of B meson decay channels containing a prompt photon or neutral pion($\pi^0 \rightarrow \gamma\gamma$). This requirement defines the detector performance demands in terms of energy resolution and granularity.

A calorimeter system measures the energy of particles by their absorption. An incident particle is stopped as it interacts with the calorimeter material, thereby losing energy by creating a cascade of secondary particles, the so-called 'particle shower'. When the energy of the incident particle has sufficiently decreased it is finally absorbed.

In case the calorimeter bulk material has scintillating properties or if it is interleaved with scintillator material, the amount of scintillation light generated by the particle shower is a measure for its initial energy.

The LHCb calorimeter system [33] consists of the following detectors arranged in downstream direction:

- A scintillating pad detector (SPD) for identification of charged particles and electron-photon separation.

- A preshower (PS) detector, behind a 12mm lead wall, for the detection of early shower developments from electromagnetic particles. This is particularly useful to reject the pion ($\pi^{\mp}$) background in electron identification.

- An electromagnetic calorimeter (ECAL) to identify electrons and photons, and measure their energy. The ECAL resolution is $\sigma(E)/E = 10\%/\sqrt{E} \oplus 1.5\%$, with E in GeV and where $\oplus$ means addition in quadrature.

- A hadronic calorimeter (HCAL) to measure the energy of charged hadrons, in particular pions and kaons. The resolution obtained by the HCAL is $\sigma(E)/E = 80\%/\sqrt{E} \oplus 10\%$.

All detectors in the calorimeter system share the same measurement technology. Layers of material with high particle stopping power are interleaved with scintillating plastic tiles. To avoid self-absorption of the scintillation light, wavelength-shifting fibres are incorporated in the tiles for the light collection. Photomultiplier tubes (PMTs) are

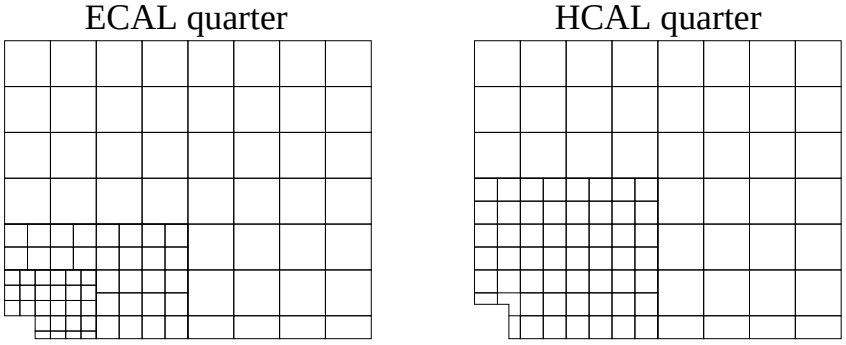

Figure 2.13: Cell arrangement in quarters of the electromagnetic (left) and hadronic calorimeter (right). Together with the ECAL and HCAL, the SPD and PS have a projective geometry w.r.t the interaction point, with a similar arrangement of detector cells.

used for the light detection. The SPD and PS are equipped with multi-anode PMTs, whereas in the ECAL and HCAL, single-channel PMTs are used for the photodetection.

The HCAL and ECAL both have a modular design; the modules ('cells') of a quarter of the HCAL and ECAL are arranged as depicted in Fig. 2.13. The granularity of the ECAL is chosen such that showers from individual photons originating from a π^0 with energy $<$50 GeV can still be separated [33]. The ECAL, SPD and PS detectors have a projective cell geometry pointing to the interaction region.

2.8 Muon Detector

Muons with a high transverse momentum (p_T) are present in the final states of several CP-violating B decays, and muons from semi-leptonic B decays provide a tag of the initial state flavour of the accompanying B hadron. Using their penetrative power, the muon detector provides a robust trigger input.

The muon system embodies 5 stations, labelled M1 to M5. M1 is placed in front of the SPD, M2 to M5 are positioned downstream of the calorimeters. Between the M2 to M5 stations, iron walls act as a muon filter.

Each station is built from multi-wire proportional chambers (MWPCs). The MWPCs give a full response within 25 ns, allowing hits to be unambiguously assigned to their corresponding bunch crossing. The channel size is determined by the rate handling capabilities. Since the particle flux strongly decreases with increasing distance to the beampipe, the muon stations are divided into regions of varying granularity, as shown in Fig. 2.14. For the innermost region of M1, particle rates reach 400 kHz cm^{-2}s^{-1}, exceeding the capabilities of MWPC detectors. Therefore, gas-filled pad detectors using gas electron multiplier (GEM) foils are used in this part of the detector [34].

The arrangement and dimensions of the MWPC and GEM chambers are chosen such

that a projective geometry w.r.t. the interaction point is kept throughout the stations. The muon system is described in detail in [35].

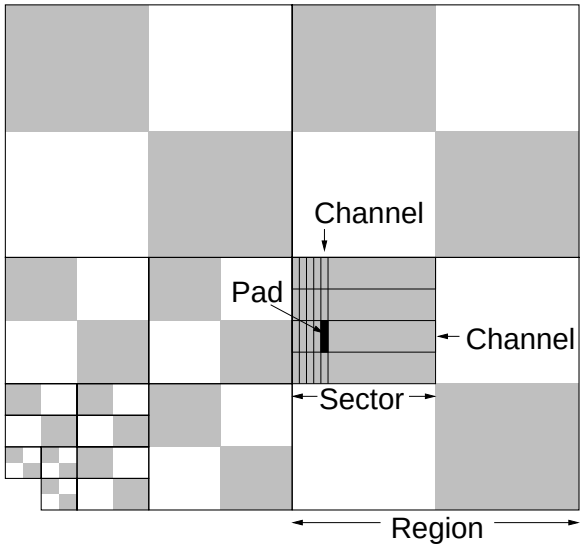

Figure 2.14: Layout of a muon station. The channels which form the logical pads are indicated. The trigger algorithm acts on pads grouped in sectors, which are arranged in regions. The pad size increases with the distance to the beam pipe.

The readout of the muon detectors provides a binary hit signal and timing information. To simplify the muon reconstruction for triggering, detector hits are characterised by the channel number only. Anode wire hits and cathode strip hits are combined to form logical pads on which the track finding algorithm acts. The timing information is accessed by offline reconstruction algorithms.

A muon is assumed to originate from the interaction point, allowing the estimation of its momentum using the p_T-kick method, described in Section 5.1. The error on the p_T measurement, introduced by the limited detector resolution is small; it is designed not to dominate the error caused by multiple scattering of muons passing through the calorimeter. As a consequence the stations surrounding the calorimeter, M1 and M2, contribute most to the accuracy of 25% on the p_T measurement. Since the station are 99% efficient, a 95% trigger efficiency can be reached for muons originating from B decays [36].

2.9 Trigger System

At the LHCb interaction point, about 12 MHz of the 40 MHz LHC bunch crossing rate contains one or more pp interactions. In these interactions, $b\bar{b}$ pairs are produced at a 100 kHz rate. In 15.1% of these events at least one B meson will have all its decay products contained in the LHCb acceptance [11]. To reject the background and efficiently select B decay events with branching fraction of 10^{-4} or less over a large variety of final states, a flexible trigger system is needed.

In LHCb, three subsequent trigger levels labelled Level-0 (L0), Level-1 (L1) and the High Level Trigger (HLT) are deployed. These trigger levels reduce the 40 MHz bunch-crossing rate to 2 kHz. In the following paragraphs, the trigger levels are discussed individually.

2.9.1 Level-0 Trigger

The purpose of the L0 trigger is to reduce the initial 40 MHz LHC clock rate to an average output rate of 1 MHz. At this rate, all detector responses are digitised and stored in buffer memory awaiting the L1 trigger decision.

The L0 trigger uses the fact that B-hadrons have a relatively high mass. Their decay produces large E_T leptons, hadrons and photons that can trigger L0. On the other hand, events with multiple pp interactions or extraordinary high track multiplicity rather than containing a genuine B decay can trigger L0. This should be avoided since these events take a proportionally large amount of the trigger- and data transport bandwidth and processing power. A pile-up detector system is installed to veto multiple pp interactions by counting the number of tracks from secondary vertices. Event track multiplicity is determined by using the SPD and pile-up multiplicity [28].

The L0 decision unit therefore generates the L0 trigger decision based on the following inputs:

- **The Calorimeter** provides the highest E_T cluster for hadrons, electrons and photons, and the hit multiplicity of the SPD.
- **The Muon system** provides the two highest p_T muon candidates.
- **The Pile-Up detector** provides the number of tracks in a 2^{nd} vertex and hit multiplicity.

An event triggers L0 if any threshold listed in Table 2.3 is exceeded and the event passes the global cuts summarised in Table 2.4. If the sum of the transverse momenta of the two highest p_T muons ($\Sigma p_{\mathrm{T}}^{\mu}$) exceeds the threshold of 1.3 GeV, the event is accepted irrespective of the global cuts.

In Table 2.5, the L0 trigger efficiencies for the benchmark B decay channels are listed. The L0 efficiency is higher for channels containing a particle which triggers at a lower energy threshold as listed in Table 2.3. Due to the π background, the L0 efficiency for electrons is lower as expected from the energy threshold.

E_T thresholds	Value (GeV)
hadron	3.6
electron	2.8
photon	2.6
π^0 local	4.5
π^0 global	4.0
muon	1.1
$\Sigma p_{\mathrm{T}}^{\mu}$	1.3

Table 2.3:

Level-0 trigger thresholds for various particles.

Global Cuts	Value
Tracks in 2$^{\mathrm{nd}}$ vertex	≥ 3
Pile-Up Multiplicity	< 112 hits
SPD Multiplicity	< 280 hits
Total E_T in HCAL	$\geq 5.0\,\mathrm{GeV}$

Table 2.4:

List of Level-0 cuts on global event variables.

Channel	L0 efficiency (%)
$B^0 \to \mu^+\mu^- K^*$	93.6±0.7
$B^0 \to J/\psi\,(\mu^+\mu^-)K^0_S$	89.3±0.5
$B^0_s \to D^{\mp}_s K^{\pm}$	47.2±0.3

Table 2.5: Level-0 trigger efficiencies for three benchmark channels listed in Chapter 1.

2.9.2 Level-1 Trigger

The L1 trigger reduces the L0 output rate of 1 MHz to 40 kHz. At this rate, the data acquisition (DAQ) system reads out all detector data and ships it off-detector, using existing technology at reasonable cost.

The L1 trigger algorithm uses two main features of the B meson: its large mass and its long lifetime, to improve the purity of the selected events.

During their lifetime, B mesons move along the beamline. With respect to the primary vertex where B mesons are produced, the B decay tracks have a large impact parameter (IP), see Section 1. Since the decay tracks point back to the beamline, a 2 dimensional (2D) track reconstruction in r-z suffices to accurately measure the track IP. Most of the 2D tracks originate from the primary vertex, which is reconstructed with $60\,\mu$m resolution in z, and $25\,\mu$m in the transverse direction. The IP resolution from high-p_T tracks not pointing to the primary vertex is about $30\,\mu$m [37]. In Fig. 2.15, an event is shown containing the hits and reconstructed 2D tracks for a 45° slice of the VELO r-sensors.

To reject ghost tracks and select tracks which are likely to originate from a B decay, tracks found in 2D are reconstructed in 3D. To limit the algorithm execution time, the only tracks which are reconstructed in 3D are:

- tracks that match a muon track provided by the L0 trigger.
- tracks that have an IP between 0.15 and 3.0 mm.

This selection forms the collection of L1-VELO tracks.

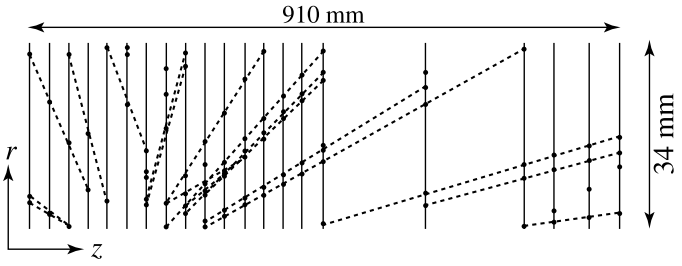

Figure 2.15: Event display of the 2D tracking in the VELO detector. Hits and reconstructed tracks in a 45° section of the detector r-sensors are shown.

To eliminate low-momentum tracks faking a high IP, track momentum information is obtained by extrapolation of the 3D tracks through the fringe field of the magnet to the TT station. The deviation from a straight line trajectory allows for a momentum estimate with 25% resolution at p_T =1 GeV.

From the successfully reconstructed tracks with high IP, the two highest p_T tracks are evaluated for the trigger decision. From these tracks, two variables are calculated: Σp_T and $\Sigma \mathrm{IP}/\sigma_{\mathrm{IP}}$, where σ_{IP} is the uncertainty on the IP, based on the track p_T. An L1 trigger decision is taken by cutting simultaneously on these variables [28].

The L1 algorithm uses data from the L0 trigger, the VELO and TT detectors and is implemented in software running on a processor farm. This allows the L1 trigger to be flexible and scalable: when permitted by data bandwidth and processing power, data from the tracker or muon detectors could be used for an L1 trigger decision.

2.9.3 High Level Trigger

The HLT reduces the 40 kHz L1 output rate to 2 kHz. The HLT has access to all detector data: subdetector data is combined for global event reconstruction.

As a first step, the HLT repeats the L1 trigger algorithm. Where the L1 trigger uses a reduced data format to conserve processing resources, the HLT has access to full detector precision data. In the track reconstruction, information from the T1-T3 stations is added to obtain a momentum resolution better then 1%. This results in a event rejection of 50% in 4 ms on average with no significant loss in signal events.

For the following steps, algorithms are under development. Preliminary studies indicate that by the exclusive selection of interesting B decays, the HLT can reduce the output rate well below a few hundred Hz. In addition the possibility of including the RICH information is studied, which would improve the selection of many specific B decay channels.

The HLT is implemented in software algorithms running on the processor farm which is shared with the L1 trigger. The latency is tuned to 10 ms on average. By rejecting non-interesting events as soon as possible, more CPU time is saved for the remaining

events.

Of the 2 kHz output rate, 1.5 kHz is reserved for inclusive single- and dimuon triggers. Chapter 6 contains details and a possible implementation of these inclusive triggers.

2.10 Readout and Data Acquisition System

LHC experiments have to cope with very high interaction rates. Fast and accurate front-end (FE) electronics are required. Furthermore, a high-performance online system is needed: the DAQ has to read events of 100 kB size at 40 kHz L1 output rate from the front-end electronics, requiring 4 GB/s bandwidth. A timing and fast control (TFC) system is deployed for distribution of clock and trigger signals. Below, the FE electronics, TFC and DAQ systems are described.

2.10.1 Front-End Electronics

The overall layout of the FE electronics is pictured in Fig. 2.16. The analog front-end is connected to the detector and read out by the L0 electronics. The L1 electronics read and store the L0 accepted data, and deliver information to the L1 trigger processors. Upon an L1 trigger, the DAQ reads and transfers the data off-detector to be processed by the HLT. The key parameters of L0 and L1 electronics are summarised in Table 2.6.

Level-0 Electronics

The LHCb detector is sampled at 40 MHz to provide input for the L0 trigger. The L0 trigger is operated synchronously; the trigger latency is 4.0 μs, independent of the input. During the latency, the detector samples are stored in clock synchronous pipeline buffers. For some subdetectors, analog detector samples are stored, where other subdetectors store data from analog (ADC) or time (TDC) to digit converters. Upon an L0 trigger, samples are transferred within 25 ns to a derandomiser buffer. The derandomiser buffer covers trigger rate fluctuations. Triggering of consecutive events require a derandomiser fill time of 25 ns. The derandomiser buffer holds up to 16 event samples and is read out within 900 ns, allowing a maximum L0 trigger rate of 1.1 MHz. Because of the short latency and high input rate, the L0 trigger is implemented in custom electronics. To accommodate the pipeline and derandomiser buffers, application specific front-end chips are developed which reside on-detector.

Level-1 Electronics

At L1, the remaining data is digitised and stored during the latency of the L1 trigger. Additionally, subdetectors participating in the L1 trigger extract the data and send it to the L1 trigger algorithm running on the processor farm. The algorithm execution time is not fixed; on average it is 1 ms, depending on the input. During the latency, the detector data is stored in the L1 buffers. An event is read out from L0 in 900 ns and accounts 36 data words maximum of 32 bit each. The buffer size is 2Mwords, allowing a

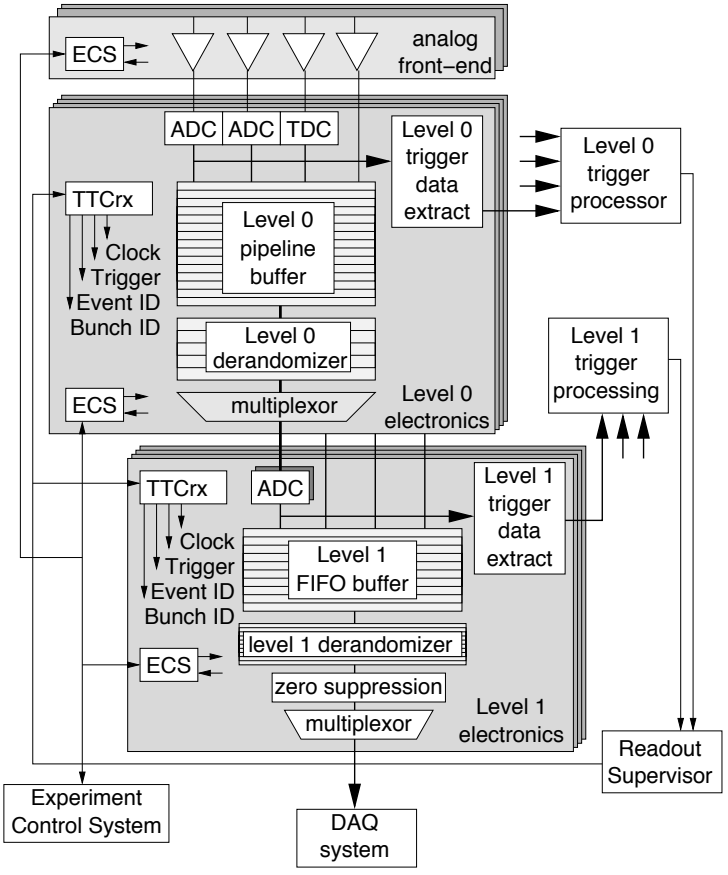

Figure 2.16: Overview of the LHCb front-end electronics system. The analog front-end is indicated on top, followed by the L0 and L1 electronics. The digitisers (ADCs and TDCs), buffers, derandomisers and multiplexers are indicated for both L0 and L1. The data extraction and processing for L0 and L1 is sketched. The electronics are controlled by the Experiment Control System (ECS) and receive Clock, Trigger, Event and Bunch information through the Timing and Fast Controls network receivers (TTCrx).

maximum latency of 52.4 ms. Since the L1 triggers are sent out in chronological order, a time-out mechanism prevents the L1 algorithm exceeding the maximum latency. Upon an L1 accept, event data are transferred to a derandomiser buffer, after which the data is zero-suppressed and wrapped in a standard transfer packet which allows it to be handled by the DAQ system.

Level-0 electronics parameters		
Input rate	40	MHz
Latency	4.0	μs
Pipeline buffer depth	160	cycles
Derandomiser depth	16	events
Derandomiser fill time	25	ns
Derandomiser readout time	900	ns
Maximum output rate	1.1	MHz

Level-1 electronics parameters		
Maximum input rate	1.1	MHz
Event size	36	words
Buffer size	2	Mwords
Max. latency	52.4	ms
Derandomiser depth	2-16	events
Output rate	40	kHz

Table 2.6: Table with L0 and L1 electronics parameters.

Timing and Fast Controls and the Readout Supervisor

The FE electronics are synchronously operated. This is only possible with a proper distribution of the LHC clock, L0 and L1 trigger signals. The Timing and Fast Controls system embodies the Readout Supervisor (RS) which generates and controls the signals for the FE electronics, distributed by the Trigger, Timing and Controls (TTC) network. Additionally, subdetector data is continuously checked whether the front-end electronics are still synchronous to the global system clock.

With a clock-synchronous architecture and the accurately defined specifications on the FE electronics for all sub-detectors, the RS is able to predict the state of the L0 and L1 buffers and derandomisers. Information on the network and processor farm occupancy are read by the RS. Hence it can throttle trigger rates to maximise the data-taking performance without exceeding the capacity of L0 and L1 buffers and derandomisers.

2.10.2 Data-Acquisition System

The DAQ system reads the input data of the L1 trigger algorithm and full data of the L1 accepted events off the front-end electronics and distributes it to the processor farm. It is capable of distributing data also in the case non-standard running modes are required, needed for detector calibration for example. By requiring the FE electronics output to be formatted in standard packets, use can be made of standard high-performance network components [38].

Similarly, the processor farm is foreseen to be built from standard components for both the computing and controller tasks. A processor farm of about 1000 CPUs is expected to fulfill the computing needs. To make optimal use of the available processing

power, the HLT algorithm is foreseen to run continuously, interrupted by the more time-critical L1 algorithms.

2.10.3 1 MHz Readout Scheme

Currently it is assessed whether the full 1 MHz L0 accepted event rate can be transferred off-detector [39]. At the cost of a DAQ capable of handling an eightfold of the data rates, all detector data becomes available to trigger algorithms successive to L0. This could dramatically improve the trigger efficiency and flexibility, enhancing the event yield of channels relevant to CP-violation.

Since there is no hardware imposing limits on the data throughput following the L0 trigger stage, a separate implementation of the L1 trigger is abandoned. Instead, a single trigger algorithm is developed, performing both the tasks previously divided between the L1 and HLT algorithms. In this thesis, a division between L1 and HLT triggers is kept. However, a single trigger algorithm opens up possibilities for a more versatile application of the online track reconstruction algorithm presented in Chapter 5.

Chapter 3

The Outer Tracker

The tracking detectors in LHCb are used to measure the lifetime of B mesons. A B meson is identified from reconstructing its mass through momentum measurement of its decay particles. Subsequently the lifetime is estimated by the measurement of the decay length. The tracking system embodies the VELO, Trigger Tracker (TT) and the main tracker stations T1, T2 and T3. The main tracker stations consist of an Inner Tracker (IT) and an Outer Tracker (OT) detector, as indicated in Fig. 2.4. The requirements, design and production of the latter is described in this chapter.

3.1 Particle Flux in the Tracker

A proton-proton (pp) event containing a B meson produces about 30 primary charged particles [40] in the LHCb acceptance, see Fig. 1.4. These particles produce a multiple of secondary particles through interactions with detector material. On average, about 100 tracks traverse the T stations in events containing a B meson decay in the acceptance. The high particle count in a single event combined with the high event rate at the LHCb interaction point results in a large particle flux, which the T stations have to withstand.

Before the magnetic field, the particle flux density resembles a $1/r^2$ distribution, with r the distance to the beamline. The magnetic field deflects charged particles, as a result the distribution is broadened in the x direction. This effect is illustrated by the simulated particle flux distributions plotted for the TT upstream and T3 downstream of the magnet in Fig. 3.1.

Only a small fraction of the particles traversing the tracker originate from the B meson decay. For a proper identification of B decay particles, all tracks must be reconstructed to assist the RICH detectors in assigning detected photons to B decay tracks, see Section 2.6.

The fraction of detector channels generating a signal in an event is called the detector occupancy. For efficient particle track recognition, the occupancy must be low. A low occupancy can be reached with a high channel granularity. Therefore, the IT, a silicon strip detector with fine pitch, is installed around the beampipe where particle densities are high. The boundary between the IT and OT is optimised for a low OT occupancy while maintaining a small IT surface [31].

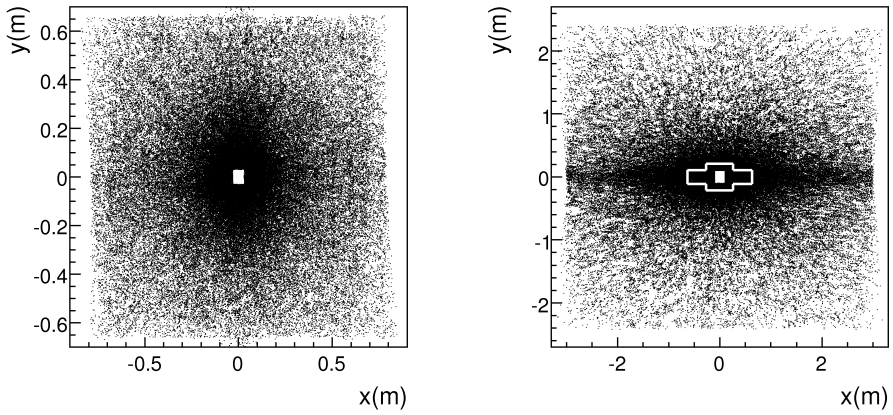

Figure 3.1: Plot of the particle flux density in the TT (left) and T3 (right) stations, located upstream of the magnet at z=2.5 m and downstream of the magnet at z=9.2 m respectively. In the right plot, the boundary between the Inner and Outer tracker is indicated with a white line.

The IT is surrounded by the OT, a gas-filled detector. For a high-rate hadronic environment as present in LHCb, wire chamber technology is the natural choice for fast gas-filled detectors covering a large surface [41]. In the following section, the OT requirements are discussed.

3.2 Outer Tracker Requirements

Besides a high efficiency, the LHCb tracker has to satisfy three main performance requirements, irrespective of the applied detector technology.

1. The resolution should be sufficient to provide a track momentum estimate within 0.5% for particle momenta from 2 up to 100 GeV/c. A high momentum resolution on the B decay tracks reduces the error on the reconstructed mass of the B meson, improving the separation of $B \to \pi\pi$ from $B \to K\pi$ events [42], and increasing the rejection of background events.

2. The channel occupancy must be low for efficient track reconstruction. With an occupancy below 10%, track finding algorithms are sufficiently efficient [43].

3. The tracker must be radiation hard and its performance should not deteriorate during the foreseen lifetime of 10 years.

In the following sections, the consequences of these requirements are discussed individually.

3.2.1 Spatial Resolution Requirement

The precision of the reconstructed mass of a B meson candidate is determined both by the momentum resolution of the reconstructed tracks and by their angular resolution at the vertex. The angles of the tracks at the vertex are measured by the VELO and TT detectors. The momentum is determined by measuring the track deflection in the magnetic field using three T stations, installed over 1.8 m distance in the z direction. Since the field of the dipole magnet is oriented along the y direction, the tracker stations are optimised for resolution in the x direction.

The slope resolution is proportional to the momentum resolution, which strongly affects the B meson mass resolution. The more accurate the track momentum is determined, the more precise the B meson mass can be reconstructed and the more effectively background events can be rejected.

To estimate the detector resolution required to achieve the desired track slope resolution, a simplified model of track slope measurement in the OT is introduced. The model relies on the following assumptions:

1. Tracks originate from the interaction region.

2. Particle trajectories are modelled to have straight segments in the VELO and T stations; the curvature of tracks in these regions with low magnetic field is neglected.

3. The magnetic field is modelled as a singular field of equal strength. Tracks experience an instant change of slope at the focal plane of the magnet, located at $z = 5.2\,\mathrm{m}$.

4. For the determination of the track slopes, measurements from individual layers are used. The layers placed under a stereo angle are assumed to contribute with equal resolution as the vertically oriented layers.

5. An OT station is modelled as if the measurement layers are sandwiched between two layers representing the thickness of the material used in the stations, as sketched in Fig. 3.3.

A sketch of a track in the bending plane is depicted in Fig. 3.2. In the magnetic field B, the Lorentz force F_L acting on a charge q moving with velocity v changes its momentum p with time t according to:

$$\frac{d\overrightarrow{p}}{dt} = \overrightarrow{F_L} = q(\overrightarrow{B} \times \overrightarrow{v}). \tag{3.1}$$

From a particle moving in the z direction, its momentum can be reconstructed from the deflection in the magnetic field. With t_{x_1}, t_{y_1}, t_{x_2}, t_{y_2} the slopes in the x-z and y-z planes in the VELO detector and the tracker stations respectively, the reconstructed

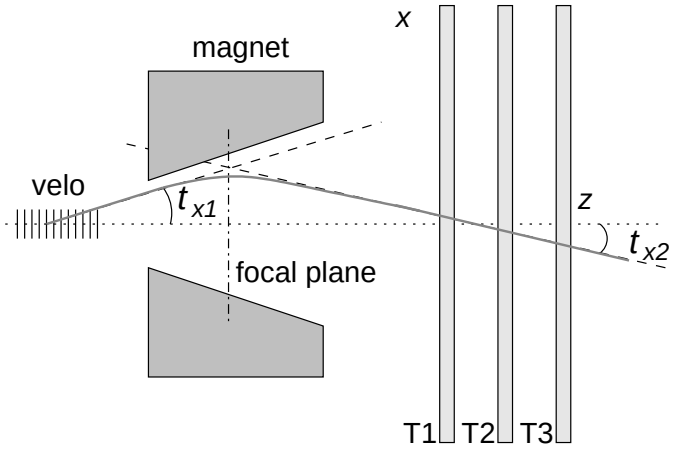

Figure 3.2: A deflected track in the x-z plane. t_{x_1} is the angle with the z-axis in the VELO, t_{x_2} the angle at the tracker stations T1, T2 and T3. The deflection in the magnetic field is modelled as if the track kinks at the focal plane of the magnet.

momentum p_{rec} becomes: [44]:

$$p_{rec} = \int B \, \mathrm{d}z \, \frac{\sqrt{\frac{1+t_{x_2}^2+t_{y_2}^2}{1+t_{x_2}^2}}}{\frac{t_{x_2}}{\sqrt{1+t_{x_2}^2}} - \frac{t_{x_1}}{\sqrt{1+t_{x_1}^2}}}, \tag{3.2}$$

where $\int B \, \mathrm{d}z$ represents the integrated magnetic field in the z direction along the track trajectory.

The inaccuracy of the track momentum is determined by the error on the track slope measurement, which is determined by two effects:

- Multiple scattering caused by the passage of the particle through the detector material changes the direction of flight of the particle. The deviated particle track introduces an error on the momentum estimate. Low-momentum particles are the most affected by multiple scattering.
- For high momentum tracks, multiple scattering is small. The limited spatial resolution of the detector dominates the uncertainty on the measured slope.

To obtain good track momentum resolution, the tracker should have the highest spatial resolution while introducing as little material in the acceptance as possible. These two requirements should be balanced; it is of little use to install a detector with extremely high resolution σ_R when the uncertainty on the track slope from multiple scattering σ_{MS} is large.

The total uncertainty on the slope in the tracker $\sigma_{t_{x2}}$ is given by:

$$\sigma_{t_{x2}} = \sqrt{\sigma_{MS}^2 + \sigma_R^2}. \tag{3.3}$$

The σ_{MS} and σ_R contributions to the slope uncertainty are discussed individually.

Multiple Scattering

When passing through matter, a particle experiences many small-angle scatters. Theory by Molière in Gaussian approximation [5,45,46] gives the following relation for the RMS of the scattering angle, Θ_{MS}, projected on a plane:

$$\Theta_{MS} = \frac{13.6\,\text{MeV}}{\beta cp} z \sqrt{\frac{x}{X_0}}\,\left[1 + 0.038\,\ln(\frac{x}{X_0})\right]\,. \tag{3.4}$$

Here, p, βc and z are the momentum, velocity and charge number of the incident particle. For small angles, it is assumed that the error on the slope due to the multiple scattering $\sigma_{MS} = \Theta_{MS}$. The fraction x/X_0 represents the thickness of the scattering medium expressed in radiation lengths [5]. Knowing the particle momentum, the multiple scattering contribution to the momentum error is calculated. In the top left plot of Fig. 3.4 the contribution to the momentum inaccuracy due to multiple scattering is plotted for three different values of x/X_0.

Detector Resolution

Of the assumptions listed at the beginning of this section, numbers 1 to 3 are taken into account by defining an additional measurement point at the focal plane with a resolution equal to the tracker measurements. The track slope t_{x_2} in the tracker is determined by

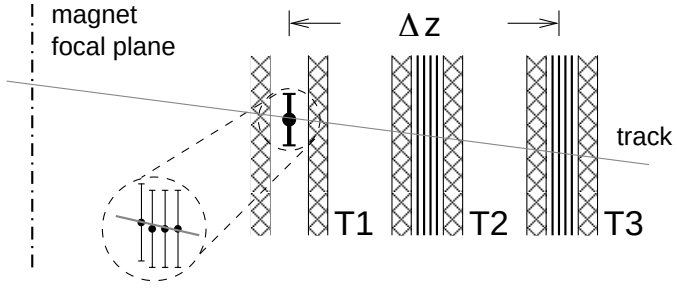

Figure 3.3: Track slope resolution of the tracker stations installed over a distance Δz. A station is modelled by measurement layers surrounded by two layers of material (shaded). Track segments are assumed to pass through the focal plane of the magnet, see text.

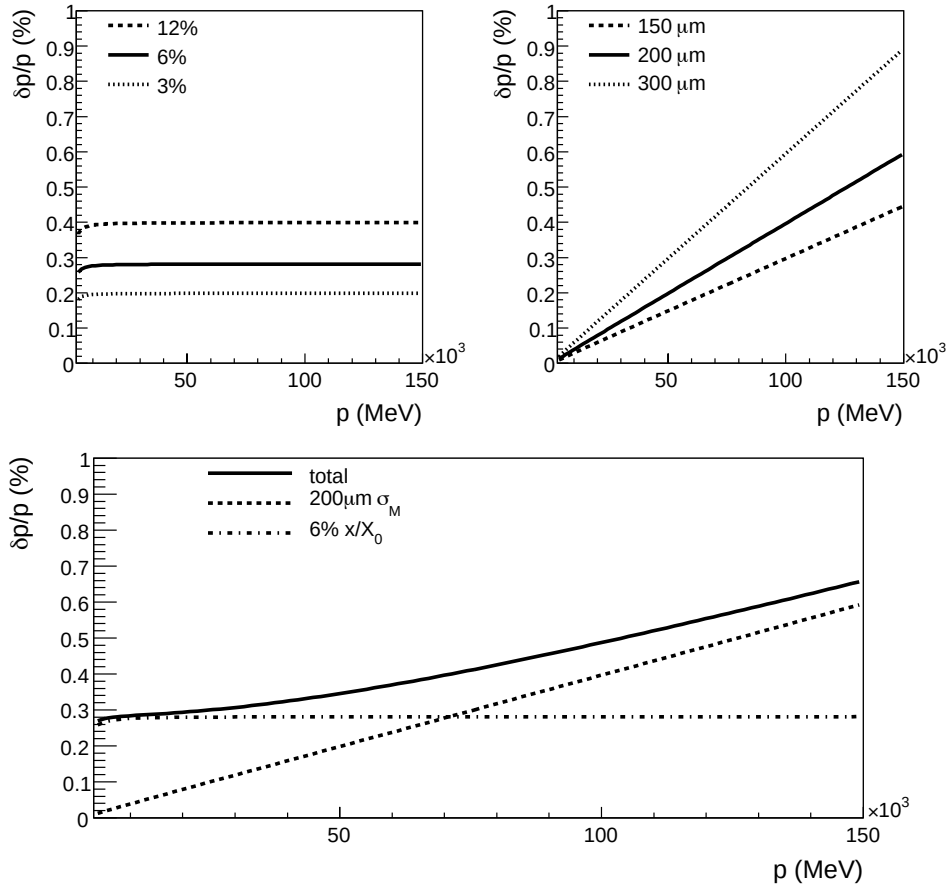

Figure 3.4: In the top plots, the contributions of multiple scattering and resolution to the OT momentum resolution $\delta p/p$ versus p are plotted for different detector thickness (left) and resolution figures (right). The bottom plot contains the total OT momentum resolution (solid line). The contributions from the 6% x/X_0 detector thickness and 200 μm resolution are plotted separately.

fitting a straight line to the measurement points, including the one at the focal plane. When fitting a line to N measurements in x with errors σ_x located at z, the total error σ_R on t_{x_2} becomes:

$$\sigma_R = \frac{\sigma_x}{\sqrt{N(\overline{z^2} - \overline{z}^2)}} \ . \tag{3.5}$$

In the top right plot of Fig. 3.4, the contributions to t_{x_2} from the detector thickness

and the measurement resolution are plotted as a function of the momentum p for various resolutions σ_R.

When a 0.5% precision on the reconstructed momentum is required for track momenta up to $p = 100\,\text{GeV}$, both contributions to the momentum resolution must be balanced. The design of the OT is optimised for a low material budget: an OT station is estimated to introduce 2.98% of X_0 into the acceptance [47]. As a result, 6% of X_0 is present between the measurement layers, see Fig. 3.3. To comply with the momentum resolution requirement, it follows from Eq. (3.5), (3.3) and (3.4) that the OT resolution must be $212\,\mu$m or better.

Using an argon-based drift gas, it is well possible to obtain the required resolution with drift detectors operated at atmospheric pressure.

3.2.2 Occupancy

For efficient track reconstruction, the occupancy must stay below 10%. A low occupancy is obtained with a small surface covered per channel. A small channel surface in wire chamber detectors implies a small wire pitch. However, below a few mm pitch, attractive forces between the anode wires and cathode surfaces limit the applied voltage, and thus the detector efficiency and resolution. Furthermore, detector engineering and production becomes very tedious for long wires with pitches in the order of 1 mm, aside from the cost enlargement that comes with the increased channel count.

For the OT, a wire pitch of 5.25 mm is considered an optimal trade-off between the above-mentioned factors. Accounting for mechanical tolerances, it allows for a drift cell size of 5 mm.

To retain a low occupancy, the channel length is limited by separating the wires at the y=0 plane, where particle fluxes are highest. As a result, typically a channel measures 2.4 m and stretches along half the OT station height.

To reduce the amount of responses from neighbouring events, wire chambers in high-rate environments should be operated with a fast counting gas.

3.2.3 Efficiency

The T stations must be efficient over their full surface to provide tracking algorithms with some redundancy in the number of measurements. The OT is based on wire chamber technology: arrays of wires cover the sensitive area of the detector. To cover for insensitive regions in between the channels, a second, staggered layer of wires is introduced.

3.2.4 Radiation Tolerance

During the foreseen 10 year lifetime of the LHCb experiment, the detectors are exposed to large particle fluxes. The passage of particles can induce damage in materials through a wide variety of processes commonly referred to as radiation damage. For the degradation of detectors, two main effects can be identified:

- the long-term detector stability is affected by degradation of detector materials, caused by the total accumulated dose, and
- the detector performance is worsened due to the exposure of the anode and cathode to ions and radicals of the counting gas constituents. This effect is proportional to the charge deposited in the sensitive volume caused by ionising radiation.

The quantity of radiation causing the damage is hard to predict a priori since it depends on simulations at unprecedented beam energies. In Ref. [48], effort is made to estimate the radiation background in the LHCb experiment. For the tracking stations, the estimated dose accumulated in 10 years of operation is 10 Mrad just outside the beampipe, dropping to 100 krad at the border of the OT and IT. At the outer edges of the OT detectors, about 2 krad is expected.

To ensure the detector to last for the intended LHCb lifetime, accelerated ageing tests have been conducted on single channels as well as entire modules. In sections 3.3.4 and 3.4, the selection and validation of used detector materials, in particular the cathode surfaces, is discussed.

3.3 Straw Tube Detector Technology

Arrays of proportional counters have been used for particle tracking since 1968, when Charpak operated the first multi-wire proportional chamber [49]. The LHCb OT is based on the same technology: particle tracks are reconstructed using the combined response of individual channels operated as proportional counters. To keep the drift time low, a cylindrical drift cell geometry is used in the OT. The anode wires are surrounded by conductive straw tubes with an inner diameter of 4.9 mm acting as cathodes. The cylindrical geometry introduces a predictable limit on the maximum readout time of a OT channel.

3.3.1 Working Principles

A charged particle traversing a gaseous medium will transfer energy to the gas constituents by electromagnetic interactions: if the energy transfer exceeds the ionisation potential of the gas molecule, an electron can be liberated. If this primary electron has enough energy, it can in its turn liberate secondary electrons. The latter process takes place over a short range: the initial particle thus leaves behind clusters of electrons and ions in the counting gas.

In gas at STP[1], the number of primary ionisations per unit length is small. For Ar(70%)-CO_2(30%) gas mixtures as used in LHCb, a minimum-ionising particle (MIP) creates on average 31 clusters of 3 electron-ion pairs each per cm [50].

In presence of an electric field, the ions and electrons will not recombine but drift in opposite directions along the field, thereby scattering off the gas molecules. Due to

[1]Standard Temperature and Pressure: 0° C and 101.325 kPa

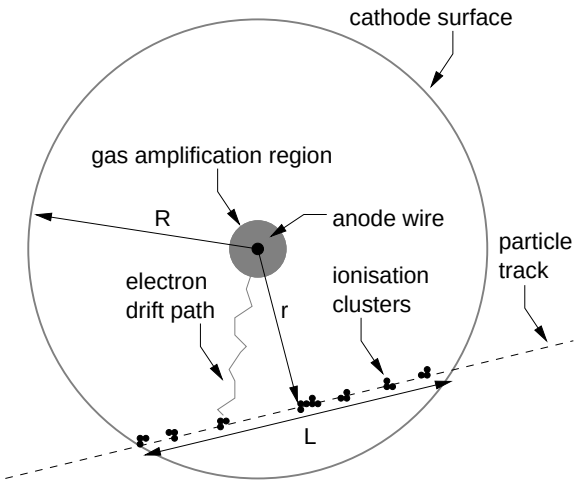

Figure 3.5: Illustration of the working principles of a circular drift cell. R is the cell radius, r indicates the closest approach of the particle to the wire. L represents the length of the particle path inside the drift cell.

their low mass, electrons drift about two orders of magnitude faster than ions. At high field strengths, electrons will be accelerated sufficiently to liberate electrons through collisions with gas constituents. The Townsend coefficient is the average number of electrons resulting from a collision, which depends strongly on the electric field strength. As soon as it rises over 1, additional electron-ion pairs are created in the collisions. With repetitive collisions, this leads to an avalanche of electrons, leaving behind a large cluster of ions near the anode. This process is referred to as gas amplification or gas gain.

For straw tubes with inner diameter R, the electric field E as a function of distance r to the anode wire of diameter r_a is given by:

$$E(r) = \frac{V}{r \ln \frac{R}{r_a}} \tag{3.6}$$

where V is the applied voltage. Close to the wire, the field strength is highest and gas amplification will occur. Combining Eq. (3.6) and data from Ref. [50], it is found that the gas gain starts at 50-100 μm from the anode wire surface for the straw tubes used in the OT, operated at their nominal voltage of 1600 V. An illustration of the working principles of a circular drift cell is included in Fig. 3.5.

Finally, the arrival of the electron avalanche on the anode, and the relatively slow drift of the ions towards the cathode, gives rise to an electronic signal. Depending on the electrical configuration, a detectable voltage or current pulse is generated. The time elapsed between the particle impact and the appearance of the anode signal is dominated by the electron drift. The minimum distance of the track to the anode wire is determined

by timing the drift cell response. To obtain a high spatial resolution, it is crucial that the first cluster arriving at the wire is detected.

3.3.2 Straw Tube Performance

The drift cell in the OT consists of the gas filled cathode straw tube and the anode wire at the centre. Ultimately, the drift cell characteristics determine the OT performance: the resolution of the drift cells should be at least 200 μm and the drift time must be short for a low channel occupancy.

Resolution

Given a gas filled detector, the resolution depends on the counting gas properties and the applied voltage. In order not to let electronic noise dominate the detector resolution performance, the gas gain should be sufficient that avalanches induced by the first cluster arriving at the anode wire are efficiently detected. The anode wire diameter is 25 μm, the straw tube has an inner radius of 2.45 mm and is filled with Ar(70%)-CO_2(30%) drift gas. When using the ASDBLR preamplifier [51], a resolution better than 200 μm is obtained at 1600 V anode voltage [52–54], surpassing the resolution requirement. At this voltage, the gas gain is at least 7×10^4. The measured dependency of the track position resolution on the anode voltage is plotted in Fig. 3.6.

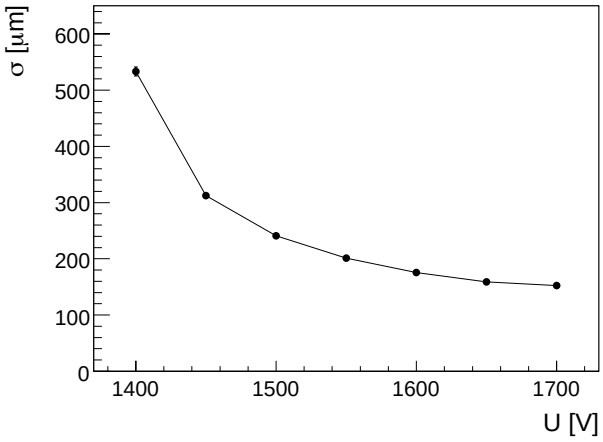

Figure 3.6: Straw tube position resolution σ versus anode voltage U, from Ref. [54]. At 1600 V, the 200 μm resolution requirement is surpassed.

Drift Time

The drift time depends on the field strength present in the drift cell and the counting gas properties. In cylindrical drift cells, the applied voltage and the resulting electric field strength is determined by the gas gain requirements.

Of many available drift gases, a mixture of argon and CO_2 remains stable under particle rates over 100 kHz/ cm, and withstands deposited charges up to several C/ cm [55]. Using this drift gas, the width of the response time spectrum will exceed the 25 ns time between to subsequent LHC bunch crossings. To retain a full drift cell efficiency, the OT detector sample window is extended to a multiple of 25 ns, see Section 4.

The dimensions and drift gas composition are chosen to target a full response within two LHC clock cycles, 50 ns. In Fig. 3.7, the time response spectrum is plotted for a drift cell of 4.9 mm inner diameter, operated with Ar(70%)-CO_2(30%) drift gas in beam tests conducted in 2005 [54]. The spectrum width is 42 ns, this is in good agreement with earlier measurements and simulations [52].

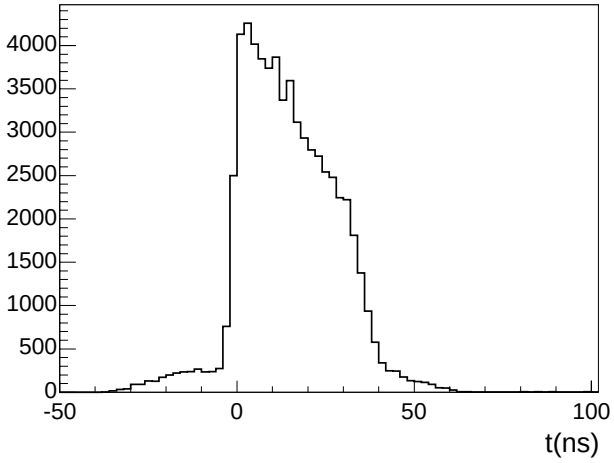

Figure 3.7: Time response spectrum of a straw tube with Ar(70%)-CO_2(30%) as drift gas, taken from Ref. [54].

Since the drift time exceeds 25 ns, an OT event sample contains channel responses from neighbouring events. The presence of channel hits from previous events increases the occupancy and makes track reconstruction more difficult. By using robust pattern recognition algorithms which are tolerant to the presence of spurious hits, track reconstruction is still sufficiently efficient [44].

The admixture of CF_4 lowers the average cross-section for electron scattering on the gas constituents and thus increases the electron drift speed [56], thus decreasing the width of the response time spectrum. Due to its electronegativity, CF_4 absorbs a

fraction of the drift electrons, necessitating a higher voltage to reach the designated gain. Unfortunately, ageing phenomena such as etching of the anode wire are associated with the use of this drift gas, and recent studies correlate anode wire ruptures under irradiation with the presence of CF_4 [57]. Therefore it is decided to run the OT with Ar(70%)-CO_2(30%) as a drift gas.

Efficiency

A monolayer of straw tubes with inner diameter d, arranged at a pitch p has a geometrical coverage of d/p, limiting the monolayer efficiency.

Furthermore, individual straw tubes are not fully efficient over the entire inner diameter. The ionisations caused by the passage of a particle are subjected to Poisson statistics; the probability $P(n;l)$ to have n primary ionisations for a particle traversing a length l in the drift gas is:

$$P(n;l) = \frac{(\frac{l}{\lambda})^n \exp(\frac{-l}{\lambda})}{n!}, \tag{3.7}$$

where λ is the average distance between subsequent ionisations. For an argon based gas mixture at standard conditions, $\lambda \sim 0.33\,\text{mm}$ [50].

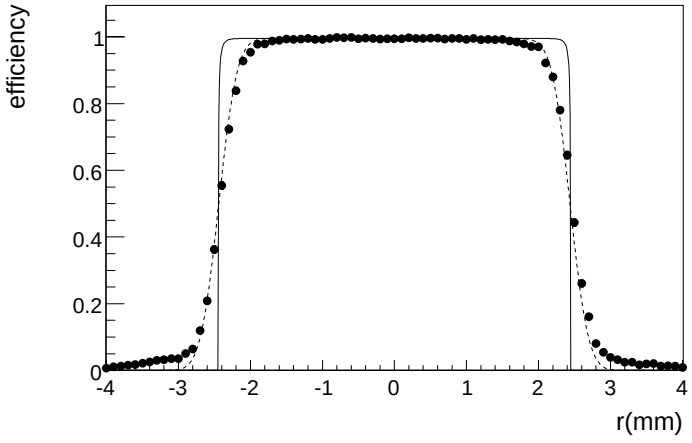

Figure 3.8: Straw tube efficiency versus distance to the anode wire r. The predicted efficiency from Eq. (3.8) with infinite and 200 μm resolution is plotted with solid and dashed lines respectively. Measurements from the 2005 beam test are indicated with dots.

With $P(0;l)$ the probability that no cluster is created over a particle trajectory of length l, the single drift cell efficiency $\epsilon(l)$ becomes

$$\epsilon(l) = 1 - P(0;l) = 1 - \exp(\frac{-l}{\lambda}), \tag{3.8}$$

assuming no loss of primary electrons and a fully efficient detector readout. Channels are only efficient when a charged particle traverses a certain length inside the straw tube; this is expressed by $\epsilon(l)$. The shortest distance between and the anode wire r relates to the straw tube inner diameter R and the traversed path length as $l = 2\sqrt{R^2 - r^2}$. With this formula, Eq. (3.8) is translated in an efficiency curve as a function of r/x. The resulting curve matches the results obtained from beam tests of prototypes [52–54]. The ideal and realistic efficiency curves are plotted in Fig. 3.8 with solid and dashed lines respectively, along with dots indicating measurements from the 2005 beam test.

As can be seen from Fig. 3.9, at 1600 V anode voltage the drift cells are >99% efficient at their plateau, which extends up to a radius of 1.8 mm. To compensate for the inefficiencies at the straw tube edges and the arrangement in monolayers, a single OT detector layer is composed of two staggered monolayers, as depicted in Fig. 2.10.

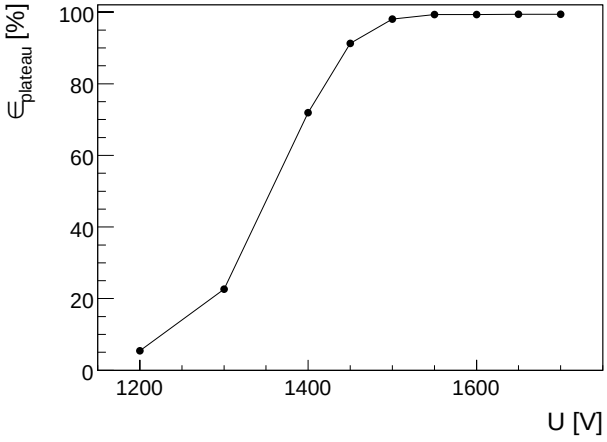

Figure 3.9: Straw tube efficiency at the plateau $\epsilon_{\text{plateau}}$ versus anode voltage U, from Ref. [54]. At the nominal anode voltage of 1600 V, the straw tube is fully efficient.

3.3.3 Straw Tubes in the OT

The longest OT channels measure up to 2.4 m. The channel efficiency and resolution should be uniform over the entire channel length. Besides signal transmission effects described in Section 4.2, the uniformity of the straw tube response depends mainly on the gas gain uniformity.

In its turn, the gas gain is influenced by many factors, of which the straw tube geometry is the most important. When the cathode surface is not circular or the anode wire is not properly centred, the electric field will deviate from the potential described

by Eq. (3.6) and consequently the gas gain will change. By the production method of winding straw tubes on a mandrel, the shape of the tubes is guaranteed to be circular and variations in diameter among tubes are in the order of 10 μm.

To ensure a resolution of 200 μm, the requirement on the wire pitch precision is set to 100 μm. In addition, as can be seen from Fig. 3.10, a deviation of 200 μm from the straw tube centre gives rise to variations in the gas gain of a few percent, and hence the uniformity of the straw tube response.

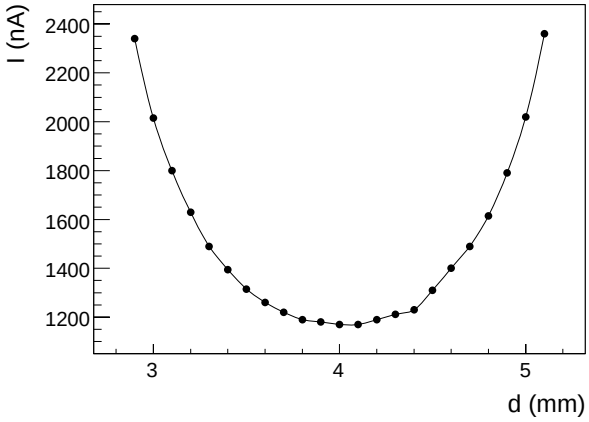

Figure 3.10: Straw tube current I versus wire position d, while irradiated with a source. The current is directly related to the gas gain; the wire is centred in the tube at an arbitrary offset of $d = 4$ mm.

Inside the straw tubes, the anode wires are strained to keep them straight and centred. To avoid wire creep and subsequent rupture, the tension must be well inside the elastic region. Because of its mechanical properties, tungsten is the preferred wire material. The critical tension for 25 μm diameter tungsten wire is reached with a load of about 110 g, the nominal load is set at 75 g.

At the nominal 1600 V anode voltage, the wires will be attracted by the grounded cathodes, and they are pulled away from the centre of the straw tube, thereby reducing the distance between anode and cathode and thus increasing the gas gain. When the displacement is too large, the straw tube can no longer efficiently be operated in the proportional region. Tungsten wire of 25 μm diameter, strained at 75 g, can be used in straw tubes up to 1 m length without additional supports. To operate the foreseen channel length of 2.4 m, wirelocators are designed to support and centre the wire at every 80 cm with 50 μm precision. Apart from high mechanical precision, these pieces are designed to withstand the voltage between anode and cathode without inducing leakage currents or breakdown. Furthermore, the counting gas can flow through unhindered. In Fig. 3.11, a drawing of a wirelocator is shown.

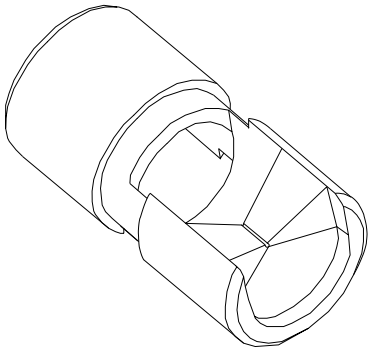

Figure 3.11: Drawing of a wire locator. The cylinder diameter is 4.9 mm, its length is 9 mm. It is designed in two symmetrical halves: the wire is centred by a V-shape in $\vee\ \wedge$ arrangement at either end of the locator.

At the ends of the straw tubes, the electric field is no longer cylindrical. To avoid regions or spots with extreme gas gain values, endpieces are designed to be inserted in the tube ends. Drawings of an endpiece and a straw tube attached to the endpiece are shown in Fig. 3.12. Similar to the wirelocators, these parts centre the wire and guide the gas flow. Individual straw tubes are equipped with endpieces. The assembly of a straw tube equipped with endpieces is positioned independently, allowing for tolerances between straw tubes to accommodate for small deviations in tube dimensions and wire pitch rather then to rely on exact dimensions of the individual components. Since many wirelocators and endpieces are needed, they are produced through injection moulding of radiation hard NORYL plastic.

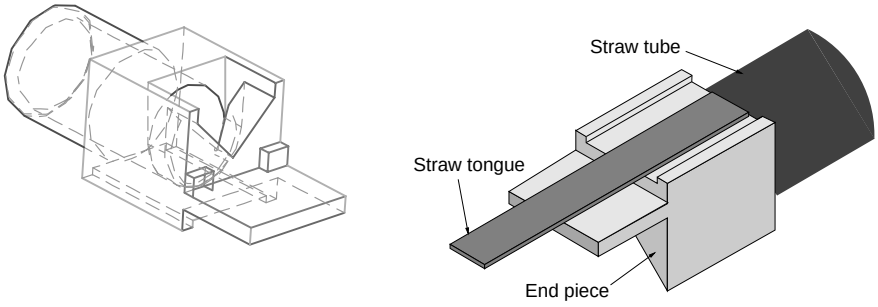

Figure 3.12: On the left, a drawing of the straw endpiece is shown. The cylindrical part is inserted in the straw tube, leaving room for the contact tongue as shown on the right.

3.3.4 Selection of Anode and Cathode Materials

An important requirement for the straw tubes is to allow stable operation under particle fluxes exceeding 60 kHz cm^{-2} and an accumulated dose reaching 100 krad in 10 years of detector operation. Whether or not the counting gas contains CF_4, drift cell performance should be conserved and the anode and cathode must not deteriorate under charge deposits of multiple C cm^{-1}.

For the anode wire, several experiments using wire chambers in high-rate environments share good experience with gold-plated tungsten wire as anodes. Research performed by the ATLAS TRT collaboration [58] indicates that when the gold plating is thick enough and free of cracks and pores, little damage due to ageing is to be expected [55].

For the cathode material, a more rigorous selection procedure is used, with three main requirements:

- it has to be conductive for the removal of the ion current,
- it has to be inert for ions and radicals of the counting gas constituents, and
- it has to remain stable up to several Mrad integrated dose and a high deposited ion charge.

Profiting from experience gained on the tracking systems in the HERA-B [59] and COMPASS [60] experiments, carbon-loaded polycarbonate (Pokalon) and polyimide (Kapton) foils were considered as cathode materials. Carbon-loaded Kapton, known as Kapton XC, is extensively tested by the ATLAS TRT collaboration [58] and finally selected as their cathode material. It is validated to be resistant to many Mrad integrated dose and large deposited charges up to several C cm^{-1}.

Apart from the experience gained elsewhere, both Pokalon and Kapton XC foils were subjected to extensive testing as described in Section 3.4. Based on the material availability and the outcome of the tests, Kapton XC is the cathode material of choice for the OT.

Plain Kapton is an excellent insulator. It is made conductive by a volume doping of carbon: with 25% volume consisting of soot particles, the resistance is brought down to several hundred Ω/square. Given that the precise cathode resistance is unimportant to the drift cell performance, the thinnest and lightest foil available, Kapton XC-160, is selected.

Straw tubes are produced by winding ribbons of foil material on a mandrel, illustrated in Fig. 3.13. The inner layer consists of Kapton XC, the second, staggered layer is wound on top to provide gas tightness of the straw tubes. The outer layer does not have to be conductive, but the other two cathode requirements have to be fulfilled since this layer is partly in contact with the counting gas. By using a Kapton-Aluminium laminate, the requirements are met, and in addition electrical shielding of the straw tube is provided.

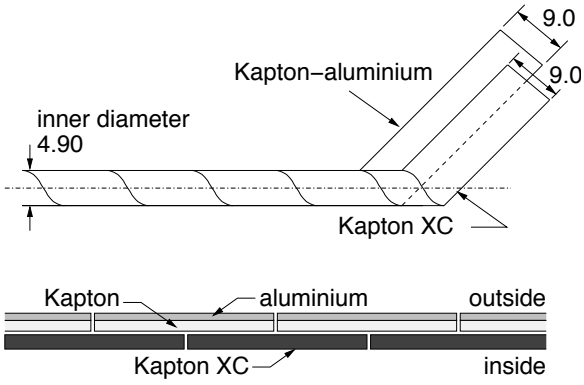

Figure 3.13: Winding pattern of the straw tubes. A tube is wound from two 9 mm ribbons staggered by half a winding cycle, as illustrated on top. The inner winding is Kapton XC, the outer is a Kapton-aluminium laminate. The lower part of the drawing contains a cross section of the straw tube wall, showing the layer arrangement.

3.4 Ageing Tests

The OT operates in a hostile radiation environment with particle fluxes over 60 kHz cm^{-2}, see below, and collects an integrated dose up to 100 krad in 10 years of operation. This necessitates ageing studies to ensure proper operation during the intended lifetime of the OT detector.

Radiation Damage

The LHCb detector is exposed to different kinds of particles covering a large energy range. The ionisations caused by charged particles in the counting gas are the means by which they are detected; unfortunately they also cause ionisations in all other detector material, resulting in material degradation in the long term. Apart from charged particles, photons and neutrons cause material damage from non-ionising energy loss. In particle flux simulations, neutrons with energies below the thermal region are taken into account, since many materials have a high cross-section for nuclear reactions involving thermal neutrons, in which additional particles are emitted.

Radiation induced material degradation often results in the loss of mechanical properties; in general materials become more brittle and less resistant to stress and strain. Furthermore, radiation can alter the electrical conductive properties of materials. For the OT operation, it is crucial that the straw tube walls, acting as cathodes, remain conductive. On the other hand, insulating parts, the wirelocators for example, must retain their insulating properties to avoid leakage currents or breakdown.

Accelerated Ageing Tests

Detector ageing is carefully studied by conducting ageing tests. To reach conclusive results in reasonable timescales, accelerated tests are performed with elevated radiation levels. The acceleration factors must be limited, since tests involving extremely high dose rates over very short time spans cannot be considered realistic ageing tests for detectors in the LHCb experiment.

The gas mixtures used in the tests contain CF_4 which is assumed to induce ageing effects faster and more severe then gas containing only argon and CO_2.

In the presence of CF_4 in the counting gas, fluorine radicals ($F\cdot$) are formed under irradiation. Many materials are not resistant to $F\cdot$, including some metals that can be etched away by it. Tests are conducted to investigate whether $F\cdot$ is formed in counting gas of interest and whether it attacks the foil materials under study for use in the OT. From these experiments, Kapton XC emerged as the prime candidate for the cathode foil [61]. In further ageing tests, radiation tolerance and ageing damage is studied in both single drift cells as well as entire modules.

Three types of tests have been performed:

1. Cathode ageing from accumulated radiation dose. Straw tube proportional counters are operated in a 11 MeV proton beam. Since most of the protons are stopped in the cathode material, it rapidly accumulate a large dose.

2. Charge deposition of counting gas ions and radicals. By operating straw tube counters under irradiation, the anode and cathode stability under large deposited charges is investigated. For convenience, radioactive sources and X-ray tubes are used to irradiate the straws.

3. Ageing of an entire module in a realistic environment. An OT prototype module is incorporated in the HERA-B experiment, where a similar variety and flux of particles is present as is expected in LHCb.

Accumulated Radiation Dose

Materials are degraded when a large radiation dose is accumulated. The cathode foils are exposed to counting gas ions and radicals. Unlike the metal anodes, the cathodes are made of plastics and therefore are the most susceptible to radiation damage. To study the effects of a large accumulated radiation dose on straw tube performance, single straw tube proportional counters are operated in a 11 MeV proton beam. The test extended to an accumulated dose of 0.7 Mrad, after which the stability of the straw tube counter was not affected. The highest dose expected for the OT is about 100 krad in 10 years for regions close to the IT, depending on the final design of the VELO detector and the beampipe [48,62]. To minimise the risk of detector degradation, only materials certified to be radiation tolerant are used in the detector construction.

Deposited Charge

Anode and cathode materials of choice must be tested to be resistant to large deposits of gas ions and radicals created in the gas amplification process, as described in Section 3.3.1. To investigate the effects of degradation due to the integrated ion charge, the particle fluxes and the consequent charge deposits must be estimated. Using simulation tools as described in Chapter 5, the highest particle flux in the OT is expected at the corners of the IT as indicated in Fig. 3.14.

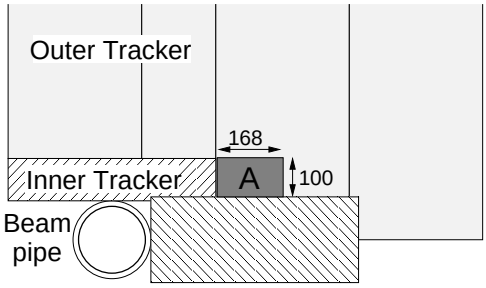

Figure 3.14: Schematic picture of the OT and IT arrangement around the beampipe for a quadrant of a tracking station. The surface with the highest particle flux is marked 'A'. Its dimensions in mm are indicated.

Averaged over 16.8 cm in x, and 10 cm in y, the highest particle flux in the LHCb OT is 63 kHz cm^{-2} when operated at a luminosity of 5×10^{32} cm^{-2}s^{-1}. If the charged particles are assumed to be minimum ionising particles (MIPs), the average charge deposition in the counting gas per particle can be calculated. In an Ar(70%)-CO_2(30%) gas mixture at STP, a MIP creates about 93.1 electron-ion pairs per cm [50]. In a drift tube with diameter $d = 4.90$ mm, particles travel on average through $d\pi/4 = 3.85$ mm of counting gas. Typically, a MIP will create 35.8 primary electrons in a straw tube.

At 1600 V anode voltage, the gas-gain in Ar(70%)-CO_2(30%) is measured to be 7×10^4 [63]. As a result, the primary electrons liberated by a single MIP cause a charge of 0.4 pC to be deposited on the anode and cathode.

In the hottest region of the OT, integrated over 10 years ($10^8 s$) of running at high luminosity, the aforementioned assumptions lead to a deposited charge of 1.3 C cm^{-1}.

Before conducting elaborate ageing tests with large deposited charges, initial ageing tests were carried out on straw tube chamber prototypes using a radioactive source. For these tests, a ^{90}Sr source is used, emitting electrons up to 2.3 MeV. By operating the straw tubes in proportional counter mode while exposing them to the source, charge is accumulated on the cathode tubes and anode wires. The ion current at the anode is monitored to estimate the total dose received by the drift cell. For accumulated charges up to 374 mC cm^{-1}, no ageing effects were observed [61].

Subsequently, straw tubes were exposed to X-rays. The straws can be tested up to large charge deposits in a controlled environment by using an X-ray tube for the

irradiation. In this test, where charges up to several C cm^{-1} are deposited on the anode and cathode, some wire ruptures were observed [57] when the counting gas contained CF_4. Consequently it was decided to operate the LHCb OT without CF_4.

Of course, irradiation with electrons from a ^{90}Sr source or X-rays from an X-ray tube cannot be considered a realistic simulation. To mimic the radiation environment present in LHCb, a test with hadronic particles is performed

Ageing in a Realistic Environment

To test ageing effects on an entire chamber rather then on single straw tubes, a realistic chamber prototype is inserted in the tracker of the HERA-B experiment. The variety and flux of particles in HERA-B is assumed to be similar to LHCb. Hadrons are present at a wide energy spectrum: from minimum-ionising particles to slow protons and neutrons. Operation in this environment is difficult to simulate in a laboratory ageing test. For several months the chamber was operated in the high-flux environment near the beampipe of the experiment. Before and after the test, the chamber straw tube performance was monitored using a ^{90}Sr source. From the monitored data, no deterioration due to the radiation received in the HERA-B experiment has been observed.

3.5 Module Design

Straw tubes are the active detector elements of the OT. Unfortunately, the OT detector cannot be constructed from straw tubes alone, since they lack necessary mechanical properties. Over the 2.4 m maximum length, straw tubes are not self-supporting, nor straight, nor gas-tight. Therefore an external envelope is needed, which has the following requirements:

- It should introduce little material in the acceptance. In order not to exceed the momentum resolution specification defined in Section 3.2.1, the OT should not exceed a thickness of about 3% of X_0 per station.
- It must be gas tight. Considering the volume of the straws, the foreseen flow rate and the requirements on the gas quality [64], the leak rate should be less then 8×10^{-4} l s^{-1} [63].
- It must be sufficiently rigid to resist overpressure. To enable a well-defined flow of the counting gas, some overpressure is necessary. Including a safety margin, a 10 mbar overpressure must be tolerated.
- It has to withstand the tension of the strained anode wires without significant deformation.
- It should have the mechanical stability to ensure the detector position within 100 μm (500 μm) in the $x(z)$ direction.
- It has to shield the anode wires from external electromagnetic influences.

- It should provide the necessary interfaces to the gas, high voltage and readout services.

The design of the OT is modular: stations consist of layers, station layers are composed of modules. A module acts as a separate detector; it is mechanically stable, gas tight and capable of stand-alone operation.

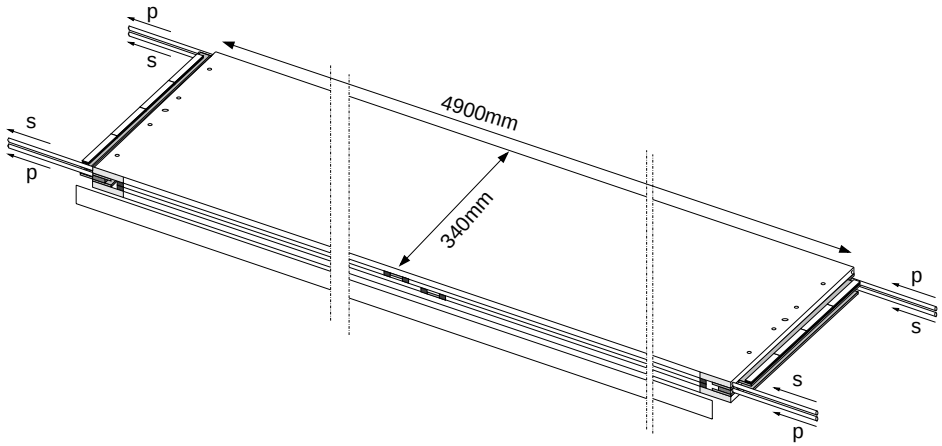

Figure 3.15: Drawing of an OT module with its overall dimensions. The gas flow direction for in- and outlets of the primary p and secondary s volumes are indicated. In the drawing, the sidestrip is removed, allowing a view of the module internals.

Fig. 3.15 contains a drawing of the module designed to satisfy the above-mentioned requirements. A single module provides full geometrical coverage: it contains two monolayers of 64 straw tubes each, arranged as displayed in Fig. 2.10. A module containing the straw tubes is constructed from two panels joined together by sidewall strips to form a box surrounding the straw tube layers. Endpieces close off the module ends.

The module is mechanically loaded by the anode wire tension and the counting gas overpressure.

The force introduced by a single monolayer equals the wire tension of 64 straw tubes. Halfway the module where straw tubes of the top and bottom detector half are separated, the anode wires are mechanically connected to a printed circuit board, so no net forces are exerted at the separation zone of the straw tubes. The resulting load for two monolayers is 9.6 kg, directed along the panels.

The gas overpressure results in forces perpendicular to the panel which are more difficult to withstand. Due to the larger density of the main component of the drift gas, argon, at 20° temperature an overpressure of 1 mbar is present at the bottom of the module. To retain a controlled gas flow, another 2 mbar overpressure must be present

inside the module. The panel strength and stiffness is designed with these loads in mind. Lightweight materials are used to restrict the material budget: panels are made of a 10 mm thick Rohacell core covered on both sides with 90 μm thick carbon fibre skins. 400 μm thick carbon fibre sidewalls connect the panels and stiffen the module.

Straw tubes wound from Kapton windings only are observed to elongate with increasing humidity. Up to 1.5% elongation is observed when the relative humidity is raised from 0% to 55%. When aluminium is used for the outer windings, no significant elongation is observed.

With straw tubes glued to a panel, eventual elongation of the straw tubes strains the glue joint between the straws and the panel. This could lead to buckling of straw tubes or glue joint failure. During detector operation, dry counting gas is surrounding the straw tubes. By storing the tubes in equally dry environment and by performing the module assembly in a controlled atmosphere with 50% humidity, expansion of the tubes is avoided. Eventual remaining stresses are handled by the module; full-scale tests did not reveal any problems related to humidity.

In high-rate environments as present in LHCb, a clean counting gas is extremely important to avoid detector deterioration through ageing [55]. To avoid pollution of the counting gas with contaminating elements entering through diffusion or small leaks, two gas volumes are introduced in a module. The straw tubes define the primary volume, which has its own gas feed and exhaust. The secondary volume surrounds the strawtubes and is defined by the module panels, sidestrips and endpieces. The inner side of the panels is covered with an extra layer Kapton-aluminium foil laminate for gas tightness of the secondary volume. An illustration of the two gas volumes inside the module and their gas flows is included in Fig. 3.16. With two independent gas flows, the leak rate requirement of $8{\times}10^{-4}$ l s^{-1} is met and the OT drift gas quality stays within specifications [64].

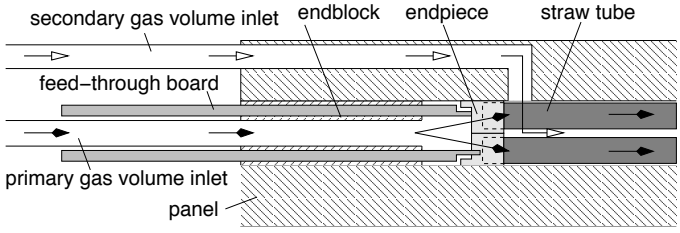

Figure 3.16: Cross-section of the module edge with the division of primary and secondary gas volumes. The module panels, sidestrips and endpieces define the secondary gas volume, the straw tubes define the primary volume.

The ends of the panels are equipped with aluminium inserts. The assembly of two panels is closed with a endblock. The gas in- and outlets and feed-through boards are attached to the endblocks. The feed-through boards contain solder pads for the anode wires and shielded leads to the front-end electronics connectors..

For a reliable ground contact of both the Kapton XC inner winding and the aluminium outer layer of the straw tube, so-called tongues are cut at the straw tube ends, as shown in Fig. 3.17. Straw tube tongues are connected by a crimped contact to the feed-through board, providing a solid connection to the ground plane used by the front-end electronics. More background on the interface between the straw tubes and the on-detector electronics is found in Chapter 4.

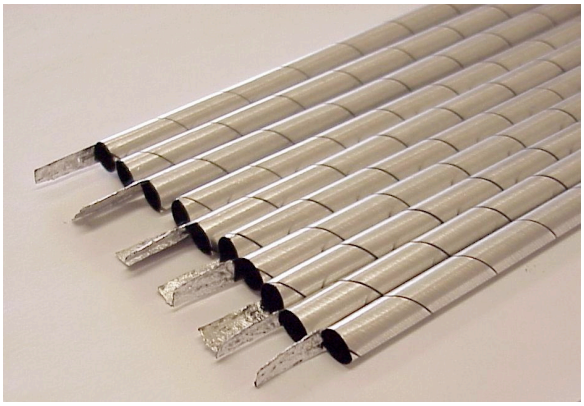

Figure 3.17: Straw tubes with tongues for the ground connection to the inner conductive Kapton XC cathode layer and the outer layer of Kapton-aluminium laminate.

For occupancy reasons, straw tubes are read out at the upper and lower ends of the module independently. Both anode wires and straw tubes are interrupted halfway the module as illustrated in Fig. 3.18. To avoid an insensitive zone in the OT, the region where straw tubes are separated is staggered in the y direction. The staggering arrangement is optimised for track reconstruction performance [65]. A practical consequence is that the straw tube length differs on both sides of the separation zone; two lengths of straw tubes are present in a single module.

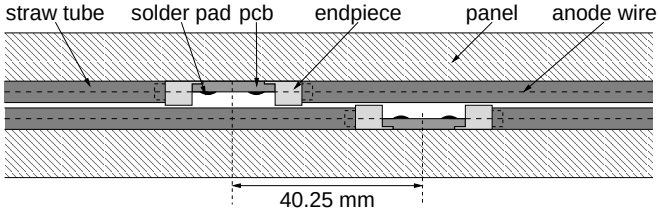

Figure 3.18: Drawing of the straw separation region halfway a module.

Above and below the IT, the OT contains half-size modules. The dimensions of these modules are adapted to the IT shape; modules differ in length, and modules containing 32 channel wide layers are incorporated.

The contributions to the material budget from individual components of the OT detector are listed in Table 3.1. The total OT thickness is 2.98% of X_0. By using lightweight composite materials, the amount of material introduced by the panels is limited. The modular OT design results in a reliable detector which is easy to repair in the case of module failure. Furthermore, production of a large number of similar modules is less complicated and error prone than construction of a tracker station as a whole.

Material	$x/X_0(\%)$
Panel	0.222
Straws	0.131
Glue	0.019
Total half module	0.372
Total module	0.744
Total station	**2.98**

Table 3.1: Material budget of a OT station in x/X_0 with the contributions from the individual components.

3.6 Module Production

After a research and development programme, a final module design was defined and module production started in 2004. Of the OT stations, the surface around the IT is covered by modules of different length and width, labelled 'S', which account for 25% of the OT surface. The other 75% is covered by a single module type, labelled 'F'. 168 of these F-modules have to be produced. In Fig. 2.11, the module types are indicated. The large number of modules calls for a mass production procedure, which is described below.

3.6.1 Production Procedure

Ideally, a straw tube monolayer consists of perfectly straight tubes at the exact pitch in a flat planar arrangement. In reality, straw tubes are not straight by definition and the module panels are not guaranteed to be flat. Straw tubes need to be straight for stable operation and uniform response characteristics, therefore following tolerances apply to the position of straw tubes relative to the nominal position in an perfect monolayer:

- the maximum deviation in x is $100\,\mu$m, and
- the maximum deviation in z is $500\,\mu$m.

To reach this accuracy in a production procedure, an external precision jig is required to position the straw tubes relative to each other and to guarantee the straightness while the straw tubes and the panel are glued. The glue joint accommodates the panel unevenness with respect to the straws aligned in the jig. The jig consists of a slab of solid aluminium with machined grooves in which the straw tubes are placed. The position and straightness of the jig grooves are verified to be within 50 μm from an ideal geometry.

The ensemble of straw tubes, endpieces and PC-boards are glued together on a panel to form the assembly sketched in Fig. 3.18. All components are positioned in the jig as can be seen in on the photo in Fig. 3.19 before the panel is glued.

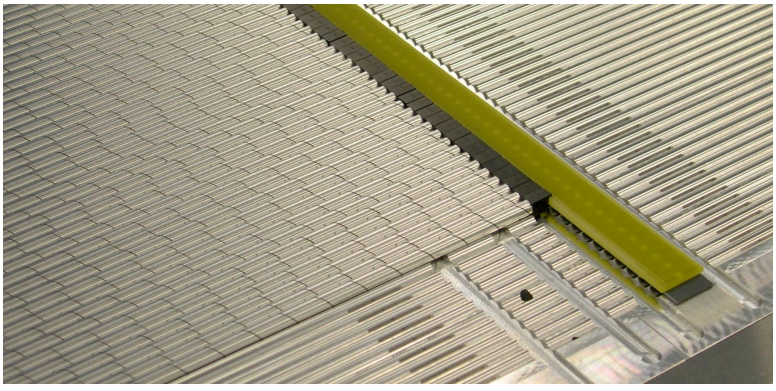

Figure 3.19: Photograph of straw tubes in the jig at the straw tube separation zone halfway the module. The straws, endpieces and pc-boards can be seen at the picture; a cross-section of the assembly is sketched in Fig. 3.18.

Using a jig as described, modules are assembled in module halves consisting of a panel with a monolayer of straw tubes glued onto it. The assembly of a half-module comprises the following steps:

1. Straw tubes are cut to length, with the tongue providing the ground contact on one end. Ground contacts are crimped to the straw tubes.
2. Straw tubes are equipped with wirelocators and endpieces (see Fig. 3.11 and 3.12).
3. Straw tubes are placed in the jig, together with the feedthrough boards.
4. The straw tube ground contacts are soldered to the feedthrough boards, see the top photo in Fig. 3.20.
5. The module panel is positioned in a dedicated tool and glued to the straw tubes and feedthrough boards in the jig. This stage is displayed in the bottom photo of Fig. 3.20.

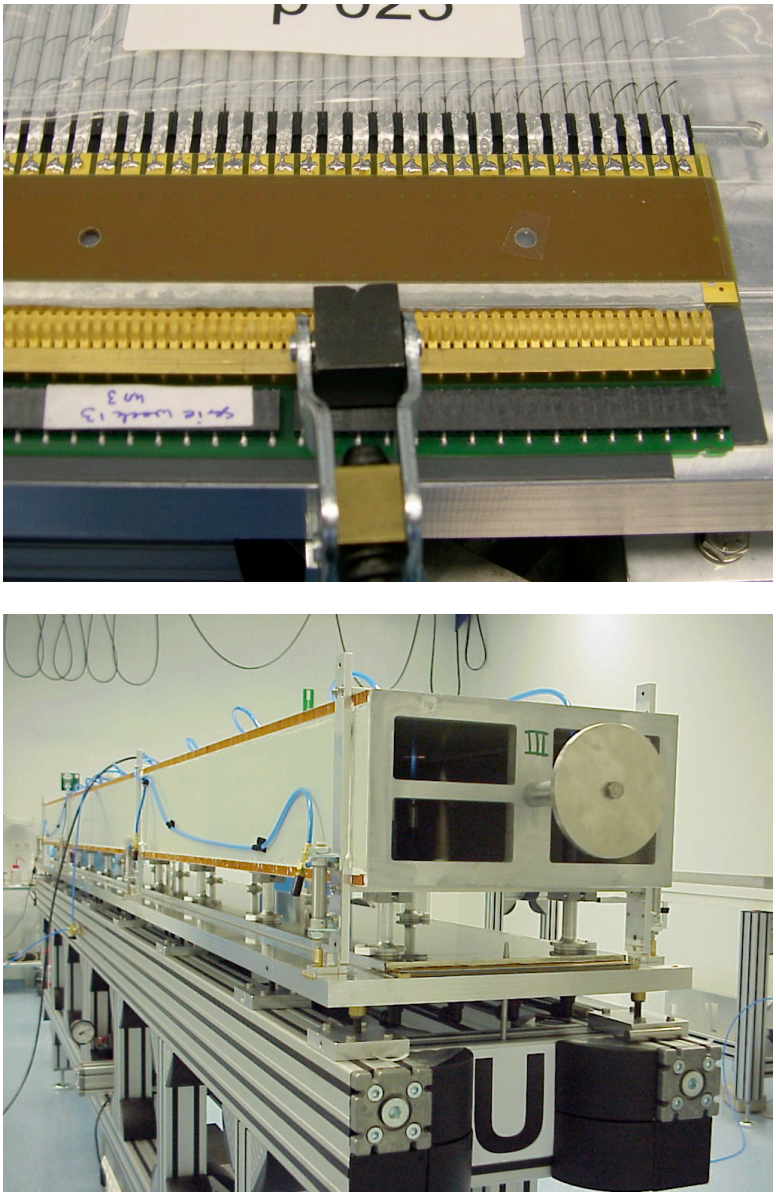

Figure 3.20: Photographs of the production procedure stages and tools.
On top, the end of the module is shown, with the straw tube tongues and the connection to the feed-through board.
In the bottom picture, the panel, held by its handling tool, is glued to a layer of straw tubes in the jig.

6. After the glue has cured, the straw tubes are equipped with anode wires, which are strung to the correct tension and soldered.

After completion of the assembly procedure for a half-module, several tests are carried out while the module internals such as anode wires are still reachable. Upon completion of the tests, approved module halves are joined to a module. Subsequently, the gas tightness is tested. After that, the correct operation of the module is ensured through a series of tests which are discussed in the following section. When a module has successfully passed the tests, it is accepted for use in the OT.

3.6.2 Module Tests and Quality Control

Before two module halves are joined, there is still opportunity for repairs in the case of failures. After a visual inspection, channels are subjected to the following tests as described in Ref. [63]:

- At the ends of the straw tube, the wire position is measured. The deviation should be within 100 μm from the straw tube centre.
- After the wires are strung and soldered, the wire tension is determined by detecting the resonance frequency in a magnetic field [66]. When a deviation larger then 5 g from the 75 g nominal tension is detected, the wire is replaced.
- When the wire tension of all wires are checked to be within the specifications, they are put on high voltage (HV) while in air. The current is monitored continuously while the anode voltage is ramped up to 1600 V. If a wire draws a current over 20 nA at 1600 V, the wire is declared bad and replaced.

Once all channels on the module halves have passed these tests, the halves are joined to a module. The assembled module is checked on gas tightness. An overpressure of 7 mbar is applied to the module gas volume, and the overpressure decay rate and the leak rate are measured. If the leak rate is below the specification mentioned in Section 3.5, the module is accepted.

The next test is the so-called HV-training. The module is flushed with counting gas after which HV is applied. It is observed that occasionally wire currents are initially high but stabilise at normal values of around 1.0 nA in a few hours. When the HV-training is completed and all channels are validated, the chamber is exposed to a radioactive source to check the performance.

For the chamber performance check, a ^{90}Sr source is used. It is a β-source, emitting electrons with energies up to 2.3 MeV which is sufficient to traverse the straw tubes inside the module. The source is mounted on a carriage which can be moved along the full length of the module. The module is scanned by moving the source in 1 cm steps and reading the corresponding ion current from the channels in a monolayer. The resulting measurement curve indicates the uniformity of the response along the full wire length.

The result of a module scan is depicted in the left plot in Fig. 3.21. The vertical white lines indicate the regions where the wirelocator inside the straw tube renders the

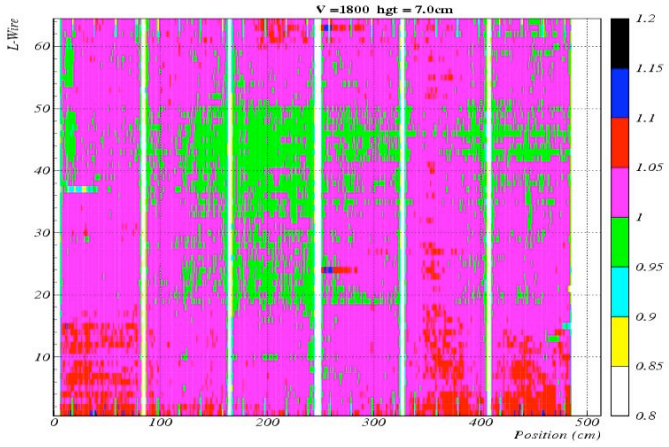

Figure 3.21: Response of the straw tubes in a monolayer to radiation of the ^{90}Sr source versus its position along the wire. For all wires, the relative current is plotted. The inefficient regions where the wirelocators are placed can clearly be seen in white.

.

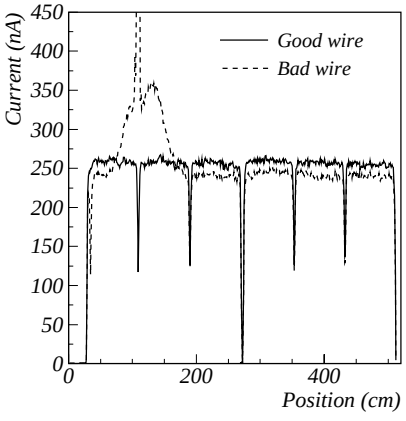

Figure 3.22: The response of two channels to irradiation from a ^{90}Sr source versus its position along the wire. The inefficiencies caused by the wire locators and the straw tube separation halfway the module are clearly seen. The dotted line is the response of a channel where a missing wire locator is causing an excessive current.

drift cell inefficient. The plot in Fig. 3.22 displays the channel response to a scan of two independent channels. A uniform channel response is plotted with a solid line: the dips in the response are caused by the wirelocators. The dashed line is the response of a channel with a missing wirelocator, which is clearly seen from the current excess in the plot.

The response to the ^{90}Sr irradiation is used to validate the module, and also to monitor whether the production method for the module is sound. If abnormal responses are found from the ^{90}Sr scan, the module response can be examined using a ^{55}Fe source. The ^{55}Fe source emits monochromatic photons of 5.9 keV. The greater part of the photons reaching the counting gas are absorbed through photo-absorption, leaving about 220 primary electrons in the gas. The height of the corresponding pulse at the anode is determined by the gas gain, independent of the material traversed. It is common practise to examine wire chambers this way but it is more elaborate, it requires sensitive pulse-height measuring electronics and it takes time to gather sufficient statistics. During production, samples of the total production are subjected to the ^{90}Sr scan. If anomalies are found, the module is checked using the ^{55}Fe source. Besides verification of the correct workings, systematic deviations provide feedback to the production method. For example, a batch of bad anode wire can be traced back from excessive variations in the ^{90}Sr scan response.

3.7 Station Design

The four layers of straw tube modules in a station are mounted on an aluminium frame. For servicing and repairs, stations are built in halves which close around the beampipe. For simplicity, both the OT, the IT detector and its mounting frame is suspended by the same structure.

An overview drawing of the LHCb magnet, beampipe and the tracker stations and their support structure is included in Fig. 3.23.

A spacing of 25 mm in z is kept between the module layers to obtain sufficient lever arm for a slope measurement of track segments. One x and one stereo angle layer of modules are mounted with dowel pins on 10 mm thick aluminium precision ruler beams. The pin hole positions on the beams define the module position with respect to reference points on the beams. A single station is built from four 'C-frames', each frame carries two layers of modules for half the station width. A C-frame embodies precision ruler beams at the bottom and at the top, connected by an aluminium structure outside the tracker acceptance. Fig. 3.24 shows a drawing of a C-frame and modules. In between the ruler beams and sides, sufficient space is reserved for the guidance of cables and services necessary for detector operation such as gas supplies and cooling water lines.

The C-frames facilitate opening and closing of stations for maintenance and repairs of the IT and OT detectors. After closing a station, the positioning of two halves will not be reproducible better than a few tenths of a mm. Moreover, temperature effects can introduce additional uncertainties in the station positions. Therefore, the tracker is equipped with a RASNIK alignment system [67], which provides information on the

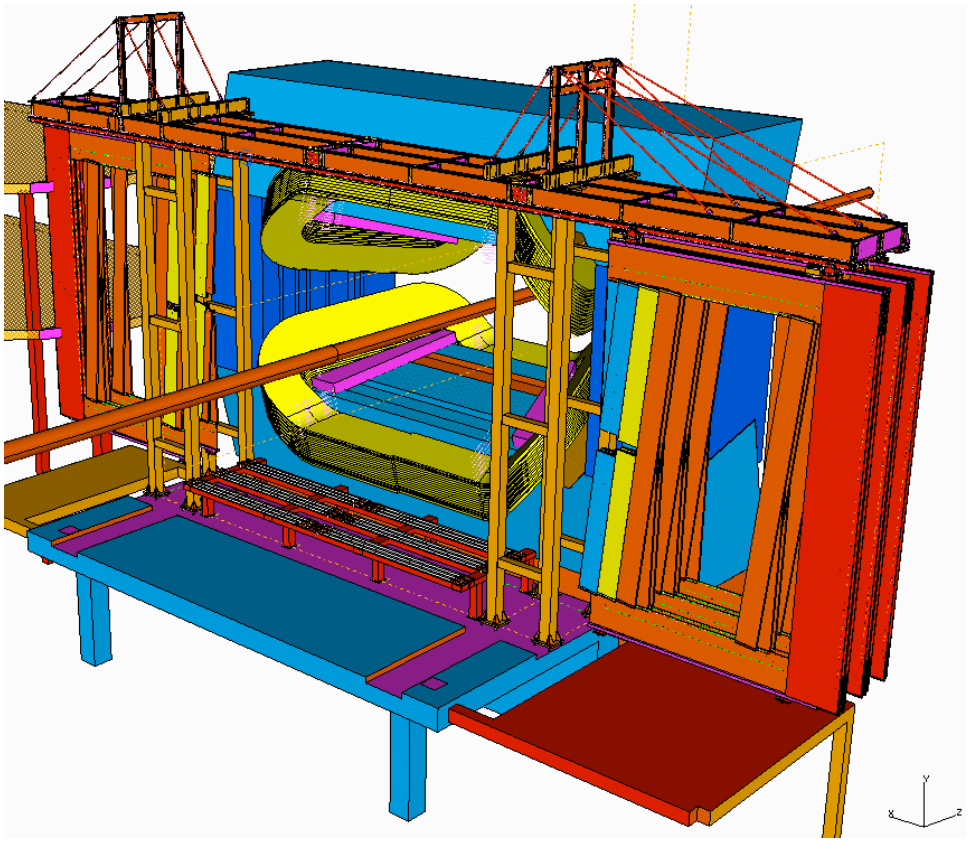

Figure 3.23: Overview solid model drawing of the tracker stations with their support structure and the magnet, viewed in upstream direction. In front of the magnet, the station support structure is visible. The stations are retracted from the beampipe, for simplicity only a few modules are drawn.

relative position of the three stations and station halves.

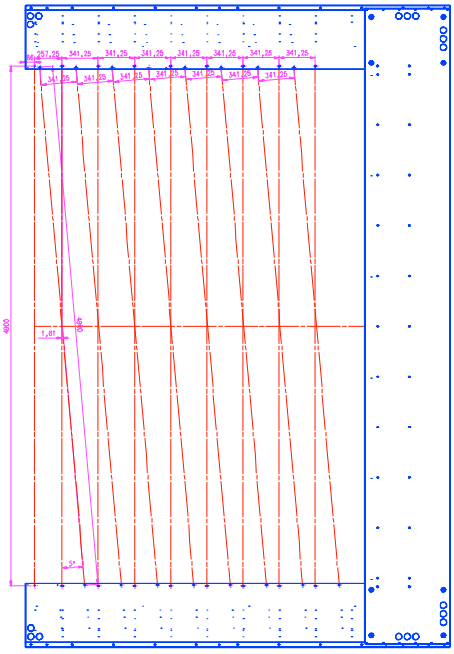

Figure 3.24: Drawing of the C-frame of half the station width, capable of suspending two layers of modules. Modules are attached to the precision beams on top and at the bottom.

3.8 Summary

In this chapter, the design of the LHCb OT is presented. The three OT stations have a common support structure, the C-frames. Two C-frames form a station halve. The frames are equipped with detector modules, which are capable of stand-alone operation. A single module contains 128 straw tubes. The straw tubes have an inner diameter of 4.9 mm and are arranged in monolayers at 5.25 mm pitch. To provide full geometrical coverage, a module houses two staggered monolayers. Most modules stretch along the full detector height; for occupancy reasons, channels are separated halfway in these modules.

Straw tube drift cells filled with Ar(70%)-CO_2(30%) are the active elements of the OT. In beam tests, a spatial resolution better then 200 μm has been achieved. The resolution, in conjunction with the low amount of detector material present in the acceptance, is sufficient to provide a track momentum measurement with a precision better then 0.5% for tracks with momenta in the 2 to 100 GeV/c range.

The straw tubes have a limited drift time of 42 ns. The drift time exceeds the 25 ns spacing between two successive bunch crossings of the LHC: an OT detector sample will contain hits from neighbouring events, thereby increasing the occupancy. Even at high luminosity, the 10% occupancy limit set by the pattern recognition software is not exceeded, and the expected hit rates can be easily handled by the straw tubes.

The OT has to operate for 10 years in a harsh radiation environment, therefore it is built from materials that are certified to be radiation hard. The cathode material is carefully selected on its resistance to total accumulated radiation dose and stability under large deposited charges by counting gas ions and radicals. Both at the level of single drift cells as well as entire modules, the OT has been subjected to ageing tests. No major obstacles have been encountered so far. The use of CF_4 in the counting gas reduces the OT response time and thus occupancy. However, the presence of CF_4 in the drift gas is correlated with wire ruptures and is therefore abandoned.

The detector performance is determined by the straw tube drift cells in conjunction with the readout electronics. In the following chapter, the interface of the straw tubes with the preamplification stage and time measurement performance are discussed.

Chapter 4

The Outer Tracker Readout

The LHC machine reaches its high luminosity by a 40 MHz bunch-crossing frequency. A consequence is that the detectors used in LHC experiments need to have a short response time to unambiguously assign detector responses to bunch crossings. In conjunction with the detectors, the readout electronics must be compatible with the speed demands of the LHC experiments.

In this chapter, the readout electronics of the Outer Tracker (OT) and the interface with the straw tubes are presented. In addition, the performance and physics consequences of the preamplifiers and Time to Digit Converter (TDC) are discussed.

4.1 Outline of the Readout System

The LHCb subdetectors provide a pulse height measurement with a 25 ns response time, except for the OT. Here, the timing of drift tube signals is measured. By recording the time between particle impact and the arrival of the resulting signal, the impact location is determined. The maximum signal collection time exceeds a single bunch crossing interval; the OT straw tubes have a readout sample window of 75 ns. Subsequent bunch crossings generate responses in straw tubes with 25 ns spacing, consequently an OT event can contain hits from preceding as well as subsequent bunch crossings.

The OT readout electronics reside on the upper and lower edges of the detector. Here the integrated dose accumulated in 10 years of operation is expected to be 2 krad [48]. To ensure reliable operation, only radiation hard electronics are used on-detector.

The Level-0 (L0) and Level-1 (L1) electronics requirements are extensively documented [68, 69]. As described in Section 2.10.1, on-detector electronics accommodate the L0 trigger buffers, whereas the L1 trigger electronics are located off-detector, in the counting room.

4.2 Straw Tube Proportional Counter Signals

In straw tube proportional counters, the signal is formed by the electrons and ions liberated in the gas amplification process, drifting towards the anode wire and cathode

surface respectively, see Section 3.3.1.

4.2.1 Electrostatic Configuration

In the LHCb OT, positive high voltage (HV) is applied to the anode wire. The straw tube walls, acting as cathodes, are grounded. The anode wire is connected to the preamplifier input with an insulation capacitor to decouple the HV from the preamplifier. Fig. 4.1 contains a schematic of the straw tube connections. The capacitor and the preamplifier input impedance act as a high-pass filter, effectively eliminating unwanted low-frequency components.

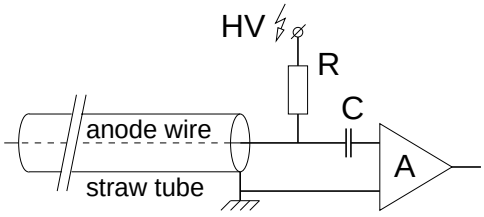

Figure 4.1: Schematic of the straw tube connections. The High Voltage (HV) is connected through a series resistance R to the anode wire, the straw tube wall acting as the cathode, is grounded. The preamplifier A is isolated from the HV by the insulation capacitor C.

The straw tube walls are made from Kapton XC, of nonzero resistance. The HV is connected to the anode wire with a series resistor of 1 MΩ to limit the current to a few mA in case of a short circuit between cathode and anode. The ion current running through both resistances causes a small voltage drop, reducing the HV. With the conservative assumption of a 2 MHz minimum-ionising particle rate for the hottest OT channels, the ion current is well below 1 μA. With the HV series resistance and a cathode resistance of 30 kΩ m^{-1}, the voltage drop is about 1 V. A 1 V drop in the HV results in a reduction of the gas gain of about 1%, which has a negligible influence on the timing of the signal leading edge. Hence, no resolution worsening has been observed as a result from such small HV variations.

4.2.2 Signal Formation and Transmission

Signal generation

A straw tube response is generated from the drift of the electrons and ions created in the gas amplification process. While they drift towards the anode and cathode respectively, they gain energy from the electric field. Depending on the configuration of the straw tube connections, a signal voltage or current between the anode and cathode is induced. The signal vanishes as the charge carriers are absorbed by the cathode and anode. Practically

all electrons are liberated from the ions in the gas amplification process. Both charge carriers drift through the gas independently, the electrons at much higher speed than the ions. The magnitude of the generated signal depends on the energy the charge carriers gain from the electric field per time interval. Since most of the charge carriers are generated in the high field region close to the wire, the initial signal magnitude is high. Electrons have a short drift path in the region with high electric field close to the wire, while ions drift from the wire to the wall where the field is lower. Due to the short drift distance and high drift speed, electrons generate a short pulse, superimposed on a pulse with a long decay generated by the slower and longer ion drift. The electron signal is described with a step function with an exponential decay with a time constant of 13.2 ns. Since the electric field depends on the distance to the wire r as $1/r$ and the ion drift speed is approximately constant within the electric field range, the ion signal tail behaves as $1/t$, which cannot be modelled by a single exponential. The modelled straw tube signal is plotted in Fig. 4.2.

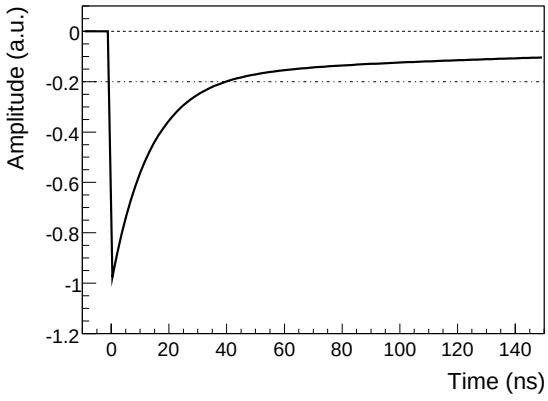

Figure 4.2: Modelled charge pulse for a single avalanche in Ar(70%)-CO_2(30%) counting gas, see text. An arbitrary threshold level is drawn.

The timing of the pulse leading edge is a measure for the distance between the wire and the position the electron was liberated by the particle traversing the straw tube. The leading edge of an avalanche has a sub-ns risetime. Timing of the pulse onset results in the most accurate distance determination.

Signal shape

A single particle traversing a straw tube leaves behind multiple clusters, each inducing an avalanche at the anode wire. The number of clusters depends on the length of the particle path in the detection gas, see section 3.3.2. Clusters generated close to the wire generate an immediate response while clusters generated close to the cathode

generate a signal after a drift time up to tens of ns. The exact drift time depends on the composition of the counting gas and the applied voltage. Due to the 40 MHz LHC bunch-crossing frequency, particles are generated at the interaction point with 25 ns spacing. In addition, the time-of-flight varies for different particles depending on their energy and trajectory in the experiment. As a result, straw tubes are traversed by particles with very small temporal spacing [44].

The preamplifier for the read-out of the straw tubes should be able to discriminate between straw tube responses to different incident particles. However, due to the slow ion tail in the signal, multiple cluster responses will pile up. Fig. 4.3 contains a plot of the pile-up of two responses each consisting of multiple clusters. The leading edges of the second response are clearly recognised around $t = 40$ ns. Due to the signal tails of the first response, the subsequent signals are lifted above the (arbitrary) threshold level for hundreds of ns, making the timing of a second incident particle more difficult.

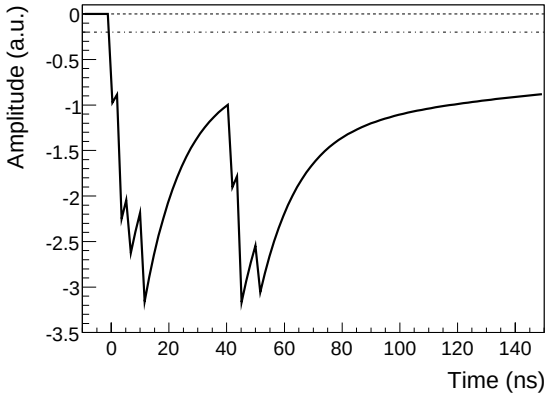

Figure 4.3: Modelled charge pulse of the pile-up of two separate straw tube responses arriving at $t = 0$ and 40 ns respectively. Each response consists of multiple clusters. An arbitrary threshold level is indicated with a dashed line to illustrate the need for tail cancellation in order to recognise the individual responses.

To avoid the second response to go unnoticed, a short deadtime is required. It is necessary to cancel the ion tail signal such that the leading edge of a next cluster can be detected.

Signal transmission

The 13 μm aluminium layer in the straw tube walls and the 25 μm thick anode wire form a cylindrical coaxial transmission line. A transmission line is modelled by the continuum of a discrete series of capacitors and inductors as displayed in Fig. 4.4, with

a capacitance C and inductance L per unit length:

$$C = \frac{2\pi\epsilon\epsilon_0}{\ln(r_c/r_a)} \approx 10.5 \text{ pF m}^{-1}, \tag{4.1}$$

$$L = \frac{\mu\mu_0}{2\pi}\ln(r_c/r_a) \approx 1.06 \ \mu\text{H m}^{-1}, \tag{4.2}$$

where ϵ_0=8.85 pF m^{-1}, μ_0=$4\pi \cdot 10^{-7}$ N A^{-2}, $\epsilon = \mu = 1$, r_c=2.45 mm and r_a=12.5 μm.

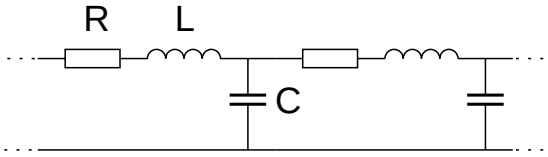

Figure 4.4: Model of a transmission line as a discrete series of capacitors (C), inductances (L) and resistors (R).

The sub- ns risetime of the straw tube signals is much smaller than the pulse transmission time of the straw tube, which exceeds 10 ns for a 2.4 m straw tube. Therefore, straw signals are considered fast pulses. For the transmission of fast pulses by an ideal transmission line, important characteristics of transmission lines are the impedance Z_0 and propagation speed v_0:

$$Z_0 = \sqrt{\frac{L}{C}} \approx 320\Omega, \tag{4.3}$$

$$v_0 = \frac{1}{\sqrt{LC}} = c. \tag{4.4}$$

Due to the non-zero wire resistance of $R \approx 110\,\Omega$ m^{-1}, the transmission line impedance Z, the propagation speed v and attenuation length λ depend on the frequency ω:

$$Z = Z_0\sqrt{1 - i\frac{\omega_0}{\omega}}, \tag{4.5}$$

$$v = \frac{v_0}{Re\sqrt{1 - i\frac{\omega_0}{\omega}}}, \text{ and} \tag{4.6}$$

$$\lambda = -\frac{v_0}{\omega} \cdot \frac{1}{Im\sqrt{1 - i\frac{\omega_0}{\omega}}}. \tag{4.7}$$

Where the characteristic frequency ω_0 is given by:

$$\omega_0 = \frac{R}{L}, \ f_0 = \frac{\omega_0}{2\pi} \approx 16 \text{ MHz}. \tag{4.8}$$

Following from the above with $\omega \to \infty$: $Z \to Z_0$, $v \to c$ and $\lambda \to \frac{2Z_0}{R} \approx 6\,\mathrm{m}$. For a good match between the straw tube and the preamplifier, the straw tube impedance is of particular interest. The straw tube impedance versus frequency is plotted in Fig. 4.5. For convenience in practical applications, the frequency f is used in favour of ω.

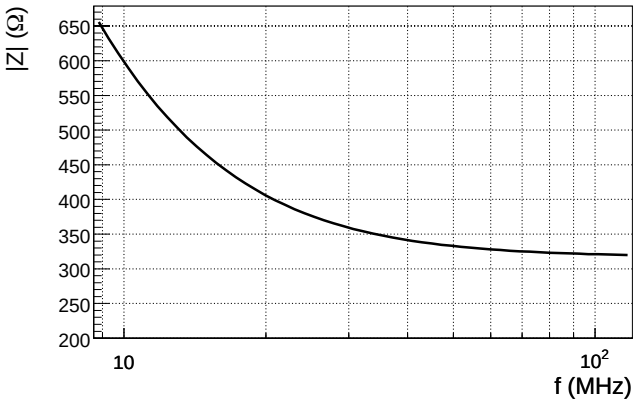

Figure 4.5: Characteristic impedance of a straw tube $|Z|$ as a function of frequency f.

The consequences of the straw tube transmission line characteristics described above are the following:

- To avoid reflected pulses travelling along the wire, the straw tube should be properly terminated. The impedances of the termination and the straw tube should be equal at the frequency of interest to eliminate reflections.
- Pulses travelling considerate length along the straw tube are attenuated. This lowers the detection efficiency for pulses generated far from the preamplifier side of the straw tubes.
- The frequency dependent transmission speed causes the leading edge of the pulse to smear, limiting the maximum resolution on the drift time measurement. Due to the relatively short length of the straw tubes, this effect is negligible.

From the straw tube properties for high-frequency signals, the requirements for the preamplifier follow. In Section 4.3, the preamplifier of choice and its performance is discussed.

4.2.3 Crosstalk

Due to the close spacing of the straw tube in a module monolayer, a straw response pulse affects the neighbouring channels through electromagnetic interference. This so-called crosstalk is suppressed by shielding, but cannot be completely eliminated.

For non-perfect conductors with a conductivity σ and a permeability μ, the penetration depth over which an incoming electromagnetic wave is attenuated with a factor e, the skin depth δ, is given by [70]:

$$\delta = \frac{1}{\sqrt{\pi f \mu \sigma}} \ . \tag{4.9}$$

Where the conductivity is $\sigma = \frac{1}{\rho}$, with ρ the conductor electrical resistivity.

The 12.5 μm outside aluminium layer of the straw tube acts as shielding. For aluminium, $\rho = 2.65 \mu\,\Omega$ cm, resulting in a skin depth of $\delta = \frac{0.082}{\sqrt{f}}$. The frequency dependence of the attenuation provided by the straw tube wall is plotted in Fig. 4.6. Because of its high resistance, the shielding effect of Kapton XC is negligible and is not taken into account. The typical range of interest is around 30 MHz, where the preamplifier is most sensitive. Sharp signal leading edges corresponding to frequencies in the GHz range are effectively suppressed by the straw tube walls.

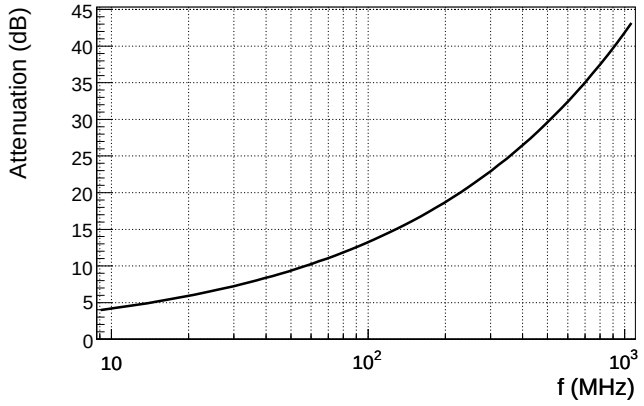

Figure 4.6: Attenuation provided by the aluminium in the straw tube wall versus frequency f.

It is outside the scope of this thesis to provide a theoretical calculation of straw tube crosstalk. Instead, the measured crosstalk between single neighbouring straw tubes is 1% at most [71]. Thus, for a signal of given amplitude, a signal is induced on neighbouring channels with 1% of the original signal amplitude. For nominal threshold levels and MIP straw tube signals, the probability that a channel hit is caused by crosstalk is about 5%.

In addition to the crosstalk from straw tubes, mutual influence of channels takes place in the front-end electronics boards and circuits as well. With a careful design it can be kept at a low level, but again it cannot be eliminated completely. Intrinsic crosstalk figures on the preamplifier are included in the next section.

4.3 Preamplifier and Straw Tube Interface

Originally developed as an application specific integrated circuit (ASIC) for the ATLAS TRT detector [58], the prime candidate for the preamplification of the LHCb OT straw tube signals is the ASDBLR [51, 72].

4.3.1 ASDBLR Description

ASDBLR is an abbreviation for Amplifier-Shaper-Discriminator with BaseLine Restoration. Its key design objectives are a high rate capability while maintaining a low noise level. High rate operation requires a fast recovery from signals, with effective elimination from slow ion tails. Therefore the ASDBLR contains base-line restoration circuitry for each channel. The output of the ASDBLR is a pulse of fixed height. The output pulses are read by a TDC measuring the timing of the leading edge. A block diagram of the chip internals is depicted in Fig. 4.7.

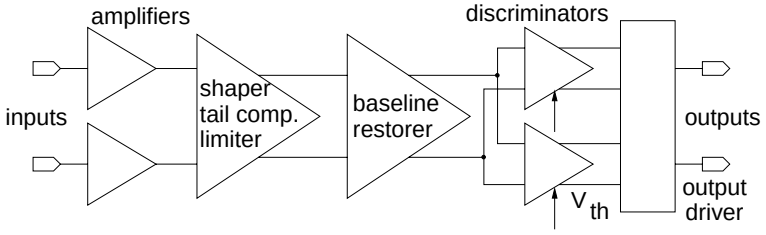

Figure 4.7: ASDBLR chip block schematic. For a single channel, two symmetrical preamplifiers are deployed, followed by a tail compensation, shaper, limiter and baseline restorer. Two discriminators are included, set by independent threshold voltages V_{th}. For the OTR, only the primary discriminator is used; the secondary is designed for a X-ray signal threshold to serve the ATLAS TRT detector.

The rate capability is extensively tested up to 20 MHz by the ATLAS TRT collaboration, exceeding the maximum rates expected in LHCb with an order of magnitude [73].

A single package features a 8 channel chip in a low-power design, requiring about 36 mW per channel. Channel-to-channel crosstalk is measured to be below 0.3% for chips mounted on a front-end electronics board [74]. This is low compared to the 1% intrinsic detector crosstalk caused by the straw tubes as discussed in the previous section.

In the case of a wire breakdown or a short-circuit, the energy stored in the channel capacitance is dumped into the input of the ASDBLR. The total stored energy in a capacitance C at voltage V is $U = V^2C$. For a 2.4 m long straw tube, the capacitance is 25 pF in addition to the 330 pF HV insulation capacitor. The total stored energy

accounts for 909μJ for V=1600 V anode voltage, making the incorporation of input protection circuitry into the ASDBLR design a necessity.

The chip is implemented in DMILL technology, which has been tested by the ATLAS TRT collaboration to be radiation hard up to at least 1.5 Mrad [75, 76], so it can easily be operated at the OT station edges.

4.3.2 ASDBLR Characteristics

The ASDBLR is optimised with respect to the signal over noise ratio and response speed. A fast response requires a large bandwidth B, which is proportional to the RMS of the noise voltage: $V_{Noise} \sim \sqrt{B}$. An optimal trade-off is reached when the input amplifier bandwidth is limited from 0 to 150 MHz. Following the preamplification and baseline restoration stages, the threshold comparator is designed with a 7 ns peaking time matching the preamplifier stage bandwidth.

The downside of the short peaking time are the increased noise and reduced efficiency. With a straw tube drift time up to 42 ns, at most 17% of the charge contained in the pulse generated by a MIP track in the drift cell is collected by the preamplifier with the current peaking time. For a MIP particle traversing a 4.9 mm straw tube, detected at the nominal gas gain of 7×10^4, the integrated charge accounts for about 67 fC.

To retain a high efficiency for the first cluster avalanche signal, it is necessary to operate the ASDBLR at a low threshold. The first cluster on average deposits a charge of 34 fC. With a threshold of 2 fC, 6% of the cluster charge, the timing of the first cluster leading edge is adequate and introduces an negligible error on the drift time.

Low-noise circuit design is applied to operate the chip at low threshold levels; the RMS of the intrinsic noise is specified at 2000 electrons (0.32 fC), which is in good agreement with measurements [77].

At the same time, single signal peaks of 20-50 times the threshold level will occur frequently due to absorption of X-rays or slow particles in the counting gas. A large dynamic range and fast return to baseline therefore is necessary to avoid a large deadtime trailing a large signal at the input.

Ion tail cancellation circuitry is built into the chip to reduce the deadtime. It is tuned to match the typical ion tails of Xenon and Argon based drift gases. The ion tail cancellation is linear up to charge deposits of 600 fC. Following the ion tail cancellation, a shaper with 25 ns signal width is incorporated. The signal at the shaper output is limited to 120 fC. To further reduce the response time of the preamplifier, baseline restoration (BLR) circuitry is incorporated in the chip design. The BLR allows the baseline and threshold levels to follow the low-frequency components in the amplifier signal. This eliminates the effects from signal pile-up, it reduces the sensitivity to a ion tail mismatch and it decouples the preamplifier and shaper from the comparator circuitry, thereby eliminating common-mode effects. The signal shapes after the ASDBLR stages are illustrated in Fig. 4.8.

As a result, the ASDBLR deadtime is very short. In the case of signals with a very large pulse height, the deadtime extends to a maximum of 160 ns [74]. With average signals, the deadtime varies between 20 and 40 ns.

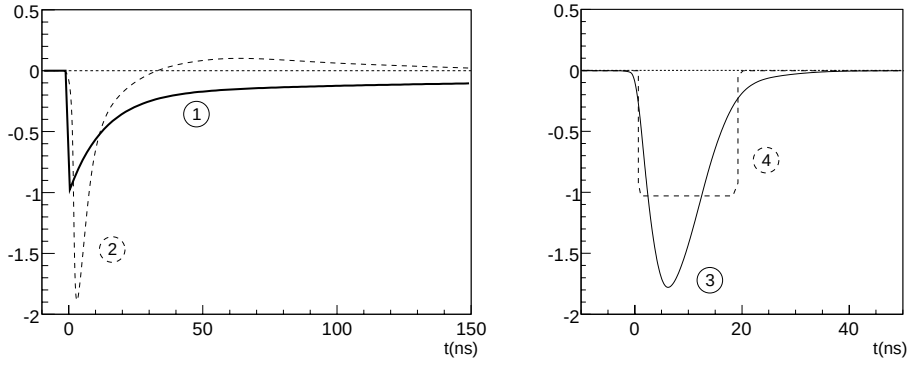

Figure 4.8: Illustration of the signal shapes versus time `t` in ns after the ASDBLR stages. In the left graph, the preamplifier (1) and shaper output (2) are drawn. In the right graph, (3) is the signal after the baseline restoration and curve (4) represents the discriminator output.

4.3.3 Straw Tube and ASDBLR Interface

When a pulse along the straw tube is generated, it initially splits in two equal parts. One part propagates towards the preamplifier and produces an output pulse. The other part propagates towards the module centre and reflects at the unterminated straw tube end, thereafter propagating towards the preamplifier end. For the 2.4 m long straw tubes, pulse transmission and straw tube termination characteristics are of prime importance.

The impedance of the straw tube should match with the input impedance of the ASDBLR for efficient charge collection and a proper termination of the straw tube. A non-perfect match of the preamplifier and straw tube impedances causes pulse remnants to reflect off the preamplifier end. These pulses can travel back and forth along the straw tube, generating additional pulses. If a pulse is generated near the preamplifier, the reflected pulse arrives ∼18 ns later. With the fast recovery characteristics of the ASDBLR, the reflected part of the pulse could well generate a second response ('afterpulsing').

From Eq. 4.7, it is seen that the impedance Z of the straw tube depends on the frequency f as $1/\sqrt{f}$. When constructing circuits using passive components only, the impedance functions can contain integer powers of f only. An impedance match is therefore only possible in a limited range. For straw tube signals, the frequency range of interest is centred around 30 MHz.

In Fig. 4.9, the measured input impedance as a function of frequency is plotted. To provide a proper impedance match between the straw tube and the ASDBLR at f=30 MHz, a series resistor is placed at the channel input. This resistor has to be as small as possible since it attenuates the straw tube signal and introduces additional noise at the preamplifier input. Measurements in the lab and beam tests showed that a

130 Ω resistor yields the optimal result: the resistance is small while large pulses do not introduce additional hits due to possible reflections [78].

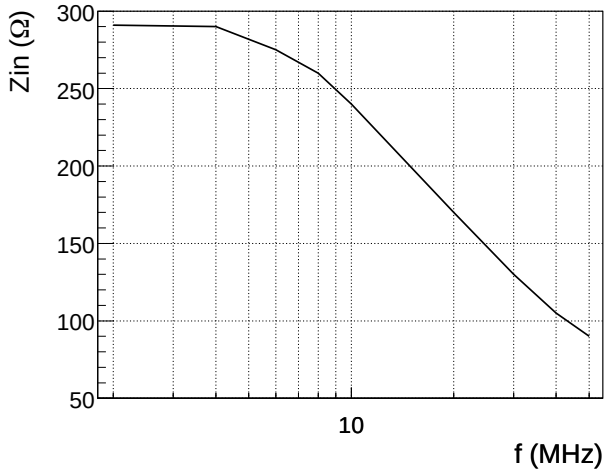

Figure 4.9: Input impedance Z_{in} of the ASDBLR as a function of frequency f.

Apart from the additional series resistance, care should be taken not to introduce additional capacitances at the ASDBLR input. In a realistic setup, multiple connectors and boards provide the necessary connections to the chamber and HV, acting as capacitors. Care should be taken that these capacitances do not cause an impedance mismatch resulting in additional reflections coming off this end of the straw tube. Additional uncontrolled capacitances raise the probability for reflections inducing undesired spurious pulses. Additionally, parasitic capacitances affect the intrinsic noise levels of the front-end electronics [77].

4.3.4 Physics Consequences

Ultimately, the OT performance is determined by the characteristics of the ensemble of straw tube and ASDBLR preamplifier. Multiple layers of full-length modules equipped with electronics resembling final versions were tested using radioactive sources and cosmic rays [79].

In Fig. 4.10, the noise rate is plotted versus the ASDBLR threshold for four different monolayers in the test setup. With the table in the left part of the figure, threshold voltage can be converted to threshold charge. To keep the amount of noise induced responses at a low level, the threshold needs to be raised above the nominal 2 fC level. A higher threshold reduces the resolution. Fig. 4.11 contains plots of the ASDBLR hit detection efficiency and track resolution as a function of the threshold voltage.

V_{th} (mV)	Q (fC)
600	2.0
700	2.8
800	3.6
900	5.4

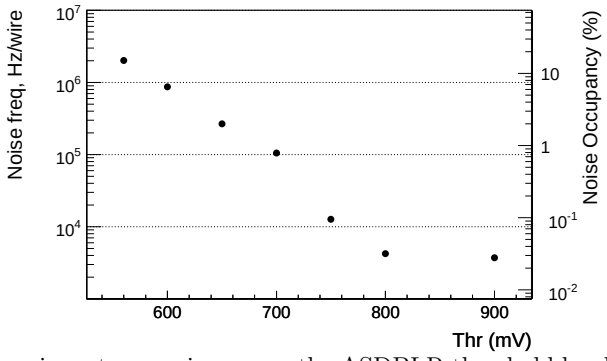

Figure 4.10: Plot of the noise rate per wire versus the ASDBLR threshold level (Thr). On the left y-axis, the noise rate expressed in the channel occupancy in %.

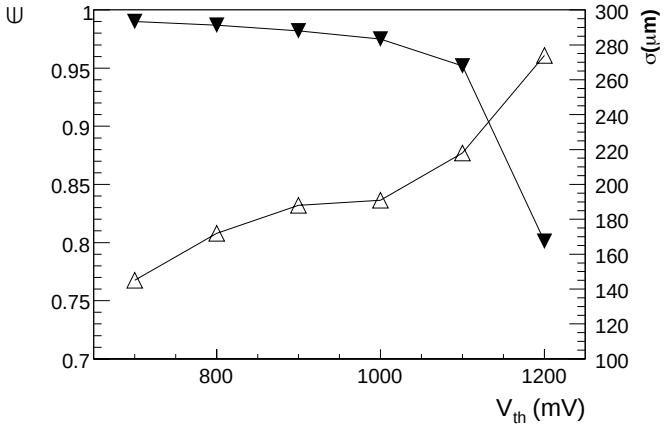

Figure 4.11: ASDBLR hit detection efficiency ϵ and track resolution σ as a function of threshold voltage V_{th}, indicated with filled and open markers, respectively. The values are averaged over a OT module monolayer [54]. The table in Fig. 4.10 converts the threshold voltage to charge.

During transmission, pulses are attenuated. As a consequence, the straw tube efficiency decreases with distance to the preamplifier. By leaving the opposite straw tube end unterminated, reflected pulses arrive within the shaping time interval, boosting the integrated pulse charge hence the detection efficiency. A plot of the charge collection efficiency of the ASDBLR preamplifier as a function of the distance along the straw tube wire is plotted in Fig. 4.12. The charge collection efficiency reflects the fraction of

the charge in a pulse which is accumulated by the preamplifier in its peaking time. The ASDBLR peaking time covers 17% of the signal collection time. In addition, the charge pulse is split in two equal parts travelling in opposite directions along the wire, hence the nominal charge collected within the peaking time should be about 8%, which is in agreement with the measurements. It is clearly seen that the charge collection efficiency does not decrease when the distance to the preamplifier increases, illustrating the boost of the unterminated straw tube end.

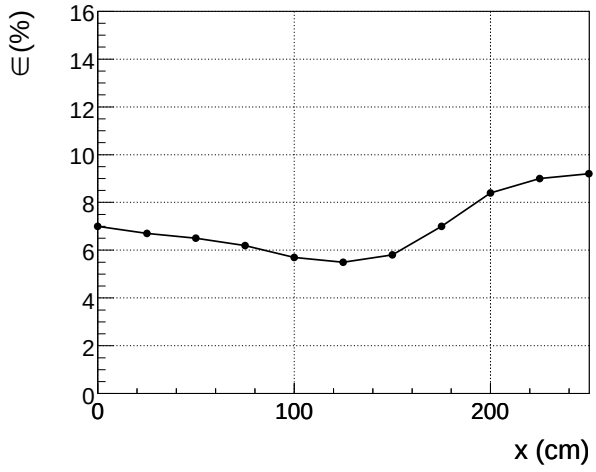

Figure 4.12: Charge collection efficiency ϵ in % of the straw tube relative to the distance x from the preamplifier.

The result from the current straw tube and preamplifier configuration is summarised as follows:

- By matching the impedance of the ASDBLR to the straw tube transmission line impedance, a proper termination is provided and reflections of pulses are suppressed. The other end of the straw tube is left unterminated. For signals originating far from the preamplifier, the reflected pulse adds to the direct pulse, compensating for signal attenuation along the straw tube. Some reflections are unavoidable; in some cases these generate a secondary response from the preamplifier.

- Crosstalk for straw tubes is at the 1% level; crosstalk in the electronics is about 0.3%. For a reasonable threshold value of around 3 fC and the intrinsic noise figures of the ASDBLR, this results in a 5% probability to have a hit induced by the crosstalk signals. This crosstalk figure is low and does not worsen the track reconstruction [44].

- The ASDBLR has a low intrinsic noise, of $\sigma = 0.32\,\text{fC}$. However due to parasitic capacitances at the input, the noise level is increased, necessitating a threshold setting above the desired 2 fC level, reducing the detection efficiency and accuracy.

- Due to the short shaping time of the ASDBLR, the deadtime is limited to 20-40 ns, depending on the pulse height. The peaking time of 7 ns is short and results in a good time resolution. However, measurements indicate that at most 10% of the total straw tube pulse charge is collected within this time interval, resulting in a lowered hit detection efficiency.

The hit efficiency and precision can be restored with increasing the gas gain by raising the anode voltage. However, an increased gas gain accelerates ageing processes, see Section 3.4.

4.4 TDC

For the timing of the ASDBLR output signals, a Time to Digit Converter (TDC) is required. To comply with the detector requirements and the specifications of the LHCb front-end electronics, a custom TDC, the OTIS [80] (Outer Tracker Time Information System) is developed.

4.4.1 Description of the OTIS TDC

The OTIS is intended to reside on-detector to avoid extensive cabling and possible deterioration of preamplifier output signals. The L0 buffering, logic and L0 derandomisers are included in the ASIC, greatly reducing the amount of data which has to be shipped off-detector. To withstand the radiation levels at the OT detector edges, the chip is implemented in 0.25 μm CMOS technology using radiation hard design techniques, it is tested for radiation hardness exceeding 1 Mrad [81].

With its 32 channel inputs, the OTIS is able to read signals off 4 ASDBLR chips, covering half a monolayer of an OT module. The large channel count reduces the data volume at the OTIS output and reduces the overall electronics cost.

As a clock signal, the 40 MHz LHC bunch-crossing frequency is used. Since the ASDBLR has a high sensitivity in this frequency range, care should be taken that the clock signals do not cause ASDBLR responses. By using low-level balanced signals for the OTIS connections, the influence to the analog front-end is minimised.

The OTIS architecture is depicted in Fig. 4.13. At the inputs, level comparators receive the hit signals from the ASDBLR chips. Next is a programmable channel mask register to block channels from entering the data stream (hot or noisy channels).

The actual time measurement of the OTIS is performed by means of a Delay Locked Loop (DLL). It consist of a series of inverters combined with a charge pump. The DLL is synchronised to the external clock, the state of the inverters determines the fine time steps within a 25 ns clock cycle. Upon a hit signal, the state of the DLL is copied to the corresponding Hit Register (HR). The 64 bit HR content is translated to a 6 bit

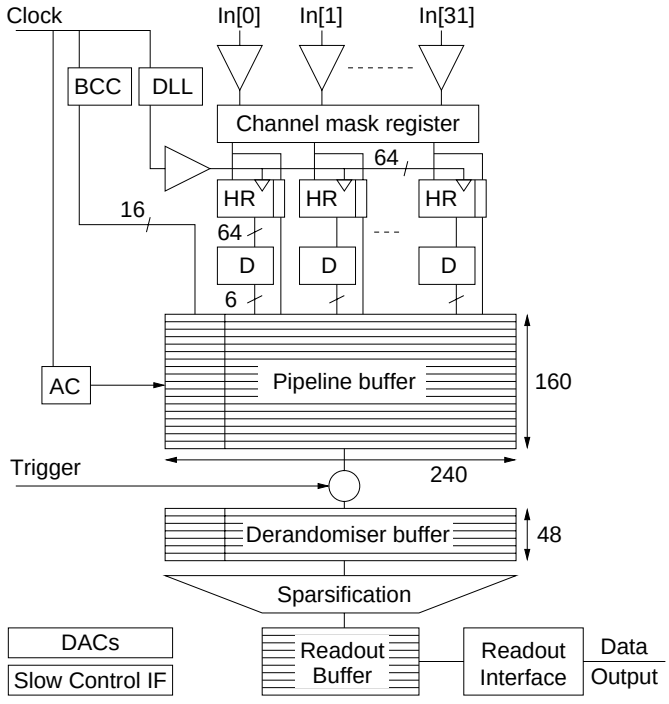

Figure 4.13: Architecture of the OTIS TDC.

time word by the Decoders (D) and is written in the pipeline buffer. In the pipeline buffer, 7 bits are allocated for every channel. It is 160 stages deep and covers the L0 trigger latency of 4 μs. The bunch counter (BCC) value is written into the buffer as well, to check the buffer synchronisation. Upon a L0 trigger, the corresponding hits and the BCC value are copied to the derandomiser buffer. This buffer has 48 stages and is required to store up to 16 events, allowing a maximum of 3 hits to be transferred upon a single trigger signal. Transferring multiple hits for a single channel in a single event is only possible with a low channel occupancy or reduced trigger rate. Following from the L0 specifications summarised in Table 2.6, the OTIS can only output 1 hit per channel per triggered event due to bandwidth limitations at nominal LHCb operation [68].

The sparsified event data are stored in a readout buffer before the data is transferred off the chip through the read-out interface. The OTIS delivers the data through a 8 bit wide bus.

An additional feature of the OTIS are 4 independent DACs, which provide threshold levels to the ASDBLR chips. The OTIS settings and DAC levels are programmable through an external I^2C slow control interface.

4.4.2 OTIS Performance

The TDC must not limit the detector resolution. With a 2.45 mm drift cell radius and a 200 μm resolution requirement, at least 48 time bins are required within the maximum drift time. To accommodate for fast drift gases and avoid TDC discretisation errors to contribute to the track resolution, the OTIS has a resolution of 6 bit within a 25 ns clock cycle, resulting in a time bin width of 0.39 ns. Fig. 4.14 contains a plot of the differential non-linearity of the time bins for four different temperatures [80]. From the plot it is seen that even and odd bins have a different offset sign. If this is compensated for, the RMS of the DNL is below 0.25 bin for the full temperature range.

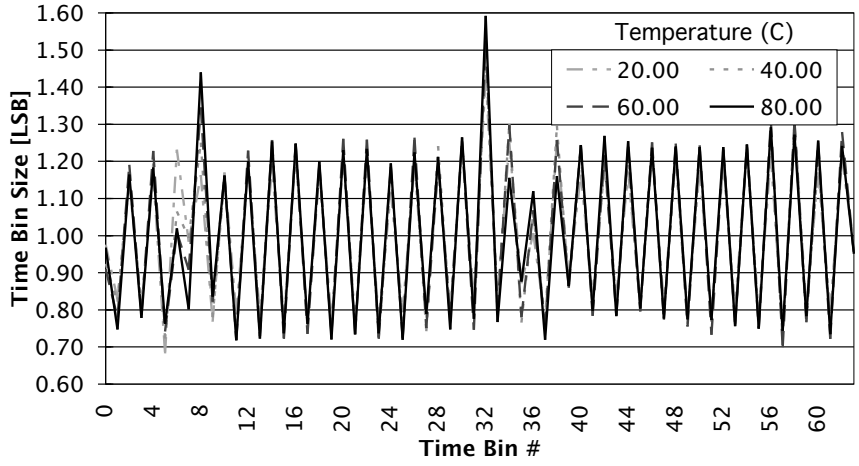

Figure 4.14: Differential non-linearity for the 64 time bins of the OTIS, plotted for temperatures of 20, 40, 60 and 80 ° C [82].

Digitised hits at the OTIS inputs are stored in the HR. This register is read out once in a clock cycle, therefore it is not possible to digitise and store multiple hits within a single clock cycle. As soon as a hit is digitised, the OTIS input is not responsive to hits in the remainder of the cycle, introducing a deadtime of at most 25 ns. This is hardly limiting the OT performance, since the ASDBLR preamplifier has an intrinsic deadtime of at least 20 ns.

Since the straw tube response time extends to multiple bunch crossing intervals, the capability to sample multiple hits for a single channel is included in the OTIS [80]. With the specified data- and trigger rates, only a single hit is read out in the 75 ns detector sample window, introducing a 6% inefficiency [44]. Should there be a drift gas fast enough such that the readout window can be reduced to 50 ns, the inefficiency is reduced to 5%.

4.5 L0 Readout and Data Transport

The essential functions of the L0 electronics as described in Section 2.10.1 are incorporated in the OTIS. The TDC contains the L0 hit buffer, trigger logic and deradomiser buffers. The output data needs to be shipped to the L1 electronics which reside off-detector.

The OTIS output bus delivers 8 bit wide words. A L0 event spans 36 words, hence the maximum event readout rate is 1.1 MHz, resulting in a data stream of 316.8 Mbits/s.

The electronics residing on-detector are exposed to a radiation dose up to several krad. When using radiation hard design techniques in .25 μm CMOS technology, effects such as 'latch-up', resulting in device failure, are avoided. Still, memory cells in integrated circuits can be influenced by radiation, ultimately resulting in the change of logical levels, known as 'bit-flips' [83]. Bit flips introduce errors in data but also alter configuration registers of front-end chips. To reduce the possibility of failing electronics or errors in data, the amount of memory and logical circuits must be limited. Instead of performing further data reduction or processing on-detector, data are shipped off-detector upon a L0 accept.

Following a development by the CMS collaboration, the data transport is performed by the Gigabit Optical Link (GOL) serialiser, operating at 1.6 Gbits/s rate [84]. The GOL accepts 32 bit wide words at 40 MHz rate, the data of 4 OTIS chips is transported by a single chip. The modular OT layout is conserved: all L0 accepted data of one module side is read out over a single serial (GOL) link. The GOL is coupled to an optical link driver, providing a galvanic insulation of the module electronics, eliminating noise due to mutual influence of neighbouring modules. Fig. 4.15 contains a schematic picture of the OTIS and GOL connections.

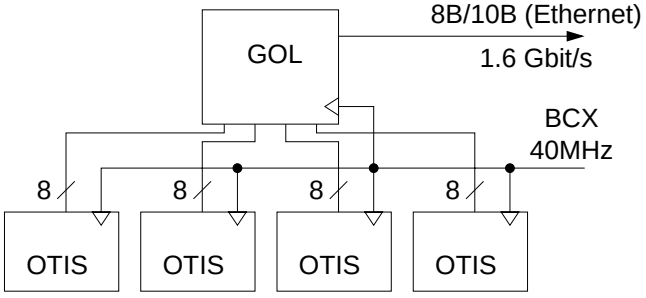

Figure 4.15: Block schematic of the OTIS and GOL connections. The GOL reads the OTIS data over a 8 bit wide bus. The data of 4 OTIS chips is transported over an optical link using the Gbit Ethernet protocol. All chips use the same 40 MHz BCX clock.

Since the GOL development is initiated by an LHC experiment, it is verified to

be radiation resistant and ensures virtually error-free transmission from L0 data to L1 electronics, even in radiative environments.

4.6 Off-Detector Electronics and Trigger Data Output

The L0 accepted data is received by TELL1 boards [85, 86], performing the tasks described in Section 2.10.1. A TELL1 board has 24 inputs for GOL links. Due to the high occupancy of the OT detector and the limited output bandwidth, only 9 inputs on every board are used. In total, the OT readout requires 48 TELL1 boards. The board reprocesses and outputs the data required for the subsequent trigger algorithms to the CPU farm.

To conserve bandwidth and processing power, the current proposal is to initially send a single bit representation for every channel. Channels which have registered a hit in the corresponding event are marked, omitting the timing information [87]. Sending binary hitmap information greatly reduces the amount of data shipped to the trigger processors: a single event of a TELL1 board accounts for 172 bytes. The data stream from the OT to the trigger processors accounts 172 bytes$\times$1.0 MHz $\times$48 boards = 8.3 Gbytes/s. The data rate is constant: it is not depending on the detector occupancy.

In the next section, an algorithm is presented for fast track reconstruction and momentum measurement for triggering purposes in LHCb. The algorithm uses binary hitmap data only, and is capable of track reconstruction and momentum measurement with a few % precision. Despite the fact that the division of the trigger into a L1 and Higher Trigger Levels (HLT) has been abandoned, these trigger levels are still used to illustrate the algorithm performance.

Chapter 5

T-Tracking: an Online Tracking Algorithm

The readout system described in the previous chapter is capable of delivering tracker data of events accepted by the Level-0 (L0) trigger. In this chapter, a track finding algorithm for online purposes, baptised 'T-tracking', is presented. It is used for track reconstruction and provides a track momentum estimate with a few percent resolution. The algorithm specifications, applications and implementation are described, followed by tracking performance figures using tracks from the VELO and muon detectors. In the next chapter, the performance of trigger applications using the T-tracking is presented.

5.1 Online Momentum Measurement

As can be seen from the histograms in Fig. 5.1, tracks from particles originating from a B meson decay have a high p_T compared to other tracks in events containing a B decay. Trigger algorithms use momentum information to select events containing a B decay and reject background events. Efficient track reconstruction and a p_T estimate with a precision of 10% or better is beneficial for the trigger performance. Currently, the VELO and TT detectors are used to provide an initial track momentum estimate to the trigger, see Section 2.9.2.

Between the VELO and the main tracker, the greater part of the magnetic field is present, as shown in Fig. 2.7. Reconstructing tracks using the VELO and the T stations therefore yields a more precise momentum estimate than achieved by the VELO-TT tracking.

Since the bandwidth available for the readout of T stations at trigger level is limited, an online tracking algorithm cannot access all tracker data. In this thesis, it is assumed that only binary channel hit data (hit maps) are transferred.

Using (binary) hit information from the T stations, multiple methods exist to obtain an estimate on track momentum, explained in the following paragraphs.

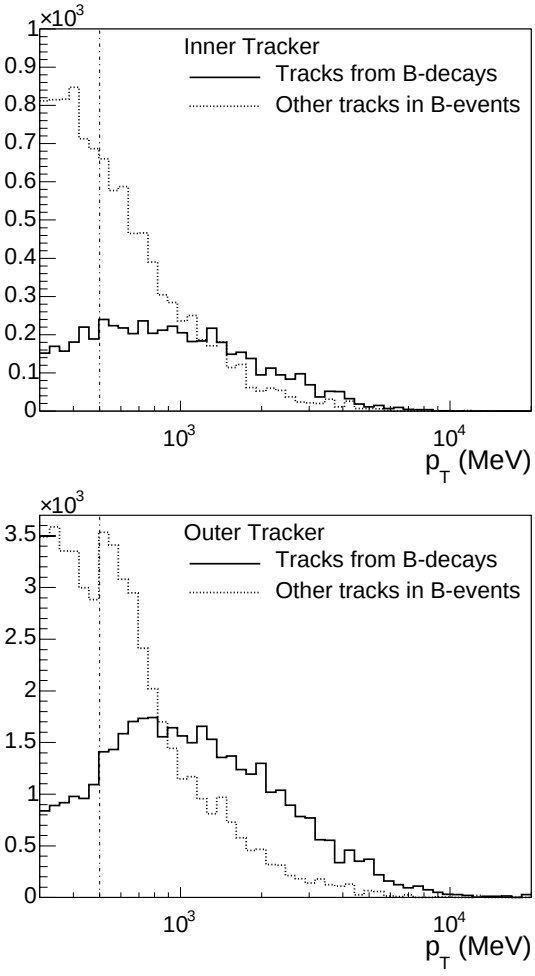

Figure 5.1: Transverse momentum (p_T) distribution of particles in the IT (top plot) and the OT (bottom plot) for tracks from B decays and other tracks. The vertical line indicates a value of 500 MeV p_T.

The 'P_T-kick' Method

The first method estimates the momentum p from the slope in the x-z plane of the track segments reconstructed in the T stations. It assumes tracks to originate from the nominal interaction point $(0, 0, 0)$. As is illustrated in Fig. 5.2, track segments are extrapolated to the $z = 0$ plane, where the distance to the origin x_0 is proportional to $1/p$ (see Eq. (5.1) in Section 5.2.3). Using the p_T-kick method, a momentum resolution

better than 9% is obtained.

VELO-T Matching

The track deflection, and thus the momentum estimate, is improved when a track segment in the T stations is linked to its corresponding track segment in the VELO. Due to the orientation of the magnetic dipole field, tracks are not deflected in the y-z plane. As a result, matching of track segments in the T stations to VELO tracks in the y-z plane is relatively straightforward and it is used to improve the matching efficiency and reject false track combinations.

The two track segments are assumed straight. Their extrapolations intersect at $z = z_f$, the magnet 'focal plane'. This is illustrated in Fig. 5.2, more details are found in Section 5.5.1. Using Eq. (3.2), the momentum is estimated from the slopes of the two track segments, resulting in a resolution better than 3%.

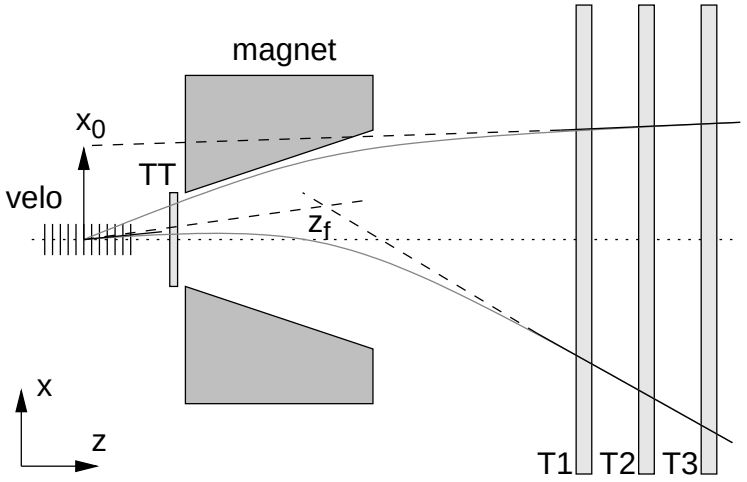

Figure 5.2: Schematic picture of the tracker detectors in the x-z plane. For the upper track, the momentum is estimated with the p_T-kick method, for the lower track, the momentum is determined using VELO-T matching, see text.

Track Fitting

The best momentum estimate is obtained when all measurements from the VELO, TT and T stations are used to follow a particle trajectory through the detector and finally fit a three-dimensional track to the measurements [44]. This method is more complicated than the previous two: high resolution measurement data from the sub-detectors are

required, as well as an accurate description of the magnetic field shape and its strength, and detailed knowledge of the material traversed by the particle. By an iterative track fit to the measurements, the accuracy of the momentum estimate is typically 0.5% for a large momentum range. However, the large volumes of data involved and the required processing power make this method unsuitable for online use.

An algorithm for online usage must have a limited execution time. The Level-1 (L1) trigger performance benefits from accurate momentum information on selected tracks, but has an average latency of 1 ms only. In the High Level Trigger, the first step is a L1 confirmation which consumes 4 ms on average. For both cases, the time budgets are small, calling for simple algorithms which only reconstruct a limited number of tracks and act on small amounts of data.

5.2 T-Tracking Applications

The T-tracking algorithm is developed for trigger applications and therefore focuses on reconstruction of the tracks with highest p_T. To find these tracks within the trigger execution time, continuations of reconstructed track segments in the VELO and muon detectors are looked for. This simplifies the algorithm and greatly reduces combinatorics and hence execution time. The track segments from the VELO or muon detectors are extrapolated. The resulting three dimensional position is called a 'seed point' and is used as a starting point for a track search in the T stations. In the following sections, the various cases of seed point generation are briefly discussed. Fig. 5.3 contains an illustration of the various algorithm applications.

5.2.1 VELO Track Seeding

The reconstruction of VELO tracks for L0 accepted events is described in Section 2.9.2. The L1 trigger decision is based on a small subset of the tracks in the VELO. Tracks with an impact parameter between 0.15 mm and 3.0 mm, and tracks linked to a L0 muon track are selected. On average, 8 tracks are reconstructed. Each of these L1-VELO tracks is used to generate a seed point for the tracking algorithm.

Other selections of VELO tracks could also be used for the generation of track seeds, for online and offline use such as alignment.

Between the VELO detector and T stations, charged particles will follow curved trajectories due to the magnetic field. Therefore, the VELO tracks must be properly extrapolated into the region containing the magnetic field to generate seeds for searches of straight track segments in the T stations. In section 5.5.1, details of the seed point generation from VELO tracks are discussed.

5.2.2 Muon Track Seeding

In addition to tracks reconstructed in the VELO, muon detector tracks can be used to generate seed points. For the L0 trigger, the muon detectors provide tracks consisting of a three dimensional point and slopes in the x-z and y-z planes (x, y, z, t_x, t_y).

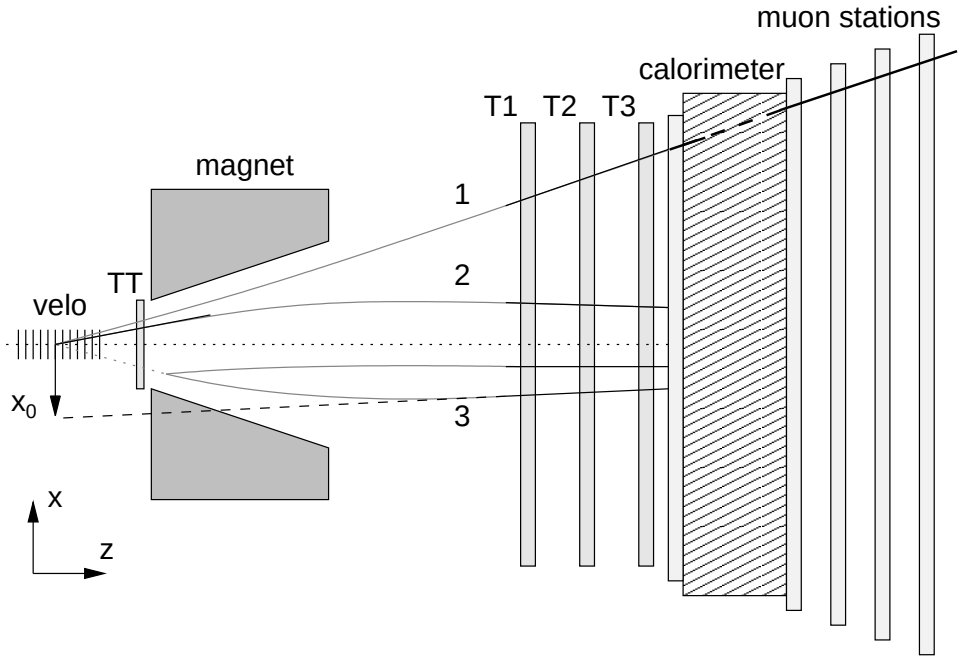

Figure 5.3: Schematic display of three applications of the tracking algorithm. Seed points are generated from:
1. Tracks from the muon detectors.
2. Extrapolated VELO tracks.
3. Stand-alone generated points at (x_0,0,0).

Between the muon detector and the T stations, there is no magnetic field to deflect the tracks. Still, a particle trajectory is not necessarily straight since it can suffer large deflections due to multiple scattering in the calorimeter material.

More details on the seed point generation using the muon stations are found in Section 5.5.2. The algorithm for online muon reconstruction is described in 5.7.

5.2.3 Stand-Alone Seeding

Instead of using tracks from external subdetectors, a mesh of points could serve as starting points for a track search.

An array of space points $(x_0, 0, 0)$ is generated for several values of x_0, each acting as a separate seed point. If a track is found, its momentum p is directly estimated using

the p_T kick method:

$$\frac{p}{p_{T\,kick}} = \frac{z_f}{x_0}, \tag{5.1}$$

where $p_{T\ kick}$ is the integrated magnetic field, accounting 1.2 GeV, and z_f is the z position of the magnetic focal plane at 5200 mm.

A track search using stand-alone seeding is very versatile and could be used to verify detector alignment or search for tracks which are produced from a particle which has decayed in flight (e.g. a K_S^0) as illustrated in Fig. 5.3. It is less suited for an online application to search for continuation of tracks found in the VELO or muon detectors due to the large combinatorics and resulting large algorithm execution time. For this reason, the stand-alone seeding method is not discussed further in the following chapters.

5.3 Tracking Algorithm Requirements

Efficiency and ghost rate are the performance criteria for tracking algorithms. The efficiency is defined as the fraction of correctly reconstructed tracks N_{rec} from a total sample of tracks S, containing N_{tot} tracks. The tracks in the sample must satisfy certain conditions; obviously it is impossible to reconstruct tracks outside the detector acceptance. Therefore the efficiency ϵ is defined as:

$$\epsilon = \frac{\mathcal{R}(S)}{S} = \frac{N_{rec}}{N_{tot}}, \tag{5.2}$$

where $\mathcal{R}$ represents the reconstruction algorithm, acting on S.

During track reconstruction, uncorrelated detector responses accidentally aligned along a possible particle trajectory can be recognised as a track. These tracks, which are not associated to any particle, are called ghost tracks or ghosts. The fraction of ghosts in the total sample of reconstructed tracks is the ghost rate. In general, the track finding efficiency is correlated to the ghost rate: an optimal working point has to be found.

As can be seen from Fig. 5.1, the majority of tracks with a p_T below 500 MeV is not originating from a B decay. Therefore, T-tracking is less suited for the reconstruction of tracks with p_T <500 MeV. However, for higher p_T values the algorithm should be efficient and have a low ghost rate.

Ideally, a tracking algorithm for triggering purposes should comply with the following requirements:

- The algorithm must have a high efficiency for tracks with p_T over 500 MeV.
- The ghost rate for tracks with a p_T exceeding 500 MeV must be low.
- The p_T resolution for reconstructed track segments must be better than 10% to enable an efficient L1 trigger (see Section 2.9.2).

- The execution time of the algorithm must be 1 ms on average for use in the L1 trigger and 4 ms if used for L1 confirmation in the HLT. For a low execution time, the amount of data processed by the algorithm must be limited.
- The algorithm should be robust: the performance must not collapse under slight variations of the algorithm parameters, and it must be tolerant to small detector misalignments.

The algorithm developed to fulfill these requirements is based on the so-called Hough Transform and is explained in the next section.

5.4 Hough Transform Based T-Tracking

5.4.1 Working Principles

Originally developed for analysis of bubble chamber images, the Hough Transform [88] is used to reconstruct patterns from data points. The patterns are described with a set of parameters; subsequently the measurements are characterised using these parameters. Measurements belonging to an instantiation of the supposed pattern will be closely spaced in the parameter space. Pattern recognition is performed by clustering the measurements in the parameter space.

In the T-tracking, the clustering algorithm is controlled by the minimal number of required data points in a cluster and their maximum parameter spread. Tracks are found by clustering a minimum number of measurements with closely spaced parameters.

5.4.2 Hough Transform for T-Tracking

The limited execution time budget restricts the algorithm complexity to a minimum. Therefore the Hough transform based algorithm will look for straight track segments in the T stations as the basic pattern. The parametrisation of a straight track segment is divided in two parts: the first part describes the track in the x-z plane, the second part characterises the track in the y-z plane.

The segments found in the two planes are not independent. The y coordinate is not directly measured, but is determined from measurements in the detector layers with $\pm 5^\circ$ stereo angles. As explained in Section 5.5.4, the track in the x-z plane is used to combine the track segments in two planes to a single track in three dimensions.

A track segment is parametrised by the slope t_x in the x-z plane, t_y in the y-z plane, and an offset point $(a, b, 0)$ as follows:

$$x = t_x z + a, \tag{5.3}$$

$$y = t_y z + b. \tag{5.4}$$

The segment is assumed to pass through the so-called seed point (x_0, y_0, z_0), consequently $a = x_0 - t_x z_0$ and $b = y_0 - t_y z_0$.

With the assumption of the track passing through the seed point, measurements are uniquely parametrised by their slopes t_x and t_y. In both the x-z and the y-z plane, clustering will group measurements which have the same slope parameter of an imaginary line connecting the measurement and the seed point. Fig. 5.4 contains an illustration of hit channels ('hits') with their parametrisation with respect to a seedpoint.

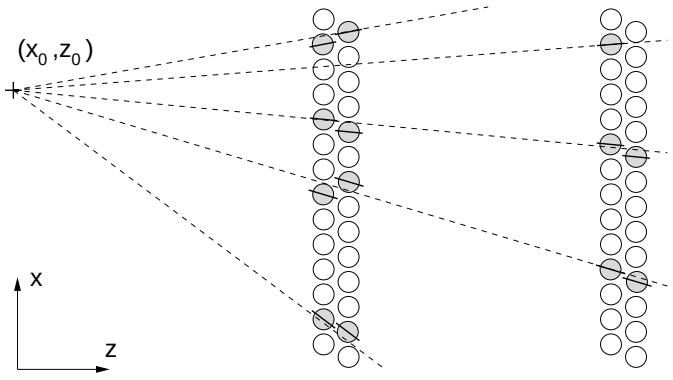

Figure 5.4: Schematic picture of a seedpoint (x_0, z_0) with detector layers. Hit channels are shaded, the dashed lines indicate straight tracks through the seed point and the measurements. The parametrised slope of the hit channels are drawn at the channel centre.

Due to the limited resolution, the slope parameters of measurement along a perfectly straight line are not equal but will have a small spread. The task of the clustering algorithm is to group measurements with parameters which are closely spaced without adding measurements which do not belong to the track.

The modelling of particle trajectories by straight tracks is sufficiently accurate if the detector resolution is limited. Particle tracks are curved between stations T1 and T3 due to the stray field from the magnet. If the deflection is equal or less than the detector resolution, particle trajectories are approximated with straight tracks.

Due to readout bandwidth limitations, only binary channel hit information of L0 accepted events is available. This limits the detector resolution to the physical channel size: 4.9 mm for the OT and 198 μm for the IT detectors.

In Fig. 5.5, a track with a sagitta s over the distance Δz between T1 and T3 is illustrated. With a sagitta below the width of a single channel, the track will be reconstructed as a straight line, albeit with a slightly different slope at T1 and T3.

For relativistic particles at speed $v \simeq c$, with charge e and a mass m boosted with Lorentz factor γ, the radius of curvature R in a magnetic field B is:

$$R = \frac{\gamma m v}{eB} = \frac{p}{eBc}. \tag{5.5}$$

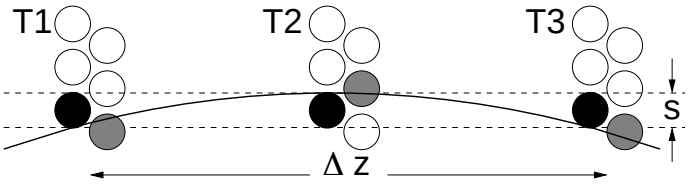

Figure 5.5: Sketch of a deflected track (solid line) which is reconstructed as a straight line in the region of the tracker stations. The maximum sagitta s over the distance Δz between T1 and T3 equals the channel pitch. Channels which are hit by the particle are shaded: hit channels compatible with both the curved and a straight track are filled.

With the above equation, the minimum momentum of tracks which are reconstructed as straight segments is calculated. Between T1 and T3, an integrated magnetic field of $\int B\,\mathrm{d}l \approx 0.26$ Tm is present. For a circular particle trajectory over the 1.6 m distance between T1 and T3 with a sagitta of the OT channel pitch of 5.25 mm, R is 64 m. Inserting 0.16 T for B and 1 for the charge e into Eq. (5.5), the resulting momentum p for this track accounts 3 GeV/c. Tracks with lower momentum cannot be considered straight in the OT when using binary hit information.

From the momentum distribution of tracks traversing the OT as plotted in Fig. 5.6, it can be seen that only a small fraction of tracks originating from a B decay have a momentum below 3 GeV. To reconstruct only straight track segments is therefore not leading to a large inefficiency.

Given the small IT channel size, only hits of particle tracks with $p >$80 GeV have a deflection small enough to be considered to resemble a straight line within the detector resolution. From the momentum distribution of the tracks passing through the IT detector, plotted in Fig. 5.6 it is clear that only a small fraction of the tracks appears straight. In the IT, the clustering algorithm must accommodate for tracks which are not perfectly straight. In the next section, implementation details of the T-tracking are presented.

5.5 T-Tracking Implementation

The T-tracking algorithm, based on the Hough Transform, is implemented in C++ code running within the Gaudi software framework [89]. It is implemented as a tool inside the DaVinci environment, version v12r13 [90]. It makes use of the simulated detector response data, generated with the Brunel program version v23r7 [91], for the Data Challenge 2004 (DC04) project.

LHCb will be operational from 2007 onward, consequently the algorithm performance

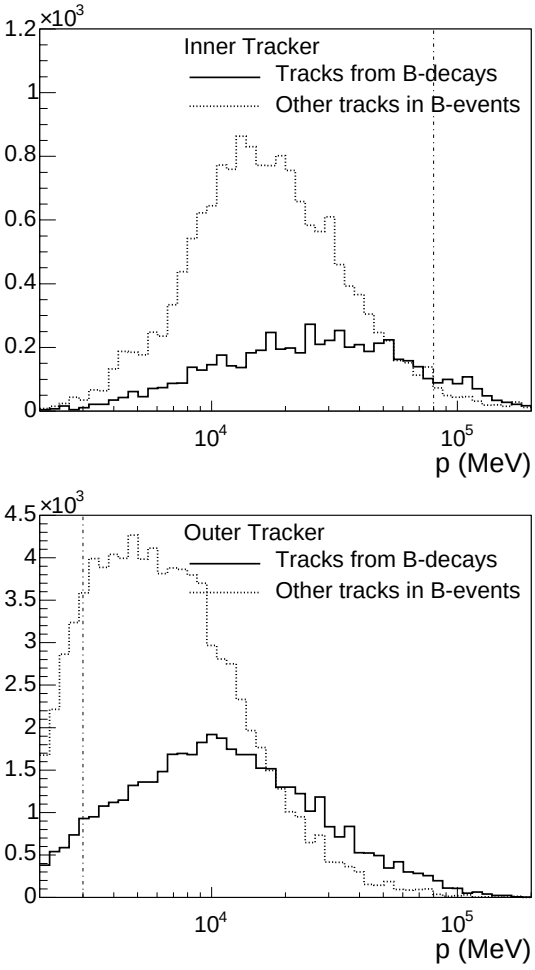

Figure 5.6: Momentum (p) distribution of particles in the IT (top plot) and the OT (bottom plot) for tracks from B decays and other tracks. The vertical line indicates a p of 80 GeV for the IT, and 3 GeV for the OT.

is entirely based on simulation studies using Monte Carlo (MC) techniques. An advantage is that all simulation information is traced back through all steps of the simulation: every detector response is attributed to the original particle inducing it, allowing the measurement of efficiency and ghost rate of tracking algorithms.

The detector response available in the GAUDI framework is generated by several external simulation programs: the PYTHIA program [40] generates events from a pp collision, the EVTGEN program [92] simulates the B-hadron decays. Both programs are

steered by a GAUDI application named GAUSS [93].

Subsequently, the GEANT4 package [89] is used to simulate the propagation of particles through the detector. It is also controlled by GAUSS. The response of the hit detector channels and the simulation of the readout electronics is performed by the digitisation application, BOOLE [94].

5.5.1 Seed Point Generation From VELO Tracks

The first step of the T-tracking is the generation of seed points (x_0, y_0, z_0). The track segments are supposed to pass through these points, therefore the choice and precision of the seed points is crucial to find the correct track. To generate useful seed points for the determination of the tracking algorithm performance, tracks found by the VELO are extrapolated into the magnet.

The magnetic field is modelled according to the sketch in 3.2. It is approximated by a singular field of equal strength $\int B \, \mathrm{d}l$, located at $z = z_f$, the magnet focal plane. In this model, track deflection is instantaneous and takes place at z_f.

Due to the non-homogeneity of the magnetic field, the focal plane is not perfectly flat. By determination of the intersection points of straight extrapolations of particle tracks in the VELO and tracker detectors, the focal plane is reconstructed and subsequently parametrised. For the determination of its shape, tracks with $p > 3\,\mathrm{GeV}$ traversing all three tracker stations are used. The top graph of Fig. 5.7 contains a scatter plot of the reconstructed z_f versus the track slope at the VELO detector. From the scatter plot, a profile histogram of the average positions is extracted and this histogram is fitted with a parabolic function, displayed in the bottom half of Fig. 5.7. The fit results are used for the seed point generation: VELO tracks are linearly extrapolated towards the point (x, y, z_f). In the y-z particles are expected to follow straight trajectories in absence of a magnetic field. As expected, no specific structure emerged from a focal plane analysis as described above. Consequently, tracks are extrapolated linearly towards the z_f coordinate extracted from their slope in the x-z plane.

5.5.2 Seed Point Generation From Muon Tracks

Tracks in the muon detector are reconstructed by a dedicated algorithm [95], combining hit channels in the M5 station upstream with hits in M4, M3, and M2 subsequently [36]. M1 is omitted for occupancy reasons, which considerably worsens the momentum resolution from muon tracks, see Section 5.7.

Between the T1 station and the muon detector, a stray field from the dipole magnet is present, deflecting the particles in the x-z plane. In the y-z plane, tracks are supposed to follow straight trajectories.

However, multiple scattering in the material of the calorimeter contributes significantly to the particle deflection between the T stations and the muon stations in both the x-z and y-z planes. Furthermore, a consequence of using binary channel information on the detector layers under $\pm 5^\circ$ stereo angles is that the accuracy of individual

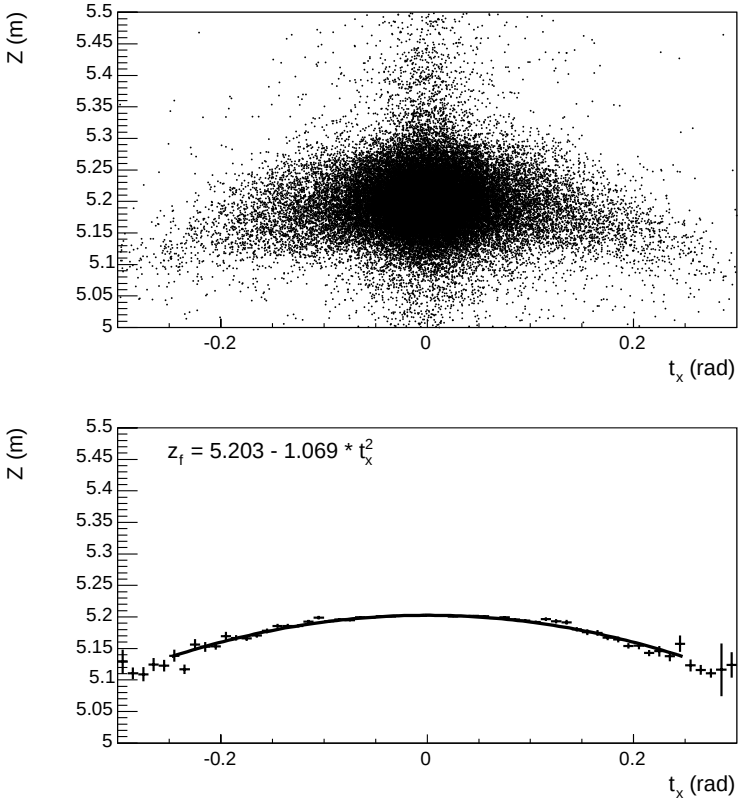

Figure 5.7: The above graph contains a scatter plot of the intersection points (Z) of straight track segments in the VELO and tracker detectors versus the track slope in the VELO, t_x. In the bottom graph, the extracted average profile is fitted with a parabolic function, plotted with a solid line.

measurements in the y-z plane accounts 60 mm, introducing additional errors on the particle slope.

A similar procedure for the determination of the magnet focal plane shape described in the previous paragraph confirmed the assumption that the scattering for muon tracks takes place halfway the calorimeter, at $z = 13.9\,\mathrm{m}$ on average. The 'focal plane' is assumed flat, since the analysis revealed no specific shape in the z direction as a function of the track slope.

Consequently, muon tracks found in M2-M5 are linearly extrapolated to $z = 13.9\,\mathrm{m}$, where a seed point is constructed. Apart from the seed point position, the slopes of the muon track are used to define a window in the T stations. For enhanced track finding

efficiency and a reduction of algorithm execution time, only hits inside the window are used in the track finding algorithm.

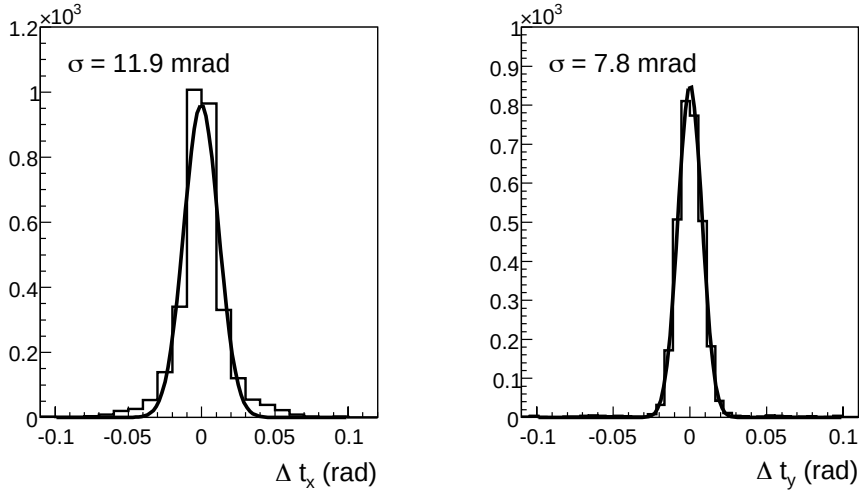

Figure 5.8: Histograms of the difference in particle track slopes $\Delta t_x, \Delta t_y$ in the T stations and the muon detector for the x-z and y-z planes, respectively. The σ is extracted from a Gaussian fit to the histograms.

The magnetic field, multiple scattering, and detector resolution introduce significant deviations from a reconstructed straight particle trajectory. To estimate the measured track deflection, the difference in reconstructed slopes of track segments in the T stations and the muon detector for MC particles is recorded. Separate histograms are recorded for the deflection in the x-z and y-z planes, both are fitted with a Gaussian curve, displayed in Fig. 5.8 . The σ of the curve is taken as the average deflection in the corresponding plane.

From the plots it can be seen that the match between the deflection distribution and the Gaussian fit is better in the y-z plane than in the x-z plane. This is supposed to originate from the magnetic field, enlarging the deflection in the x-z plane.

The deflection figures are used to reduce the track search execution time. The muon track is extrapolated through the T stations, tracks are sought only in regions where their slope differs less than 3σ from the original muon track slope.

5.5.3 Hit Selection and Track Search

After generation of the seed points, the x-layer hits in the tracker are parametrised in the x-z plane. Using Eq. (5.3) with a seed point (x_0, z_0), the t_x is calculated for every measurement (x, z) in the T stations.

To limit the execution time, only a selection of all detector hits is used for a track search. In the case of the muon seeded approach, a straightforward window is applied; in the case of the VELO seeded approach, the specific hit selection procedure is described below.

Since the B decay tracks generally have a momentum above 3 GeV, the tracking algorithm will look for high momentum tracks only. Using Eq. (5.5), the deflection of a 3 GeV track in the 4 Tm magnetic field does not exceed 0.25 rad between the VELO and the T stations. This limit, combined with the measured track slope upstream of the magnetic field in the VELO, provides a region where the track traverses the T stations. Measurements inside this region are parametrised for the track search.

In reality, tracks additionally suffer from multiple scattering which could increase the deflection. An additional margin is kept: hits are selected when their slope parameters t_x do not differ from the VELO track t_x more than 0.3 rad. Fig. 5.9 contains a histogram of track deflection in the x-z plane, generated for particles in events containing a B decay. Tracks with $p > 3$ GeV traversing three tracker stations are considered, the shaded area in the histogram represents tracks originating from a B decay. Only a very small fraction of B decay tracks are outside the plot range of ± 0.3 rad. As expected, the deflection corresponds to the track momentum: if only tracks with $p > 10$ GeV are considered, track deflection is limited to ± 0.2 rad.

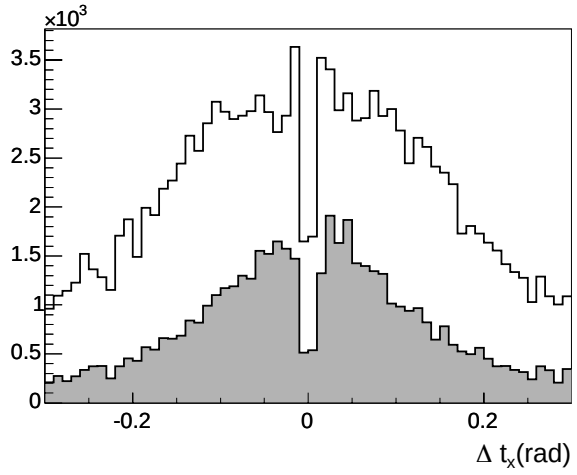

Figure 5.9: Reconstructed deflection in the x-z plane $\Delta t_x = t_{x,VELO} - t_{x,T}$ in the magnetic field for particles with $p > 3$ GeV. The shaded area represents particles originating from a B decay. The deficit around 0 reflects that few particles have a momentum high enough to undergo almost no deflection.

After parametrisation of the measurements in the selection window, the clustering on the t_x parameters is performed as follows:

- The measurements are sorted on their slope parameter.
- The clustering algorithm advances in one direction through the sorted measurements.
- Each measurement is considered a starting point for a cluster.
- A measurement is added to the cluster if its slope parameter differs by less than a value $d_{\min}$ from the parameter of the previous measurement.
- If the next measurement parameter differs more than $d_{\max}$ from the parameter of the starting point, the cluster formation stops.
- When the number of clustered measurements exceeds a threshold, the cluster is kept. Otherwise, it is discarded.
- If an upper limit on the number of measurements is exceeded by the addition of the next measurement, the cluster formation is stopped.

Since the algorithm steps through the sorted measurements in one way and considers each one of them as a starting point for a cluster, a single track will generate multiple clusters. These clusters will have practically identical parameters, mainly differing in the number of measurements. From such a sequence, the cluster containing the largest number of measurements is kept. A histogram of parametrised measurements with respect to a single seed point is plotted in Fig. 5.10.

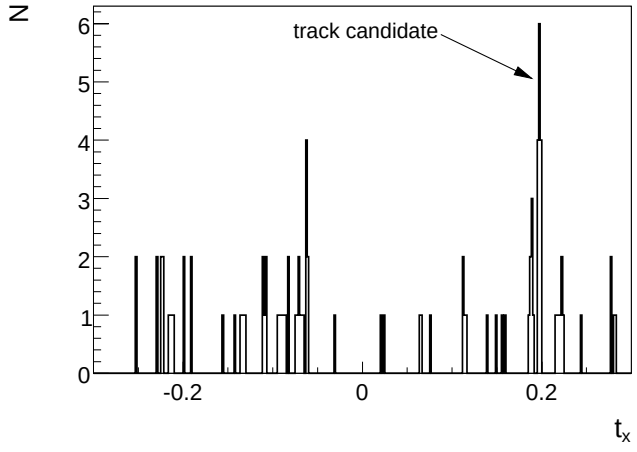

Figure 5.10: Histogram of parametrised tracker hits (t_x) with respect to a seed point. A track candidate cluster is indicated.

To limit the number of found clusters further, only clusters of which the average slope is more than 1.5 $d_{\max}$ apart are kept. This avoids the same track to be found multiple times in different clusters.

When searching for tracks, it must be possible to evaluate hits from the OT and IT detectors simultaneously. By assigning a weight to measurements for either detector, the fact that the OT has twice as many detector layers with respect to the IT is compensated for. The weight also takes into account the single channel efficiency differences between the OT and IT. An OT monolayer of straw tubes with inner diameter $d = 4.90\,\text{mm}$, with average efficiency $\epsilon = 0.97$ arranged at a pitch $p = 5.25\,\text{mm}$ has an average efficiency of $d\,\epsilon/p$=91%. For two staggered monolayers, the average number of clusters N_L becomes:

$$N_L = \frac{\epsilon(p-d) + (2d\,\epsilon)}{p}, \tag{5.6}$$

resulting in $N_L = 1.87$. The efficiency of an IT layer is above 99% [30]. Relative to an OT hit weight of 1, the weight of a single IT measurement is 1.9, equalling the weight of a double-layer OT response and a single IT response.

5.5.4 Stereo Confirmation of x-z Tracks

Tracks found in the bending plane are extended to a track in three dimensions by including hits from the layers placed under a $\pm 5^\circ$ stereo angle. For each track candidate in the x-z plane, corresponding stereo layer hits are searched for. Information in the vertical direction cannot be extracted directly, since the coordinate measured by the detector channels is the ordinate u. The ordinate is expressed in x and y as:

$$u = x\,\cos\,\theta_s + y\,\sin\,\theta_s, \tag{5.7}$$

where θ_s is the stereo angle, as is illustrated in Fig. 5.11. For layers with vertical orientation, θ_s=0, so that $u = x$. For a x-z track candidate, the stereo measurements are mapped to y-coordinates by inverting Eq. (5.7), such that the clustering algorithm is repeated in the y-z plane.

In the x-z plane, the resolution σ_u for binary readout of the OT equals the channel size of 5.25 mm. For measurements along the y-axis, the projected resolution σ_y becomes $\sigma_u/\sin\,\theta_s$, as illustrated in Fig. 5.12 As a result $\sigma_y = 11.5\,\sigma_u$. For the OT, σ_u=5.25 mm, and σ_y=60 mm. For the IT, σ_u=0.198 mm, and σ_y=2.28 mm.

Since the magnetic dipole field is oriented parallel to the y-axis, high momentum tracks are hardly deflected in the vertical direction. In Fig. 5.13, the difference in t_y of track segments in the VELO and the T stations is plotted for particles with a momentum over 3 GeV which traverse the tracker stations. In the histogram, the shaded region applies to particles originating from B decays. As can be seen from the histogram, the deflection of these particles is small, so it is safe to assume that particles with high momentum follow a straight trajectory and originate from the primary interaction point. In addition to the seed point, a prediction of t_y is used.

Similar to the hit selection for tracking in the x-z plane, the t_y prediction is used to reduce the number of candidate hits from the stereo layers, limiting combinatorics and

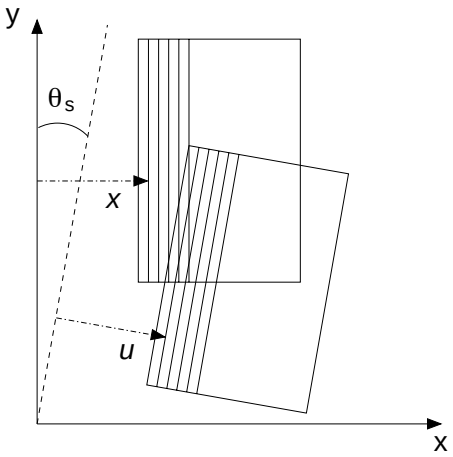

Figure 5.11:

The measured coordinate for detector layers is the ordinate u. For vertically oriented layers, the stereo angle θ_s is zero, and u=x.

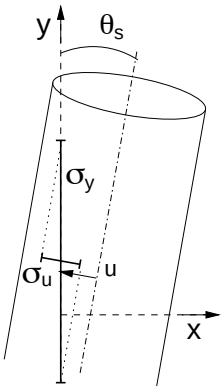

Figure 5.12:

Resolution σ_u of the measured ordinate u and the resulting resolution σ_y in the y direction for channels with a stereo angle θ_s and a given x coordinate.

algorithm execution time. A first selection based on the t_x of the track includes only the channels in the stereo layers which cross the track, irrespective of the y coordinate, limiting the number of stereo channels possibly contributing the track reconstruction in a monolayer to 50. A second selection takes only the measurements in a window of 60 mrad around the t_y from the VELO track into account, reducing the count of candidate channels in a single layer to about 8. The current algorithm implementation still calculates the parameters for all stereo hits and performs the selection afterwards: a considerate reduction of execution time is expected by improving the hit selection procedure.

The cluster selection algorithm acting on the selected measurements is identical to the track search in the x-z plane. However the values for $d_{\min}$, $d_{\max}$ and the minimum number of hits for the clustering algorithm are different, resulting from the limited resolution in the y direction.

Track segments that are not confirmed by track segments in the y-z plane are discarded. Because of the low resolution in the y direction, it occurs that multiple track segments in the y-z plane are found matching a single track segment in x-z. In that case, the x-z segment is copied and either y-z segment is added to the track. The final selection of the proper track is left to the next step in the track finding algorithm.

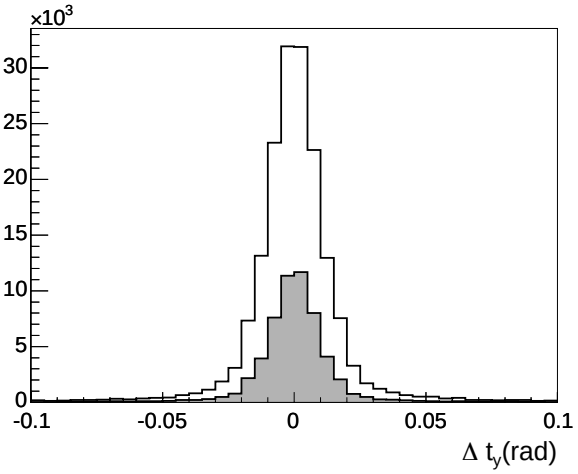

Figure 5.13: Reconstructed deflection in the y-z plane $\Delta t_y = t_{y,VELO} - t_{y,T}$ in the magnetic field for particles with p higher than 3 GeV. The shaded area represents particles originating from a B decay.

5.5.5 Track Selection

While striving for a high track finding efficiency, the algorithm frequently finds multiple tracks in the tracker matching a seedpoint from a single VELO track. Of these tracks, the best candidates must be selected.

The first step in the selection is to cut on the cluster parameters of the tracks. Tracks must have a summed hit weight over the values listed in Table 5.2, corresponding to a measurement in about 3 out of 4 detector layers. Clusters with summed hit weights exceeding 19, twice the minimum requirements, are discarded since they are likely composed of hits from two particle tracks. After the cut on the summed hit weight, the standard deviation σ and χ^2 are calculated, where χ^2 takes into account that measurements in stations far from the seed point z_0 have a higher slope resolution resulting from the large lever arm $z_n - z_0$:

$$\sigma = \frac{1}{N}\sum_{n=0}^{N}(t_{x_n} - \bar{t}_x)^2, \text{ and} \tag{5.8}$$

$$\chi^2 = \sum_{n=0}^{N}\left(\frac{(t_{x_n} - \bar{t}_x)}{(z_n - z_0)}\right)^2. \tag{5.9}$$

With measurements perfectly aligned along a straight line, the σ and χ^2 are small. By application of cuts on σ, χ^2, and on the cluster width divided by the number of hits, $d_T/\mathrm{N_H}$, defined in Eq. (5.10), tracks which might not be straight segments are removed

from the selection.

The following step is the removal of clone tracks: tracks which happened to be found twice. Clone tracks have almost identical parameters, sharing a large fraction of hits. To filter out clone tracks, the coordinates of the intersection points of the track segments in x-y planes at the T1 and T3 stations are calculated. If the tracks intersect these planes within 10(100) mm in $x(y)$ of each other, they are marked as clones and one of the two is discarded. The best of the two tracks is selected based on the number of hits. If this number is equal, the selection is based on $d_T/\mathrm{N_H}$.

If only a single track candidate is required, the track with the lowest $d_T/\mathrm{N_H}$ is selected.

5.5.6 Clustering on OT and IT Hits

The clustering algorithm can act on OT and IT hits simultaneously or perform cluster searches on separate collections of OT and IT hits. In the first case, tracks can contain both IT and OT hits at a time, while in the second case tracks contain solely IT or OT hits.

Based on the summed weight of OT and IT hits associated to MC particles, clusters are subdivided in the following categories:

- the particle has sufficient hits to exceed the cluster threshold in either the OT or IT,
- the particle has sufficient hits both in the OT and IT to form clusters,
- the particle has only sufficient hits to reach the cluster threshold when the OT and IT hits are added, and
- the particle does not have sufficient hits at all to reach the cluster threshold.

The threshold on x and stereo hits to form a cluster are 9 and 8 for the OT respectively, and 7,8 for the IT. Table 5.2 contains results of a sample of about $8{\times}10^4$ tracks, with p >3 GeV, and p_T >500 MeV. As can be seen from the numbers, few tracks depend on the sum of both OT and IT hits to reach the threshold.

Hits	N_{tracks}	Fraction
OT ↑ IT ↓	62898	79%
OT ↓ IT ↑	10736	13%
OT ↑ IT ↑	950	1%
(OT + IT) ↑	93	0.1%
(OT + IT) ↓	5518	7%
Total:	80195	100%

Table 5.1: Fraction of tracks with OT, IT hits above (↑) and/or below (↓) the threshold for recognition by the clustering algorithm as listed in Table 5.2.

The performance for clustering on OT and IT hits simultaneously or separately shows small differences only. Since the determination of cuts on parameters is more difficult if track clusters consist of both OT and IT hits, and the algorithms are more easy to adapt for specific applications, it is decided to run the clustering algorithm on OT and IT hits separately.

5.6 T-Tracking Performance

As introduced in Section 5.3, the key performance measures for a tracking algorithm for online use are the efficiency, ghost rate and execution time. Furthermore, since the algorithm uses the full magnetic field, the track momentum resolution is expected to be a few percent.

5.6.1 Measuring Performance

The efficiency and ghost rate are determined by comparing tracks reconstructed by the algorithm from simulated raw detector data output to those produced by the event simulation, using the MC information.

In the following paragraphs, the algorithm performance is presented for the case where VELO tracks are used to generate seed points, see Section 5.5.1.

Efficiency

The reconstruction efficiency is determined for a sample of MC particles on which the following requirements apply:

- The particle must be reconstructed in the VELO detector.
- The particle momentum must be over 3 GeV.
- The particle transverse momentum must exceed 500 MeV.
- The particle must originate from a B-meson decay.
- The particle must have at least one hit in every T station.

A track is considered to be reconstructed correctly if:

- more than 50% of the tracker station hits in the reconstructed track match with tracker hits associated to the particle, or
- the distance of the reconstructed track and the particle track is less than 10(100) mm in $x(y)$ in T1 and T3, and the reconstructed track momentum matches the particle momentum within 7%.

The latter criterion corresponds to a momentum resolution within 3.5σ for VELO seeded tracks, and 2.4σ for tracks with a Muon seed, see Figures 5.17 and 5.19.

From the MC particles in the sample and the reconstructed tracks, the efficiency is determined using Eq. (5.2).

Ghost Tracks

If the prime track candidate from a particular seed point does not match any MC particle, it is labelled as a ghost track. Ghost tracks with a high p_T could lead to a false identification of B decay events, since high p_T tracks are used as the signature of events containing a B decay.

5.6.2 T-Tracking Parameter Settings

The T-tracking algorithm requires a set of parameters, controlling the cluster search in the x-z and the y-z planes individually. Furthermore, cut values are set to skim the collection of found clusters. These settings determine the performance, and are set to different values depending on the requirements of the algorithm application, when a low ghost rate is more important than a high efficiency, for example.

Cluster Search Parameters

The parameters determining the cluster search efficiency are introduced in Section 5.5.3: the maximum distance between two subsequent hits $d_{\min}$, the total cluster width $d_{\max}$ and the minimum number of hits required for a cluster.

Since the same clustering algorithm is used for both the track search in the x-z plane and the stereo confirmation of these tracks in the y-z plane, the parameters used for the two cluster searches in the OT roughly reflect a factor 10 in resolution difference for the channels in the x and y directions. Table 5.2 contains the settings for the clustering algorithm for both cases. The $d_{\min}$ and $d_{\max}$ parameters are expressed in terms of the minimum resolution (MR). This is the minimum slope difference which is still measurable by the OT. The MR is the wire pitch divided by the distance between the most downstream layer in T3 and the average z coordinate of the magnet focal plane: 5.25 mm/(9400-5200) mm.

OT Parameter	x-z	y-z	
ΣW_H	9	8	
$d_{\min}$	0.7	7	MR
$d_{\max}$	1.5	15	MR
IT Parameter	x-z	y-z	
ΣW_H	7	8	
$d_{\min}$	0.07	3	MR
$d_{\max}$	0.4	8	MR

Table 5.2: Parameter settings for the clustering algorithm for the clustering in the x-z and y-z planes, for the OT and IT detectors. ΣW_H is the sum of the hit weight, $d_{\min}$ and $d_{\max}$ are expressed in units of the minimum resolution (MR), see text.

The settings are optimised for high efficiency and low ghost rate using MC particles which satisfy the conditions listed in Section 5.6.1.

Cuts on Found Tracks

The collection of tracks found by the algorithm contains ghosts and clones. From an analysis of the cluster parameters (see Section 5.5.5) of MC tracks, correctly reconstructed tracks, and ghost tracks, the cluster parameter cuts are optimised to eliminate ghost tracks while reducing the efficiency as little as possible. In Table 5.3, the cut values are summarised for tracks reconstructed in the IT and OT. Separate cut values apply to the track segments in the x-z and y-z planes.

OT Track Cuts		
Parameter	x-z	y-z
σ	<60	<6
χ^2	<90	<9
$d_T/\mathrm{N_H}$	<0.14	<1.4
IT Track Cuts		
Parameter	x-z	y-z
σ	<4	<1
χ^2	<10	<2
$d_T/\mathrm{N_H}$	<0.018	<0.7

Table 5.3: Cuts on the parameters of track segments in the x-z and y-z planes, reconstructed in the OT and IT.

A very effective parameter for the selection of correctly reconstructed tracks is the total cluster width d_T divided by the number of hits, i.e. the average distance t_x space between hits, defined as:

$$\frac{d_T}{\mathrm{N_H}} = \frac{10\ w_{\mathrm{max,x}}}{\mathrm{N_{H,x}}} + \frac{w_{\mathrm{max,y}}}{\mathrm{N_{H,y}}}, \tag{5.10}$$

where $w_{\mathrm{max,x}}$, $w_{\mathrm{max,y}}$ represents the cluster width in the x and y directions, respectively.

Two-dimensional histograms of $d_T/\mathrm{N_H}$ versus the total number of hits of a track $\mathrm{N_H}$ are plotted in Fig. 5.14, for correctly matched tracks and ghost tracks reconstructed in the OT. From the plots it can be seen that, although correctly reconstructed tracks have different average values from the ghost tracks, the parameters overlap for a certain fraction of the tracks. Currently, a one-dimensional cut of <2.5 is used for d_T/N_T, but the value and two-dimensional contour of the cut may vary depending on the inefficiency and ghost rate allowed by the application.

Final Track Selection

Depending on the application, the T-tracking algorithm returns multiple tracks with a single seed point, or selects the best track candidate.

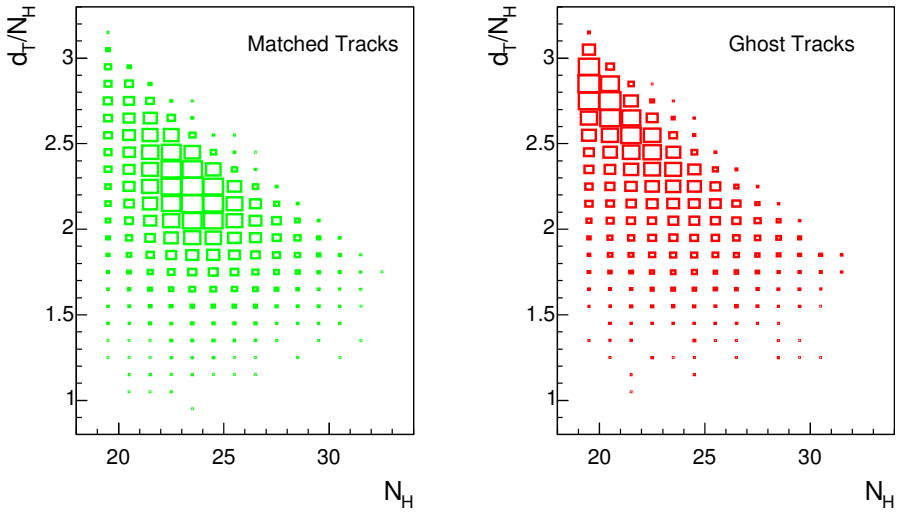

Figure 5.14: Two-dimensional histograms of the cluster width d_T divided by the number of hits N_H versus N_H. Histograms are plotted for OT tracks matching a MC particle (left) and ghost tracks (right). The size of the box corresponds to the number of entries in the specific bin.

Returning multiple tracks enhances the efficiency, but also enlarges the fraction of ghost tracks. This is useful when for example an invariant mass is reconstructed from the tracks: a high efficiency is important, while ghost tracks are effectively eliminated by a reconstructed invariant mass criterion.

If a single track candidate is required, a selection is made on the largest number of hits. If the number of hits of two track candidates is equal within 1 hit, the track with the lowest d_T/N_H is selected.

5.6.3 Results

Efficiency

To determine the algorithm efficiency, L0 accepted, off-line selected events of the benchmark decay channel $B_s^0 \rightarrow D_s^{\mp} K^{\pm}$ are used.

In the left graph in Fig. 5.15, histograms are plotted of the transverse momentum of MC particles and correctly reconstructed tracks. For this histogram, about $2{\times}10^4$ events are used. The efficiency curve versus the transverse momentum resulting from the division of these histograms is displayed in the right plot of Fig. 5.15. For tracks with a p_T over 2 GeV, the efficiency exceeds 90%.

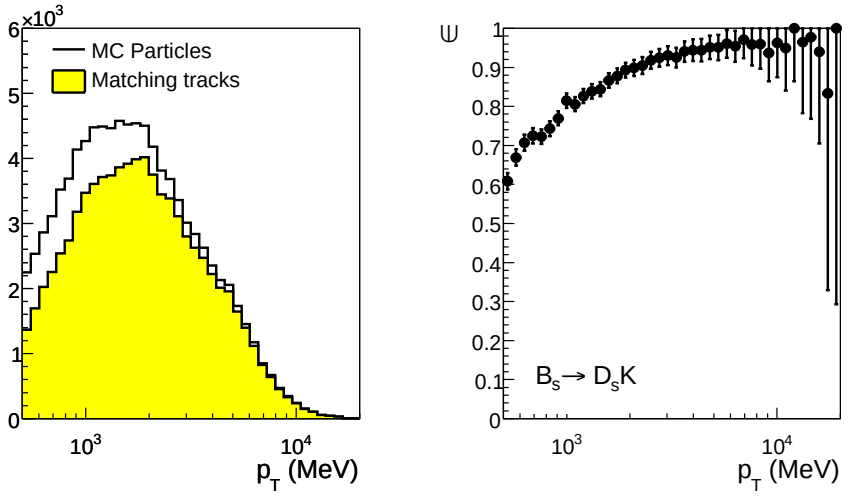

Figure 5.15: The left plot contains histograms of MC particles and matching reconstructed tracks versus momentum p_T for offline selected $B_s^0 \rightarrow D_s^{\mp} K^{\pm}$ events. In the right pane, the fraction (ϵ) of matching tracks is plotted versus the transverse momentum p_T.

Purity and Momentum Resolution

To investigate whether the reconstructed tracks are composed of the hits associated to the MC particle, the fraction of the hits in a reconstructed track matching the MC particle is plotted in Fig. 5.16. As can be seen from the plot, most of the correctly reconstructed tracks share over 70% of the hits with the MC particle. The entries with a small fraction of matched hits are considered a correct reconstruction if the track momentum estimate is within 7% of the true particle momentum.

The momentum estimate of reconstructed tracks (p_{rec}) should have a good resolution with respect to the momentum of the MC particle (p_{MC}). A histogram of the residuals $\delta p/p$ $(= p_{\text{rec}} - p_{\text{MC}})/p_{\text{MC}}$ is plotted in Fig. 5.17. A Gaussian curve is fitted to the histogram; its standard deviation σ is equal to the momentum resolution attributed to the track search algorithm. The resolution is better than 2%, which is a significant improvement with respect to the VELO-TT tracking currently used in the L1 trigger.

Ghost Rate and Momentum Spectrum

As can be seen from the left plot in Fig. 5.18, the number of ghost tracks increases with the number of hits in an event, the event multiplicity. It should be noted that the difference in multiplicity of minimum bias and $B_s^0 \rightarrow D_s^{\mp} K^{\pm}$ events accepted by the L0 trigger is about 5%, invalidating it as a selection criterion.

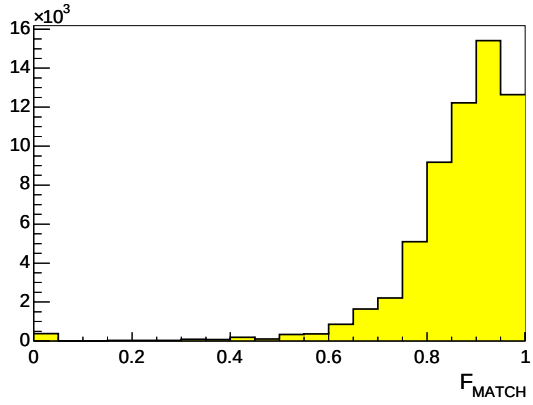

Figure 5.16: Fraction of hits matching to the MC track (F_{MATCH}) for correctly reconstructed tracks.

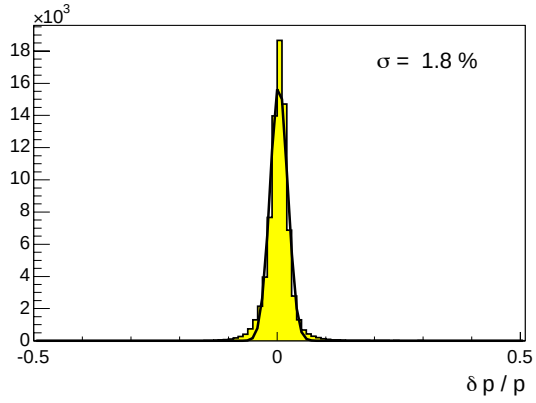

Figure 5.17: Momentum resolution δp/p of tracks matching a MC particle. The σ of the fitted Gaussian curve is taken as the resolution.

The right plot in Fig. 5.18 contains the p_T spectrum of ghost tracks for minimum bias events. The ghost rate decreases with increasing p_T, but the few ghost tracks with high p_T could lead to a false identification of a B decay.

By tuning of the cuts on the track parameters σ, χ^2, and d_T/N_H, a large fraction of the ghost tracks is removed. However, as can be seen from the plots in Fig. 5.14, it is impossible to remove all ghost tracks and simultaneously conserve all correctly reconstructed tracks.

Depending on the application, a trade-off between ghost rate and efficiency must be

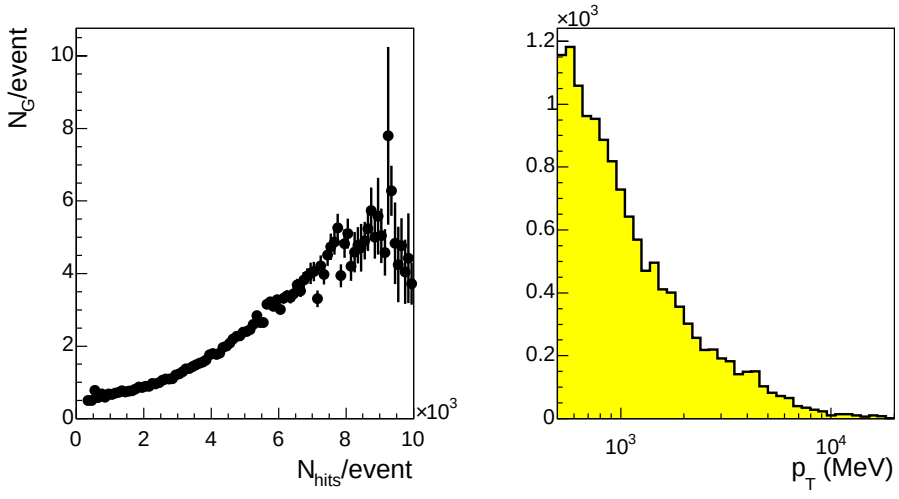

Figure 5.18: In the left graph, the number of ghost tracks N_G per event is plotted versus the total number of hits in the IT and OT, N_{hits}, in the event. On the right, the ghost track p_T spectrum is plotted.

found. For example, for a better performance of trigger applications discussed in the next chapter, some efficiency is sacrificed at the benefit of a low ghost rate for high p_T tracks.

Execution Time

The T-tracking is designed with the aim of fast execution. During the development the focus has been on efficiency and ghost rate rather than the execution time. To define the range of the execution time, an initial measurement of the time consumed by the T-tracking code has been made: on a standard node of the lxplus cluster, the T-tracking algorithm took less than 38 ms to complete the analysis of one event [96]. This number is obtained with the code version used to acquire the performance figures in this thesis. Significant improvements of this number are foreseen by application of the following enhancements:

- Performing application specific track cuts in an early stage of the algorithm, limiting the combinatorics.
- Optimisation of the loop structure, combining loops over found tracks.
- Improved computing power of a future trigger node compared to a present-day lxplus node.

Though it might be optimistic to assume the T-tracking can be applied within the 1 ms average L1 execution time, the foreseen 1 MHz readout scheme offers possibilities to incorporate the T-tracking into the trigger algorithm. In the latter scheme, a single trigger algorithm performing the tasks currently divided between L1 and the HLT. As a result, binary hit response of the T-station channels becomes available for L0 accepted events, opening the opportunity to incorporate the T-tracking into the trigger algorithm.

5.7 Online Muon Reconstruction

For application in the muon trigger algorithms described in Chapter 6, an accurate determination of the muon p_T is crucial since the uncertainty on the p_T is affects the error on the reconstructed mass of a particle. For an efficient background rejection, a p_T resolution better than 10% is desirable.

Tracks reconstructed in the muon stations lack precision to reconstruct the particle p_T with the aforementioned resolution. Consequently, muon tracks must be linked to tracks in other subdetectors to enhance the p_T estimate of the tracks. The T-tracking algorithm is used to perform online reconstruction of muon tracks.

5.7.1 Muon Tracking

To reconstruct tracks in the muon detector for trigger algorithms successive to L0, an identical algorithm is used as the one providing the L0 muon objects [95]. Where the L0 trigger is optimised to avoid false triggers based on a ghost muon track, for subsequent triggering the algorithm is optimised for a high muon reconstruction efficiency [36].

Reconstructed tracks in the muon stations are used to generate seed points, see Section 5.5.2. Starting from these points, track continuations are looked for in the T stations. Finally, it is attempted to match the muon track to L1-VELO tracks. With a track in the muon detectors matched to track segments in the T stations and the VELO detector, the muon trajectory is entirely reconstructed.

5.7.2 Muon Tracks in the T Stations

The procedure to generate a seed point from a muon track and subsequently search the T stations for track continuations is described in Section 5.5.2. The T-tracking algorithm is able to return multiple track candidates from a single muon track seed. Based on the differences in track slopes in the muon detector and T stations $t_{x,1} - t_{x,2}$ and $t_{y,1} - t_{y,2}$, and their averages σ_{t_x} and σ_{t_y} for the x-z and y-z planes respectively, χ^2_t is defined:

$$\chi^2_t = \left(\frac{t_{x,1} - t_{x,2}}{\sigma_{t_x}}\right)^2 + \left(\frac{t_{y,1} - t_{y,2}}{\sigma_{t_y}}\right)^2 \quad . \tag{5.11}$$

Muon track candidates are selected by setting a maximum cut on the track χ^2_t.

5.7.3 VELO Track Matching

By association of a track segment in the VELO to a reconstructed muon track, the precision of its momentum estimate is improved. To match L1-VELO tracks to tracks consisting of segments in the muon detector and eventually in the T stations, the muon track is extrapolated linearly to the focal plane of the magnet described in Section 5.5.1. The result is a three dimensional point (x_μ, y_μ, z_f). From this point, the track slopes in the VELO are estimated, assuming they originate from (0,0,0). In the y-z plane, particles follow straight trajectories, therefore the slope $t_{y,1}$ is directly taken from the reconstructed track in the muon detectors. The slope in the x-z plane is estimated assuming the track originates from the origin: $t_{x,1} = x_\mu / z_f$. Similarly, L1-VELO tracks are extrapolated to the magnet focal plane, resulting in a point (x_V, y_V, z_f) and slopes $t_{x,2}$ and $t_{y,2}$.

Track Slopes Match	σ_{t_x} (mrad)	σ_{t_y} (mrad)
Muon $\leftrightarrow$ T	11.9	7.8
Muon $\leftrightarrow$ VELO	21.5	3.3
Muon+T $\leftrightarrow$ VELO	6.8	7.2
R_{match}	σ_x (mm)	σ_y (mm)
Muon $\leftrightarrow$ VELO	91	13
Muon+T $\leftrightarrow$ VELO	23	33

Table 5.4: Average differences in track slope ($\sigma_{t_{x,y}}$) and position ($\sigma_{x,y}$) for matching of track segments in the muon detector, T stations and VELO detector, see text.

To find the best match between a found track and the L1-VELO tracks, the χ^2_t from Eq. (5.11) and additionally a χ^2_R on the match distance are calculated:

$$\chi^2_R = \left(\frac{x_V - x_\mu}{\sigma_x}\right)^2 + \left(\frac{y_V - y_\mu}{\sigma_y}\right)^2 , \tag{5.12}$$

with σ_x and σ_y the average distances between extrapolated track segments, similar to the χ^2_t definition. The σ parameters for the calculation of χ^2_t and χ^2_R are extracted from an analysis of MC particles with their associated track segments in the VELO, T stations and muon detectors. Table 5.4 contains the σ values for slopes and positions used for the calculation of χ^2_t and χ^2_R for the various track configurations.

As displayed in the table, the σ values for the track slope errors in the y-z plane for the T stations are dominated by the resolution of the T stations in the y coordinate rather than the particle deflection. In the y-z plane, the slope estimate from the muon stations is more accurate than the slope estimated from T stations. Consequently, the t_y estimate from the T stations is not used for VELO track matching or the momentum estimate.

For the combinations of a muon track and a L1-VELO track, the χ^2_t and χ^2_R are calculated. Track candidates are selected on the overall parameter $\chi^2_\mu = \chi^2_t + \chi^2_R$, which

must be below a cut value. If a single candidate is required, the track with the lowest χ^2_μ is selected.

5.7.4 Muon Momentum Estimate

From a track in the muon detectors, the momentum is estimated using the p_T-kick method, described in Section 5.1. When using M2 to M5 for the track reconstruction, the resolution is about 40%. A large contribution to the error originates from the track deflection in the calorimeter material. Inclusion of the M1 station, placed in front of the calorimeter, improves the momentum resolution to 25% [97]. Since it is doubtful whether M1 will be installed on time, data from this station is not used for the muon momentum estimate.

When a track in the T stations is linked to a muon track, its slope and position are known with a better precision. The extrapolation towards the magnet focal plane becomes more accurate, improving the track slope estimate. Consequently, the momentum estimate of the muon improves to 8.8%.

The best momentum resolution is obtained when a track contains segments in the muon detector, the T stations and the VELO. The plot in Fig. 5.19 contains residuals of the reconstructed momentum p_{rec} relative to the MC momentum p_{MC}: δp/p=$(p_{rec} - p_{MC})/p_{MC}$. In the plot, the particle momentum is estimated from tracks in the muon stations only, and with the inclusion of track segments in the T stations and VELO detector. The resolution σ is extracted from Gaussian fits to the histograms.

The inclusion of the T stations in the reconstruction of muons from tracks in the muon detectors improves the momentum resolution from 40% to 9%. It enhances the matching with tracks found in the VELO detector, which in its turn improves the resolution on the momentum to better than 3%.

In the next Chapter, triggering algorithms based on online reconstructed muons are presented.

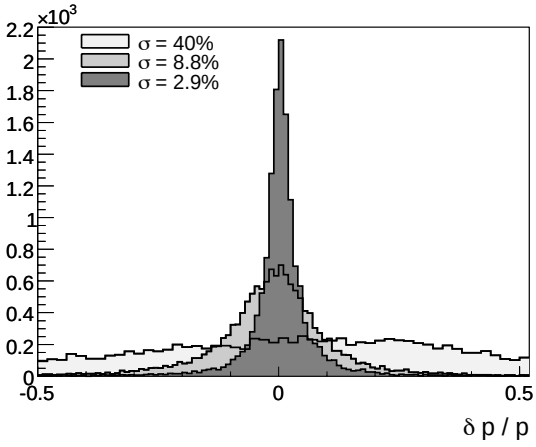

Figure 5.19: Momentum resolution (δp/p) of reconstructed muon tracks, using track segments:
1. from the muon station only (light shade),
2. from the muon stations and the T stations (medium shade),
3. from the muon stations, the T stations and the VELO (dark shade).

The resolution figures σ are extracted from Gaussian fits (not drawn).

Chapter 6

The Tracker In The Trigger

The T-tracking algorithm for online track reconstruction, presented in the previous chapter, is used for triggering at Level-1 (L1). In the L1 trigger, bandwidth is accommodated for a generic trigger, and triggers providing an inclusive selection of B meson decays. The bandwidth division for the L1 and High Level Trigger (HLT) is discussed in the following section. A generic L1 trigger using the T-tracking is presented in Section 6.2. Sections 6.3 and 6.4 contain descriptions and performance figures of inclusive triggers using online reconstructed (di)muons. Finally, Section 6.5 contains the conclusions on the application of the T-tracking algorithm in the L1 trigger, and mentions the performance at HLT output rates.

6.1 Trigger Bandwidth Division

Following the Level-0 (L0) trigger, the L1 and HLT reduce the data stream from 1 MHz to a 2 kHz output rate at which events are written to mass storage. The output bandwidth is shared between the data streams from trigger algorithms focusing on exclusive as well as on inclusive selections of B decays.

6.1.1 Physics Motivation

Application of offline selection criteria for specific B decay channels on the events selected by the L1 trigger, the HLT output rate is estimated below 200 Hz for exclusive B decay events [28]. These events are selected on their relevance for the measurement of CP violation, the prime physics goal of the experiment.

The remaining output rate is reserved to gather a data sample containing inclusive selections with high statistics. A large inclusive selection of events containing B decays offers the opportunity to search for rare or unforeseen B decay channels which are relevant to CP violation measurements, but are not favoured by the existing generic L1 trigger.

Additionally, a large inclusive sample of events containing J/ψ decays is indispensable to gain insight in the systematic effects of the experiment. By not requiring a minimum track Impact Parameter (IP), no biases originating from the acceptance, or with respect

to the B meson decay time are introduced. Apart from the unbiased analysis of $B \to J/\psi X$ decays, the well-known J/ψ mass of 3097 MeV and its narrow decay width of less than 0.1 MeV make it particularly useful for the following applications:

- the determination of the vertex and proper time resolution of the VELO detector, and
- the measurement of the magnetic field integral, track momentum resolution as well as systematic effects for the full acceptance and geometry of the experiment.

A muon trigger is useful to gather an inclusive selection of events containing B or J/ψ decays. To have a good sensitivity for all kinds of B decays containing muons, three muon triggers (with large overlaps) are implemented:

- Generic dimuon trigger. This trigger uses the reconstructed invariant mass from two muon tracks. Any mass between a lower threshold and the B meson mass is accepted. To suppress the dimuon background originating from the Drell-Yan processes, a minimum lifetime is required by a minimum cut on the IP.
- Dimuon J/ψ trigger. This trigger accepts an event if the dimuon invariant lies within a narrow mass window around the J/ψ mass. No minimum IP is required.
- Single muon trigger. Through the large branching fraction for semi-leptonic B decays, a trigger on single muons with high p_T and significant IP selects an enriched B decay event sample. The triggered muon also improves the flavour tag on the B decay.

All muon triggers require a good resolution on the p_T of the muon. The online reconstruction of muon tracks and the estimation of the p_T is performed using the T-tracking algorithm according to the description in Section 5.7. Sections 6.3 and 6.4 contain the implementation and performance of the muon triggers.

6.1.2 Bandwidth Limitations

The output rate of the L1 trigger is designed not to exceed 40 kHz. Of this rate, 30 kHz is reserved for an event stream containing many B decay modes, selected by the generic L1 trigger. The remaining 10 kHz is reserved for inclusive B decays, of which 5.6 kHz is allocated for muon triggers. The division of the L1 output rate is visually represented in the left diagram in Fig. 6.1.

The right diagram contains the bandwidth division for the HLT. Apart from the 200 Hz rate reserved for the exclusive B decays, 300 Hz is appointed to an inclusive D^* trigger, offering the possibility to study charm physics, to measure $D^0\overline{D}^0$ mixing, and to calibrate the particle identification systems for the separation of $K^\pm$ and $\pi^\pm$ particles [98]. The remaining 1.5 kHz is allocated for muon triggers, including 600 Hz for a trigger on the dimuon invariant mass and 900 Hz for single muons with a significant IP.

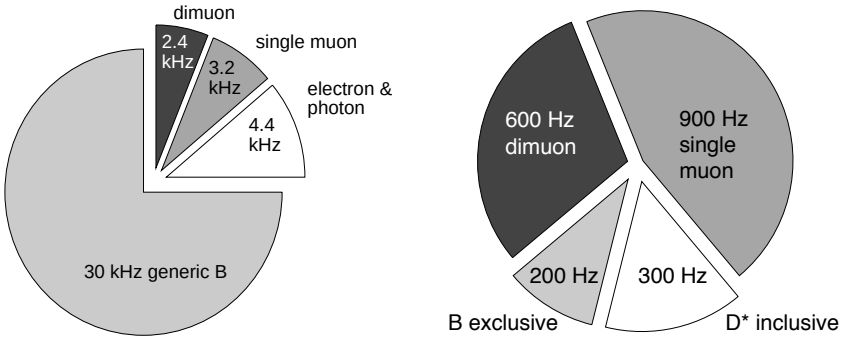

Figure 6.1: Pie diagrams of the output bandwidth division for the L1 trigger (left) and the HLT (right).

The triggers presented in this chapter operate at L1. They use 1 MHz L0 accepted events at the input, their output will be further digested by the HLT. A L1 generic trigger with an output rate of 30 kHz is presented in Section 6.2. For the inclusive data stream, a combined trigger on single and dimuons delivering a total output rate of 5.6 kHz is presented in Section 6.4.

For the single and dimuon triggers, efficiency figures will be presented for output rates which range down to their respective bandwidth shares at the HLT output. At these rates, the trigger output can be directly written to mass storage. These numbers only serve as estimates, since the parameters of the trigger algorithms are not specifically tuned for these low output rates.

6.2 Level-1 Generic Trigger

For the generic selection of B decays at L1, the algorithm described in Section 2.9.2 is used. For the L1 decision, it uses the following parameters to construct a L1 variable:

- the transverse momentum p_T of the two tracks with the highest p_T,
- the Impact Parameter (IP) of these tracks, and
- the IP significance (IPS), which is defined as IP/σ_{IP}, where σ_{IP} is the error on IP [99].

In the L1 trigger algorithm, on average 8 L1-VELO tracks are reconstructed (see Section 2.9.2). Of these tracks, the two highest p_T tracks are selected and the separate logarithmic sums of their IP and their p_T are calculated. The trigger decision criterion is effectively a two-dimensional cut on these two parameters. To enhance the trigger sensitivity for specific events, a bonus β is added to the L1 variable if a VELO track is matched to a muon track or calorimeter cluster found by the L0 trigger [100].

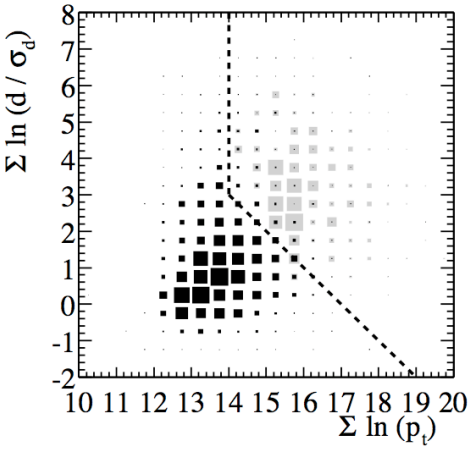

Figure 6.2: Distributions for minimum-bias events (black boxes) and $B_s^0 \to D_s^{\mp} K^{\pm}$ events (grey boxes) of the two variables Σ ln(p_T) and Σ ln(IPS). The dashed line represents the cut applied for the L1 decision, see text.

Fig. 6.2 contains histograms of these variables for minimum bias events and $B_s^0 \to D_s^{\mp} K^{\pm}$ events. The dashed line represents the 2 dimensional cut value on the L1 variable which determines the trigger decision.

The IP is determined by the VELO with a resolution of 100 μm [28]. Currently, the track p_T is estimated from the VELO-TT tracking, providing a 25% resolution for tracks with a p_T of 1 GeV.

In Table 6.1, the L1 trigger performance is summarised for L0 accepted, offline selected events of several benchmark B decay channels, presented in Chapter 1. The efficiencies are given for a 4% retention, assuming the L1 trigger has an input rate of 1 MHz and an output rate of 40 kHz. Recent studies have shown that a cut on the Σln(p_T) alone suffices for a good L1 performance, simplifying the selection.

B decay	L1 efficiency (%)
$B^0 \to \mu^+\mu^- K^*$	78.5±1.1
$B^0 \to J/\psi\,(\mu^+\mu^-) K_S^0$	67.7±0.9
$B_s^0 \to D_s^{\mp} K^{\pm}$	62.6±0.4

Table 6.1: Level 1 trigger performance for benchmark B decay channels. Trigger efficiencies are given for L0 accepted, offline selected events at a retention of 4% (from Ref. [28]).

6.2.1 L1 Performance Using T-Tracking

The L1 algorithm needs the track momentum for the trigger decision. As an alternative to the VELO-TT tracking, the T-tracking algorithm is used to determine the momentum for L1-VELO tracks. The momentum estimate of the T-tracking accounts a few percent, using binary hit data from the T stations. When using T-tracking, described in Sections 5.4.2 and 5.5, data from the TT station is not used for the trigger decision. T-tracking seed points are extrapolated from L1-VELO tracks, using the method described in 5.5.1. Of the tracks found by the algorithm, the p_T is estimated using Eq. (3.2), and the L1 variable is calculated from the logarithmic sum of the two highest p_T tracks. To suppress ghost tracks, a 500 MeV minimum p_T cut is applied. In the case that no track in the T stations is found for a L1-VELO track, the p_T is set to 400 MeV, corresponding to the average p_T of VELO tracks [37]. If no track candidates are present in an event, the resulting L1 variable amounts to 2 ln(400)=12.

The L1 variable using the track p_T estimate from the T-tracking algorithm is plotted in the left pane of Fig. 6.3 for minimum-bias and $B_s^0 \to D_s^{\mp} K^{\pm}$ events.

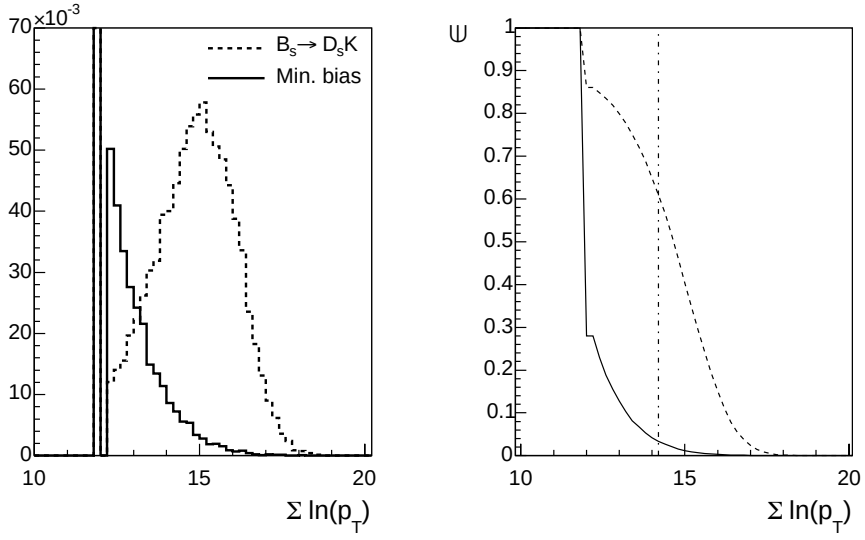

Figure 6.3: On the left, histograms of the L1 trigger variable $\Sigma \ln(p_T)$ for $B_s^0 \to D_s^{\mp} K^{\pm}$ events and minimum bias events are plotted with dashed and solid lines respectively. The curves in the right plot represents the efficiency (ϵ): the fraction of events exceeding the L1 parameter versus the cut on the L1 parameter. The vertical line indicates 4% minimum bias retention rate.

The value of the cut on the L1 parameter is determined by the trigger input and output rates. At an input rate of 1 MHz and an output rate of 40 kHz, the L1 trigger

rejects 96% of its input events. The cut on the L1 parameter is set at the point where 4% of the minimum-bias events are accepted by the trigger. The efficiency follows from the fraction of signal events passing the L1 trigger decision using the L1 cut setting.

Output rate	Efficiency
40 kHz	61.0±0.3%
30 kHz	56.5±0.4%

Table 6.2: L1 trigger efficiency for $B_s^0 \to D_s^{\mp} K^{\pm}$ events at two output rates. The uncertainties originate from the analysis statistics.

In the right pane of Fig. 6.3, the fraction of events exceeding the L1 parameter is plotted versus the L1 parameter value. The vertical line indicates the cut value where the retention of minimum-bias events is 4%. The procedure is repeated for a trigger retention of 3%, and the performance is summarised in Table 6.2. The tail of the L1 variable distribution for minimum-bias events extends to high values, caused by ghost tracks faking a high p_T, mentioned in Section 5.6.3.

The performance is similar to the current L1 algorithm, making a generic L1 trigger using the T-tracking for track momentum estimation a viable alternative to the VELO-TT based trigger.

6.2.2 L1 Confirmation Using T-Tracking

Instead of a substitute for the VELO-TT based L1 algorithm, the T-tracking based L1 trigger algorithm can also confirm the L1 decision. To reduce L1 output rate, the L1 algorithm is repeated using the T-tracking to provide a better resolution on the track p_T with respect to the VELO-TT tracking. Still, data available at L1 is used, extended with binary channel hit information from the T stations.

The L1 trigger confirmation is focused on the removal of events that have tracks with a fake high transverse momentum. By improving the momentum estimate and the addition of tracker data, low-momentum tracks faking a high transverse momentum are effectively eliminated.

The HLT uses detector data with full resolution, allowing precise track reconstruction with complex algorithms to exclusively select events containing specific B decays vital to measurements of CP violation. By application of the L1 confirmation, the HLT input rate is reduced. This leaves more computing resources for the remaining events, allowing for more sophisticated HLT algorithms with higher discriminative power.

Similar to the description in the previous paragraph, minimum bias events are used to determine the L1 cut value and the retention rate. Subsequently the efficiency is determined from the ratio of signal events passing a cut on the L1 trigger variable. In the case of a L1 confirmation algorithm, both event samples have passed the L1 trigger. Fig. 6.4 contains a graph of the efficiency versus retention for the T-tracking algorithm used for the confirmation of the L1 algorithm on L1 accepted events.

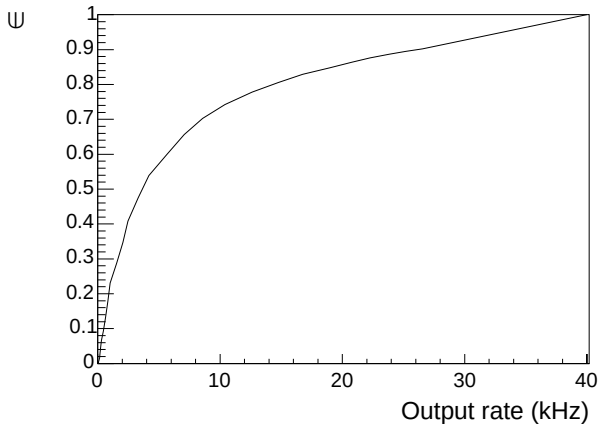

Figure 6.4: Efficiency (ϵ) versus output rate for the L1 confirmation algorithm. Naturally, the efficiency is 1 when the output rate is equal to the input rate of 40 kHz.

From the graph it is seen that the L1 output rate is reduced from 40 kHz to 23 kHz, conserving 90% of the signal events. If the L1 algorithm using the VELO-TT tracking is followed by the L1 confirmation using the T-tracking, the resulting efficiency for $B_s^0 \to D_s^{\mp} K^{\pm}$ events is $62.6\% \times 90\% = 56.3\%$ at an output rate of 23 kHz.

6.3 A Muon Trigger

For the inclusive selection of events containing B decays, trigger algorithms using muons are deployed. The T-tracking algorithm performs the online reconstruction of muon tracks, described in Section 5.7. The reconstructed muons are used for three individual triggering algorithms, of which two are based on the dimuon invariant mass and one uses the single muon IP and p_T. The dimuon triggers are described in Section 6.3.1 and 6.3.1, the single muon trigger is presented in Section 6.3.3

A Trigger Using Dimuon Invariant Mass

A trigger based on the invariant mass provides an inclusive selection of B decays. To suppress $\mu^+\mu^-$ background events originating from Drell-Yan processes, either a minimum lifetime is required, or the invariant mass is required to correspond to a well-known particle. Both types of triggers are implemented.

Firstly, a generic dimuon trigger accepts events with a reconstructed invariant mass above 1 GeV. The background is eliminated by setting a minimum IP requirement.

A positive IP requirement implies a minimum requirement on the particle lifetime: a higher IP cut selects longer-lived particle decays.

Secondly, the dimuon mass can be used to trigger on a specific particle. All available muon tracks, regardless of their IP, are used for the particle reconstruction, resulting in a trigger without a bias on the decay time. To effectively eliminate the combinatoric background, narrow windows around the particle mass are defined. Due to its well-known mass and intrinsic narrow decay width, a large sample of events containing a J/ψ is particularly useful for the calibration of energy and momentum resolution, and helps understanding systematic effects. Apart from calibration purposes, they are useful for the unbiased decay time analysis of $B \to J/\psi X$ decays.

For a precise calculation of the dimuon invariant mass, the muon momentum vector must be reconstructed as accurate as possible. The 40% momentum resolution of tracks found in the muon stations is not sufficient for efficient reconstruction of J/ψ particles. With associated track segments in the T stations and VELO detector, the invariant mass is reconstructed with higher precision.

The generic and specific triggers using the dimuon mass have different requirements on the muon tracks for the invariant mass reconstruction, and are discussed below separately. The dimuon trigger performance is illustrated using reconstruction of offline selected $B^0 \to J/\psi\,(\mu^+\mu^-)K^0_S$ events.

6.3.1 A Generic Dimuon Mass Trigger

The generic dimuon trigger accepts reconstructed masses in the range of 1 GeV to the B mass, 5.5 GeV. It is suited for triggering B-events in which the invariant mass of the $\mu^+\mu^-$ covers a large range due to the decay kinematics, as is the case in $B^0 \to \mu^+\mu^- K^*$ decays. Additionally, this trigger is used to select $B^0_s \to \mu^+\mu^-$ decays.

The tracks used in the reconstruction of the invariant mass for the generic dimuon trigger comply to the requirements listed in Table 6.3. The minimum IP threshold implies that whether or not the muon track has a track segment in the T stations, it must have an associated L1-VELO track. This requirement effectively eliminates ghost tracks, but introduces inefficiencies since not all muons necessarily have an associated L1-VELO track.

By introducing a cut on the χ^2_μ, defined in Section 5.7.3, ghost tracks are eliminated. The muon candidates passing the cuts are used to reconstruct an invariant mass, using all possible track combinations. If multiple candidates are present, the one with the highest mass is used.

6.3.2 A Dimuon J/ψ Mass Trigger

The purpose of the specific mass dimuon trigger is to provide a sample containing lifetime unbiased dimuon decays from a particle with well known properties. The J/ψ, with its narrow decay width, is particularly suitable. For this algorithm, no VELO segment is

required allowing for event selection without the introduction of lifetime biases. The momentum resolution of tracks with segments in the muon detector and the T stations is about 9%, allowing a sufficiently precise reconstruction of the particle invariant mass.

Muon Track Selection

Since track candidates are not required to have a segment in the VELO detector, multiple configurations of tracks are used for the invariant mass reconstruction.

Dimuon Track Requirements						
	Generic Mass			J/ψ Mass		
IP	$>$	0.12	mm			
χ^2_μ (VELO-T)	$<$	9.5		$<$	9.5	
χ^2_t (Muon-T)				$<$	0.95	
p_T	$>$	500	MeV	$>$	300	MeV
W	$>$	1.00	GeV			
$\lvert M_{J/\psi} - W \rvert$				$<$	300	MeV

Table 6.3: Requirements on the tracks and reconstructed invariant mass W for the dimuon trigger on the generic and J/ψ mass $M_{J/\psi}$. The χ^2 cuts for the J/ψ mass trigger are applied according to the track selection procedure represented in Fig. 6.5.

When multiple track candidates are associated to a single track in the muon detectors, the prime candidate is selected using a track selection algorithm which operates in two steps: firstly, the track with an associated L1-VELO track with the lowest χ^2_μ is selected. If the χ^2_μ is below a maximum cut value, the track is accepted as the best muon track candidate. Secondly, when no track is accepted yet, the track with the lowest χ^2_t using track segments in the muon detector and the T stations is selected. If a track χ^2_t is below the cut value, the track is accepted. If not, the track is rejected and no muon candidate is stored. Fig. 6.5 contains a flowchart representation of the muon track selection procedure described above.

It should be noted that the χ^2_μ for the matching of the VELO, T station and muon track segments is calculated using the σ values from Table 5.4. Depending on the presence of a track segment in the T stations, the corresponding σ values are used. If no VELO track with a χ^2_μ below the cut value is found, the best track candidate is selected based on the lowest χ^2_t defined in Eq. (5.11). The cut values are listed in Table 6.3.

To avoid large inefficiencies due to the χ^2_μ requirements, single muon track candidates are accepted regardless of their χ^2_μ values.

Following the selection procedure, the invariant mass is calculated for all possible track candidate combinations.

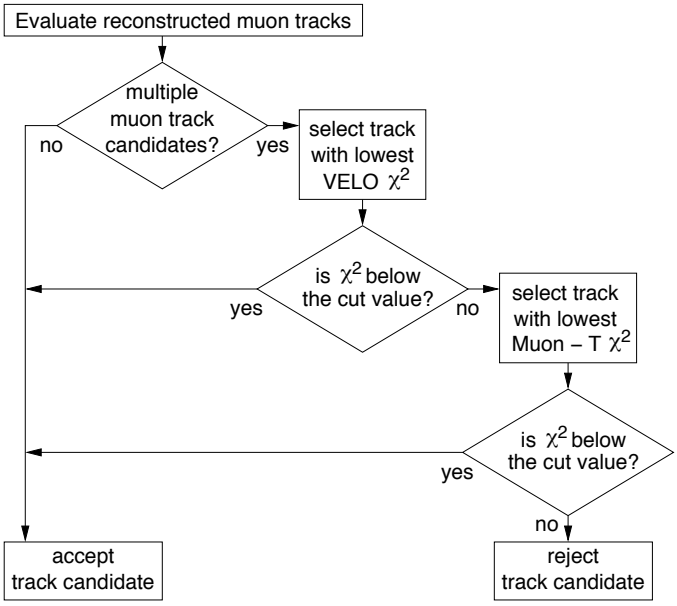

Figure 6.5: Flowchart for the track selection algorithm. The χ^2 cuts applied for the VELO and Muon-T matching are listed in Table 6.3.

Invariant Mass Selection

All combinations of selected muon tracks are used to reconstruct an invariant mass. For every possible dimuon combination the invariant mass is evaluated to be inside the J/ψ or B mass window.

The width of the mass windows centred around the J/ψ mass depends on the required trigger retention. The procedure to determine the retention and efficiency of the J/ψ dimuon trigger is presented in the next section. To reach the nominal retention listed in Table 6.3, a 300 MeV window is applied around the J/ψ mass.

Dimuon Trigger Performance: J/ψ Reconstruction

Following the procedures for track selection and invariant mass reconstruction described in the preceding paragraphs, the dimuon J/ψ mass is used as a trigger: events are accepted if they have a dimuon mass inside a symmetrical mass window around the J/ψ mass.

The trigger efficiency is determined using a signal sample of 29k offline selected $B^0 \to J/\psi\,(\mu^+\mu^-)K^0_S$ events. The left plot in Fig. 6.6 contains a histogram of the invariant mass for online reconstructed muons in the range from 2 to 4 GeV. The average of the fitted double Gaussian curve corresponds within 1% to the true J/ψ mass. The σ of the

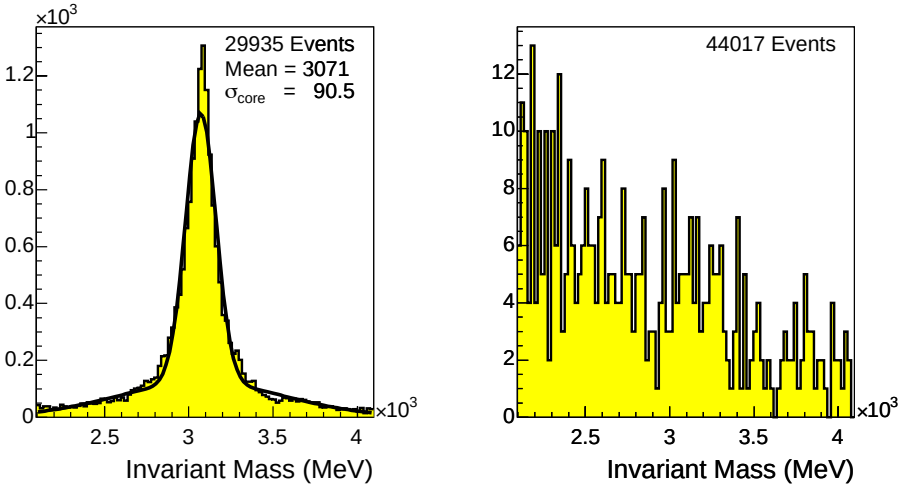

Figure 6.6: On the left, the invariant mass spectrum is plotted for offline selected $B^0 \to J/\psi(\mu^+\mu^-)K^0_s$ events. The peak at the J/ψ mass is fitted with a double Gaussian curve, of which the average and σ of the core are displayed. The right plot contains the spectrum for L0 accepted minimum-bias events.

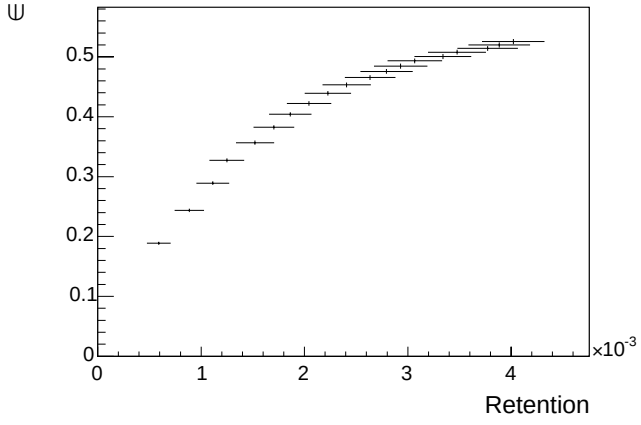

Figure 6.7: Efficiency ϵ versus the retention for the dimuon J/ψ mass trigger.

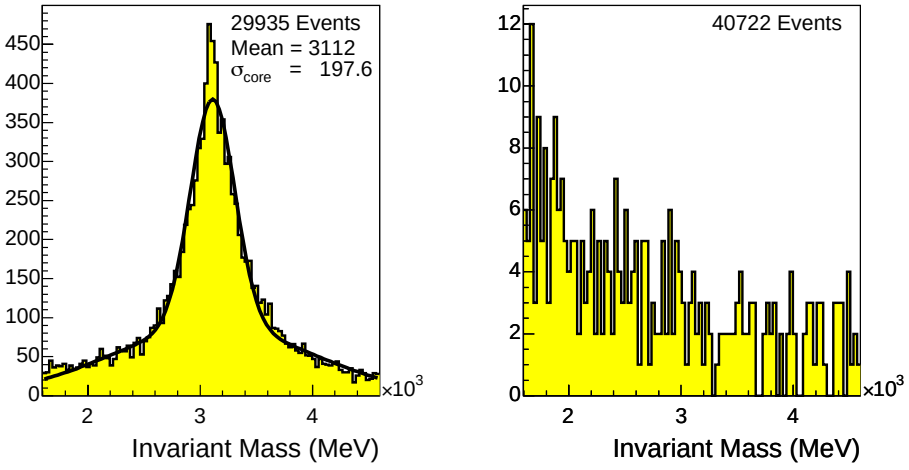

Figure 6.8: On the left, the invariant mass spectrum is plotted for offline selected $B^0 \to J/\psi(\mu^+\mu^-)K^0_S$ events. The peak at the J/ψ mass is fitted with a double Gaussian curve, of which the average and σ of the core are displayed. The right plot contains the spectrum for L0 accepted minimum-bias events. The dimuon invariant mass is reconstructed without data from the VELO.

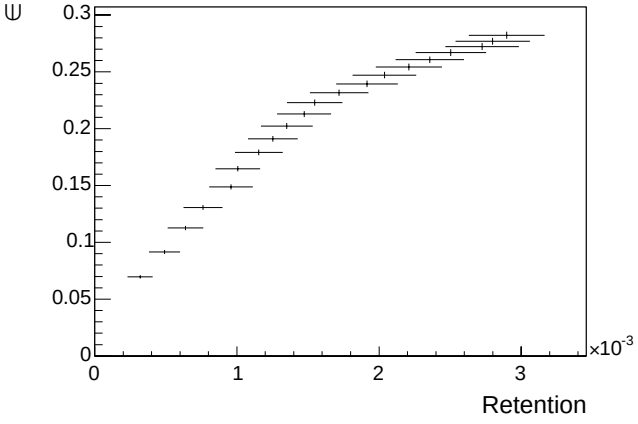

Figure 6.9: Efficiency ϵ versus the retention for the dimuon J/ψ mass trigger, when the VELO detector is omitted.

core of the peak is taken as the resolution on the reconstructed J/ψ mass, and accounts 90.5 MeV.

The trigger retention is determined using minimum bias events. If two or more muon tracks are present in a minimum bias event, it is possible that an invariant mass inside the J/ψ mass window is reconstructed. The right plot in Fig. 6.6 contains the resulting invariant mass spectrum from 44k of L0 accepted minimum bias events.

The width of the symmetrical mass window around the J/ψ mass determines the fraction of minimum bias events accepted by the trigger. The retention, but also the efficiency is affected by the mass window width. Fig. 6.7 contains a plot of the trigger efficiency versus the retention, obtained by varying the mass window width. With an input rate of 1 MHz, the plot covers the output range up to 4 kHz.

In the unlikely scenario that the VELO detector is unable to provide data to the L1 trigger algorithm, the dimuon J/ψ mass trigger is implemented using online muon reconstruction in the muon detector and T stations only. Similar to Fig. 6.6, the resulting invariant mass spectrum is plotted in the left pane of Fig. 6.8. The peak is fitted with a double Gaussian, of which the average corresponds to the J/ψ mass within 0.5%. Compared to the σ of the fit plotted in Fig. 6.6, the mass resolution has increased to 198 MeV, due to the 9% momentum resolution on the track p_T for tracks without an associated L1-VELO track. The right pane of Fig. 6.8 contains the invariant mass spectrum for minimum bias events. Similar to Fig. 6.7, the graph in Fig. 6.9 contains the trigger efficiency versus the retention in the 0 to 3 kHz output range. When omitting the VELO, the trigger performance for a retention of 1 to 3×10^{-3} is about 60% relative to the performance with the VELO included.

6.3.3 A Single Muon Trigger

Even more straightforward and robust than a dimuon trigger is a single muon trigger. As is seen from the plot in Fig. 1.5, single muons with a high p_T are likely to originate from a B decay. To suppress the muons originating from D-decays rather than B decays, and eliminate the muon background from high-energy kaons and pions, minimum cuts on the IP of 0.15 mm and p_T of 2.3 GeV are applied.

Single Muon Track Requirements			
IP cut	$>$	0.15	mm
χ^2_μ cut	$<$	5.0	
p_T cut	$>$	2.3	GeV

Table 6.4: Requirements on muon tracks in the single muon trigger.

The requirements listed in Table 6.4 are applied to all reconstructed muon tracks in an event. If one or more candidates satisfy the requirements, the event is accepted.

To reduce the amount of minimum bias events accepted by the trigger based on a ghost track faking a high p_T, a maximum cut is applied to the track χ^2_μ, defined in

N Events	Fraction	MC Event Selection
44847		Offline selected $B_s^0 \to D_s^{\mp} K^{\pm}$ events
3706		Events with a sl-muon in the 10-300 mrad acceptance
650	1.000	Events with a sl-muon with IP_{MC} >0.15 and $p_{T,MC}$ >2.3 GeV
		Muon and L1-VELO reconstruction
628	0.966	Events with a muon track from the sl-muon
434	0.668	Events with a L1-VELO track with IP above threshold
		Online Muon Reconstruction using T-tracking
290	0.446	Events with reconstructed muon above threshold
244	0.375	Events with the sl-muon reconstructed above threshold
46	0.071	Events with another reconstructed muon above the threshold

Table 6.5: On top: fractions of $B_s^0 \to D_s^{\mp} K^{\pm}$ events with a semi-leptonic (sl-)muon of the opposite B, selected on MC parameters. In the middle part, event fractions containing a sl-muon with correctly reconstructed muon and L1-VELO tracks are given. The bottom of the table contains the relative online reconstruction efficiencies. The threshold comprises the IP and p_T cuts listed in Table 6.4.

Section 5.7.3. To evaluate the efficiency and retention variation, the value of the χ^2_μ is varied.

Single Muon Trigger Performance

To determine the single-muon trigger efficiency, offline selected $B_s^0 \to D_s^{\mp} K^{\pm}$ events are used as the signal sample. In addition, the opposite-side B is required to decay semileptonically into a muon.

This decay channel is an established benchmark channel for LHCb, and is discussed in Section 1. It is very unlikely that a muon exceeding the IP and p_T threshold originates from the selected decay of the signal-B, therefore this channel is used to demonstrate the possibility to trigger on the tagging-B, such that an intrinsically good flavour tag is obtained.

For a proper determination of the single muon trigger efficiency, the muon from the B decay is required to be in the 10 to 300 mrad acceptance of the detector. Additionally, threshold cuts on the p_T of 2.3 GeV and 0.15 mm on the particle IP are applied. The top section of Table 6.5 contains the event yields for these selection criteria. To determine the relative trigger efficiency, the fraction of events with a semileptonic muon in the acceptance, and above the p_T and IP threshold cuts is set to 1.

For the semileptonic muons above the threshold cuts, the reconstruction of tracks in the muon detector and L1-VELO tracks is not 100% efficient. These effects are accounted for separately, and are listed in the middle section of Table 6.5.

In the bottom half of the table, the reconstruction efficiencies of the online muon reconstruction are listed. As is the case with the other triggers discussed in this chapter,

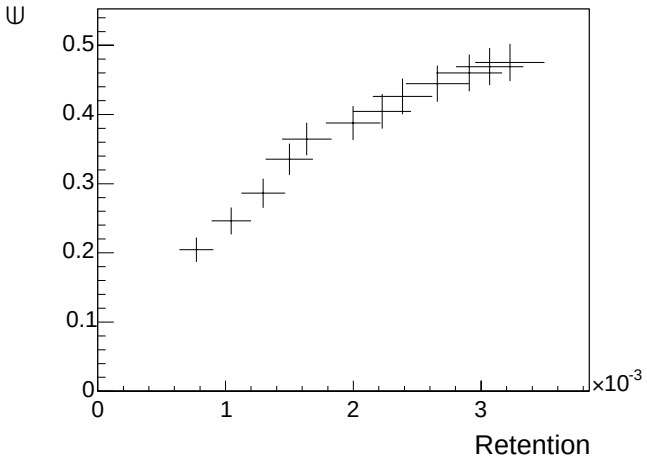

Figure 6.10: Efficiency (ϵ) versus retention for a single muon trigger. Every data point corresponds to a cut on the track χ^2_μ.

the efficiency is correlated with the trigger retention. The trigger efficiency is plotted versus the retention in Fig. 6.10. Every data point corresponds to a setting of the track χ^2_μ cut. Using 1 MHz L0 accepted events as the trigger input, the output rate plotted in the figure ranges from 800 Hz to 3.2 kHz. At the nominal output rate for L1 of 3.2 kHz, the trigger efficiency is 47%.

The HLT is envisaged to have an inclusive output stream of 2 kHz, of which 900 Hz is reserved for the single muon trigger. At 900 Hz, the single muon trigger efficiency is 22%. Apart from the cut on χ^2_μ, also the cuts on the track IP and p_T can be raised to reduce the output rate further. Table 6.6 contains the cut settings and relative trigger efficiencies for two different signal samples. As is seen from the table, the single muon trigger is relatively more efficient for tracks with higher p_T and IP.

Hence, by throttling the output rate down to 900 Hz, the single muon trigger output can be directly included in the HLT output stream, providing an independently generated, inclusive selection containing B decays with improved tagging from the triggered muon.

6.4 Muon Trigger Performance

As expected, the single muon and two dimuon triggers have large overlaps. For example, many events containing a dimuon with high invariant mass are also accepted by the single muon trigger. By combining the generic dimuon trigger, the specific J/ψ mass dimuon trigger and the single muon trigger, the overlap can be determined both for signal and

Signal Sample	IP cut (mm)	p_T cut (GeV)	χ^2_μ cut	ϵ (%)
IP_{MC} >0.15 mm, $p_{T\ MC}$ >2.3 GeV	0.15	2.3	3.3	22
IP_{MC} >0.25 mm, $p_{T\ MC}$ >3.0 GeV	0.25	3.0	4.0	41

Table 6.6: Single muon trigger efficiencies ϵ at 900 Hz trigger output rate for two different signal samples, selected on MC truth IP and MC truth p_T of the semileptonic muon in $B_s^0 \to D_s^{\mp} K^{\pm}$ decays. The cuts on IP, p_T and χ^2_μ for reconstructed tracks are listed.

minimum bias events.

6.4.1 Minimum Bias Retention and Overlap Bandwidth

With the three muon triggers combined, the χ^2_μ, p_T and IP cuts for the individual triggers and the dimuon J/ψ mass window are adjusted such that the retention of the combined trigger does not exceed 5.6×10^{-3}, corresponding to the 5.6 kHz L1 output rate which is reserved for inclusive muon triggers with the input of 1 MHz L0 accepted events.

Trigger Type	N Accepted Events	Rate (kHz)
Min.bias × L0	44017	1000
Dimuon General	30	0.68±0.12
Dimuon J/ψ Mass	132	3.00±0.26
Single-muon	102	2.32±0.23
Overlap	19	0.43±0.10
Total	241	5.48±0.35

Table 6.7: Accept rates of the individual muon triggers relative to the input rate of 1 MHz of minimum bias events accepted by the L0 trigger. On the bottom, the overlap and total output rate are listed. The uncertainties on the rates originate from the limited statistics on the minimum bias events.

Using the parameters from the analysis of stand-alone muon trigger performance, the individual triggers are tuned to their required retentions. The settings listed in Tables 6.3, and 6.4 are applied, resulting in the minimum bias accept rates listed in Table 6.7. Depending on the desired composition of the output event stream, more bandwidth can be allocated for particular triggers.

6.4.2 Combined Muon Trigger Performance

To determine the combined muon trigger performance, offline selected events are used for the benchmark channels listed in Section 1. The T-tracking was running within

the software packages, and using data according to the release versions mentioned in Section 5.5. It must be noted that the following performance figures refer to the muon trigger algorithms alone, without taking the performance of the generic L1 algorithm into account.

To quantify the performance benefit from using the T-tracking algorithm, two types of muon reconstruction are compared.

1. Muon+VELO: tracks in the muon detector are matched to L1-VELO tracks.

2. Muon T-Tracking: tracks in the muon detector are used to search for track continuations in the T stations. Subsequently, tracks are matched to L1-VELO tracks.

Both triggers are set to a retention of 5.6×10^{-3} by adjusting the mass window of the dimuon J/ψ trigger. The width of the mass window are 440 and 300 MeV for the Muon+VELO and T-tracking triggers, respectively.

For the efficiency determination, three different types of offline selected signal events are used, each of them addressing a specific muon trigger type.

- $B^0 \to \mu^+\mu^- K^*$ decays are used to determine the efficiency of the generic dimuon trigger. The dimuon mass of this decay mode covers a wide range, limited by the mass difference of the B^0 and K^* to 4.4 GeV.

- $B^0 \to J/\psi(\mu^+\mu^-)K^0_S$ decays are used to determine the efficiency of the dimuon J/ψ mass trigger.

- $B^0_s \to D^\mp_s K^\pm$ decays with a semi-leptonic decay from the opposite side B are selected by requiring a high p_T, high IP muon, regardless of the decay final state. These events are used to determine the single muon efficiency.

Table 6.8 contains results for the three event types discussed above. Efficiency figures are given for triggers based on the Muon+VELO and Muon T-Tracking algorithms for muon reconstruction. From the table, a clear performance gain at a retention of 5.6×10^{-3} by application of the Muon T-Tracking algorithm is seen, resulting in equal or higher trigger efficiencies for all selected decay channels. It should be noted that the quoted efficiencies do not include the generic L1 performance, the figures apply to the specific muon triggering algorithms only.

The improvements for $B^0 \to J/\psi(\mu^+\mu^-)K^0_S$ originate from the improvement in the p_T determination, while it does not suffer from inefficiencies in the VELO matching. $B^0 \to \mu^+\mu^- K^*$ does not gain, since the VELO is required anyway in the determination of the track IP. $B^0_s \to D^\mp_s K^\pm$ also requires a VELO track by definition, but still improves by inclusion of the T stations, through a more efficient reconstruction of the highest p_T muon track.

Decay channel	$B^0 \to \mu^+\mu^- K^*$	$B^0 \to J/\psi\,(\mu^+\mu^-) K^0_S$	$B^0_s \to D^\mp_s K^\pm$
Offline selected events	1217	29935	650
	Muon+VELO Trigger		
Triggered events:	625	15755	280
Relative efficiency:	51±2%	53±1%	43±6%
	T-Tracking Trigger		
Triggered events:	621	18125	307
Relative efficiency:	51±2%	61±1%	47±6%

Table 6.8: Combined muon trigger performance for various B decay channels at a retention of 5.6×10^{-3}. Efficiencies are given for a muon trigger using muon and L1-VELO tracks only, and a muon trigger including the T-tracking algorithm. The errors on the efficiencies result from the limited statistics. For $B^0_s \to D^\mp_s K^\pm$ decays, the event selection is described in 6.3.3.

6.5 Summary and Discussion

In this chapter, the application of the T-tracking algorithm in a L1 trigger is presented. The algorithm, described in the previous chapter, is used to search for particle tracks and reconstruct their momentum vector.

Online T-Tracking Algorithm

Starting points for a track search are provided by the muon or VELO detectors. The algorithm does not use data from the TT station upstream of the magnet, and uses binary channel hit data of the T stations. This results in a limited data volume which must be shipped to, and processed by, the trigger processors.

The momentum of reconstructed tracks is estimated using the relatively simple p_T-kick method. Here, the magnetic field is approximated by a singular field at z_f, with an identical integrated field strength $\int B \, \mathrm{d}l$. Track deflection is instantaneous and takes place at the focal plane. Using this method, the accuracy of the momentum estimate is about 9% for tracks found in the T stations, improving to 3% or better when a VELO track is attributed to the particle track.

The T-tracking algorithm is robust and simple. It is tolerant to detector misalignments up to the mm scale, through the use of binary hit information. The application of the p_T-kick method for particle momentum measurement makes the algorithm insensitive to the exact shape of the magnetic field. Furthermore, the T-tracking algorithm is not very sensitive to the settings of its parameters.

The Generic L1 Trigger and L1 Trigger Confirmation

30 kHz of the total 40 kHz L1 output rate is reserved for a generic trigger, the remaining 10 kHz is reserved for inclusive triggers. The generic L1 trigger is sensitive to many B decay modes, providing input for the exclusive selection algorithms of the HLT. The current L1 trigger implementation uses VELO-TT tracking for the track momentum estimate. The online T-tracking is capable of providing a momentum estimate with higher precision for L1-VELO tracks. The efficiency for $B_s^0 \to D_s^{\mp} K^{\pm}$ events is 56(61)% at 30(40) kHz output rate, equalling the L1 performance quoted in Ref. [28]. The performance is achieved without TT data in the L1 trigger, but by inclusion of binary hit data on the T station channels.

When using the T-tracking algorithm to re-execute the L1 algorithm with a better momentum estimate on events accepted by the current L1 trigger, the event rate is reduced from 40 to 23 kHz, while conserving 90% of the signal events. This reduces the load on the subsequent HLT trigger level, leaving more computing resources for the reconstruction of the remaining events.

Online Muon Reconstruction and Muon Triggering

An inclusive sample containing B and J/ψ decays with high statistics is indispensable for the unbiased lifetime analysis of B decays, the determination of systematic effects

and proper calibration of the detector. A muon trigger is instrumental in the acquisition of such a sample.

Through invariant mass reconstruction from two muon tracks, events containing a dimuon B or J/ψ decay are triggered. Additionally, by leveraging the large 10% branching ratio of $B \to \mu X$, a sample rich on B decays is acquired by triggering on single muons with significant IP and high p_T.

Using tracks from the muon detector as a starting point, the T-tracking algorithm is used to reconstruct muon tracks in the T stations online, and subsequently match L1-VELO tracks to the muon trajectories.

Separate trigger algorithms for single muons, generic and J/ψ specific dimuon invariant masses act on the collection of reconstructed muon tracks. An inclusive muon trigger combining these three algorithms is constructed. The trigger input consists of 1 MHz L0 accepted events, the output is restricted to the 5.6 kHz L1 output bandwidth reserved for an inclusive trigger using muons. Trigger efficiencies for the following decay channels are obtained using a combined muon trigger:

Channel	Efficiency
$B^0 \to \mu^+\mu^- K^*$	51±2%
$B^0 \to J/\psi\,(\mu^+\mu^-)K^0_S$	61±1%
$B^0_s \to D^\mp_s K^\pm$	47±6%

By applying the T-tracking algorithm, relative improvements of 15% and 10% for $B^0 \to J/\psi\,(\mu^+\mu^-)K^0_S$ and $B^0_s \to D^\mp_s K^\pm$ channels are obtained with respect to a muon trigger using the VELO and muon detectors only. Substituting the trigger efficiencies quoted above for the L1 trigger efficiency used in Ref. [13], the muon trigger is expected to deliver annual yields of 200k and 4.4k events for $B^0 \to J/\psi\,(\mu^+\mu^-)K^0_S$ and $B^0 \to \mu^+\mu^- K^*$ events, respectively.

Through the robustness of the online muon reconstruction, the inclusive muon trigger could prove its value from the first day LHCb starts collecting data. Even without using information from the VELO detector in the dimuon trigger algorithm, it is possible to construct an unbiased dimuon J/ψ invariant mass trigger with a 2 kHz output rate and a 24% efficiency using the online muon reconstruction.

References

[1] S. W. Herb *et al.*, *Observation of a dimuon resonance at 9.5-gev in 400-gev proton - nucleus collisions*, Phys. Rev. Lett. **39** (1977) 252.

[2] E. Fernandez *et al.*, *Lifetime of particles containing b quarks*, Phys. Rev. Lett. **51** (1983) 1022.

[3] N. Lockyer *et al.*, *Measurement of the lifetime of bottom hadrons*, Phys. Rev. Lett. **51** (1983) 1316.

[4] ARGUS Collaboration, H. Albrecht *et al.*, *Observation of* B^0 - $\overline{B}^0$ *mixing*, Phys. Lett. **B192** (1987) 245.

[5] Particle Data Group Collaboration, S. Eidelman *et al.*, *Review of particle physics*, Phys. Lett. **B592** (2004) 1.

[6] BABAR Collaboration, B. Aubert *et al.*, *Measurement of the CP-violating asymmetry amplitude sin2β.*, Phys. Rev. Lett. **89** (2002) 201802.

[7] Belle Collaboration, K. Abe *et al.*, *Measurement of CP-violation parameter sin(2*ϕ_1*) with 152 million B anti-B pairs*, hep-ex/0308036, 2003.

[8] BaBar Collaboration, B. Aubert *et al.*, *Observation of direct cp violation in b0 –> k+ pi- decays*, Phys. Rev. Lett. **93** (2004) 131801.

[9] Belle Collaboration, Y. Chao *et al.*, *Evidence for direct cp violation in b0 –> k+ pi- decays*, Phys. Rev. Lett. **93** (2004) 191802.

[10] LHCb Collaboration, S. Amato *et al.*, *LHCb Technical Proposal*, CERN-LHCC/98-4, 1998.

[11] H Dijkstra, N. Tuning, and N. Brook, *Some remarks on systematic effects of the trigger and event generator studies*, CERN-LHCB-2003-157.

[12] BELLE Collaboration, K. Abe *et al.*, *Improved measurement of cp-violation parameters sin(2phi(1)) and |lambda|, b meson lifetimes, and b0 anti- b0 mixing parameter delta(m(d))*, Phys. Rev. **D71** (2005) 072003.

[13] LHCb Collaboration, R. Nobrega *et al.*, *LHCb Reoptimized Detector Design and Performance Technical Design Report*, CERN-LHCC/2003-030, 2003.

[14] M. Baak, *Private communication.*

[15] Ikaros I. Y. Bigi and A. I. Sanda, *Cp violation*, Camb. Monogr. Part. Phys. Nucl. Phys. Cosmol. **9** (2000) 1.

[16] A. Pilaftsis, R. Bernhard, K.I. Voronchev, T. Nakada, O. Schneider, and T. Hurth, *Joint lhcb/theory meeting*, LHCb week December 2005.

[17] CDF Collaboration, R. Bernhard *et al.*, *A combination of CDF and D0 limits on the branching ratio of* $b_s^0(d) \to \mu^+\mu^-$ *decays*, hep-ex/0508058, 2005.

[18] C.S. Lin, $b_s \to \mu^+\mu^-$ *at the tevatron*, Flavour in the era of the LHC, 3rd meeting, 2006.

[19] Greub, C., Ioannisian, A., and D. Wyler, *Effects of new physics in the rare decays* $b \to k$ *lepton+ lepton- and* $b \to k^*$ *lepton+ lepton-*, Phys. Lett. **B346** (1995) 149.

[20] A. Ali, P. Ball, L. T. Handoko, and G. Hiller, *A comparative study of the decays* $b \to (k,k^*)$ *l+ l- in standard model and supersymmetric theories*, Phys. Rev. **D61** (2000) 074024.

[21] P. Lefèvre and T. Pettersson, *The Large Hadron Collider: conceptual design*, CERN-AC-95-05-LHC, 1995.

[22] ATLAS Collaboration, W.W. Armstrong *et al.*, *ATLAS : Technical Proposal for a General-Purpose pp Experiment at the Large Hadron Collider at CERN*, CERN-LHCC/94-43, 1994.

[23] ALICE Collaboration, N. Ahmad *et al.*, *A Large Ion Collider Experiment - Technical Proposal*, CERN-LHCC/95-71, 1995.

[24] CMS Collaboration, *Technical Proposal*, CERN-LHCC/94-38, 1994.

[25] *Lhc-b: A dedicated lhc collider beauty experiment for precision measurements of cp-violation. letter of intent*, CERN-LHCC-95-5.

[26] R. Cimino *et al.*, *Can low energy electrons affect high energy physics accelerators?*, Phys. Rev. Lett. **93** (2004) 014801.

[27] LHCb Collaboration, S. Amato *et al.*, *LHCb Magnet Technical Design Report*, CERN-LHCC/2000-007, 1999.

[28] LHCb Collaboration, R. Nobrega *et al.*, *LHCb Trigger Technical Design Report*, CERN-LHCC/2003-031, 2003.

[29] M. Agari *et al.*, *The lhcb silicon tracker project*, CERN-LHCb-2004-051, 2004.

[30] LHCb Collaboration, P. Barbosa-Marinho *et al.*, *LHCb Inner Tracker Technical Design Report*, CERN-LHCC/2002-029, 2003.

[31] R.H. Hierck, *Optimisation of the LHCb detector*, Ph.D. thesis, NIKHEF, 2003, CERN-THESIS/2003-025.

[32] LHCb Collaboration, S. Amato *et al.*, *LHCb RICH Technical Design Report*, CERN-LHCC/2000-037, 2000.

[33] LHCb Collaboration, S. Amato *et al.*, *LHCb Calorimeter Technical Design Report*, CERN-LHCC/2000-036, 2000.

[34] LHCb Muon Detector Group, *Draft of the second addendum to the muon system technical design report*, CERN-LHCB-2004-116-MUON, 2004.

[35] LHCb Collaboration, P. Barbosa-Marinho *et al.*, *LHCb Muon Technical Design Report*, CERN-LHCC/2001-010, 2001.

[36] A. Satta, *Muon identification in the lhcb high level trigger*, CERN-LHCB-2005-071.

[37] LHCb Collaboration, P. Barbosa-Marinho *et al.*, *LHCb VELO Technical Design Report*, CERN-LHCC/2001-011, 2001.

[38] LHCb Collaboration, P. Barbosa-Marinho *et al.*, *LHCb online system Technical Design Report: Data acquisition and experiment control*, CERN-LHCC/2001-040, 2001.

[39] B. Jost, A. Barczyk, G. Haefeli, R. Jacobsson, and N. Neufeld, *1 mhz readout*, CERN-LHCB-2005-062.

[40] T. Sjöstrand, L. Lönnblad, and S. Mrenna, *PYTHIA 6.2: Physics and manual*, hep-ph/0108264, 2001.

[41] W. Blum and G. Rolandi, *Particle detection with drift chambers*, Berlin, Germany: Springer (1993) 348 p.

[42] R.M. van der Eijk, G. Gracia, M. Merk, W. Ruckstuhl, and O. Steinkamp, *Track reconstruction for lhcb*, CERN-LHCB-1998-045.

[43] LHCb Collaboration, P. Barbosa-Marinho *et al.*, *LHCb Outer Tracker Technical Design Report*, CERN-LHCC/2001-024, 2001.

[44] J. van Tilburg, *Track simulation and reconstruction in LHCb*, Ph.D. thesis, NIKHEF, 2005, CERN-THESIS/2005-040.

[45] H.A. Bethe, Phys. Rev. **89** (1953) 1256.

[46] W.T. Scott, Rev. Mod. Phys. **35** (1963) 231.

[47] J. Nardulli and N. Tuning, *A study of the material in an outer tracker module*, CERN-LHCB-2004-114.

[48] G. Corti and L. Shekhtman, *Radiation background in the lhcb experiment*, CERN-LHCB-2003-083.

[49] G. Charpak *et al.*, *The use of multiwire proportional counters to select and localize charged particles*, Nucl. Inst. and Meth. **62** (1968) 262.

[50] F. Sauli, *Principles of operation of multiwire proportional and drift chambers*, CERN-77-09.

[51] B. Bevensee, M. Newcomer, R. Van Berg, and H.H Williams, *Progress report on the development of a bipolar asic for the atlas transition radiation detector*, CERN ATLAS INDET-NO-080, 1994.

[52] Th.S. Bauer, I. Gouz, and L.B.A. Hommels, *Beam tests of lhcb outer tracker prototypes in 2000*, CERN-LHCB-2001-011.

[53] L.B.A. Hommels, I. Gouz, and G.W. van Apeldoorn, *Beam tests of lhcb outer tracker prototypes in 2000*, CERN-LHCB-2001-098.

[54] G.W. van Apeldoorn *et al.*, *Beam tests of final modules and electronics of the lhcb outer tracker in 2005*, CERN-LHCB-2005-076.

[55] A. Romaniouk, *Choice of materials for the construction of the trt*, ATLAS-INDET-98-211, 1998.

[56] L.G. Christophorou *et al.*, *Fast gas mixtures for gas-filled particle detectors*, Nucl. Inst. and Meth. **163** (1979) 141.

[57] S. Bachmann, *Ageing studies for the straw tube detectors for the lhcb outer tracking system*, IEEE-NSS Conference Proceedings, 2004.

[58] *Atlas inner detector: Technical design report. vol. 2*, CERN-LHCC-97-17, 1997.

[59] *Hera-b: An experiment to study cp violation in the b system using an internal target at the hera proton ring. proposal*, DESY-PRC-94-02.

[60] COMPASS Collaboration, Guenter Baum *et al.*, *Compass: A proposal for a common muon and proton apparatus for structure and spectroscopy*, CERN-SPSLC-96-14.

[61] G.W. Apeldoorn, Th.S. Bauer, J.Steijger, and H.B. Dreis, *Aging studies of straw tube chambers*, CERN-LHCB-2001-003.

[62] V. Talanov, *Radiation environment at the lhcb inner tracker area*, CERN-LHCB-2000-013.

[63] G. Van Apeldoorn *et al.*, *Outer tracker module production at nikhef: Quality assurance*, CERN-LHCB-2004-078.

[64] S. Bachmann, *Specifications for the drift gas quality of the outer tracking system*, CERN-LHCB-2002-031.

[65] M. Merk *et al.*, *Optimizing the outer tracker near the y=0 region*, CERN-LHCB-2003-019.

[66] I. Gouz *et al.*, *Wire tension meter for the production of the lhcb outer tracker - commissioning and calibration*, CERN-LHCB-2004-034.

[67] M.Adamus, K.Brzozowski, P.Gawor, T.Marszal, A.Nawrot, K.Syryczynski, and M.Szczekowski, *First results from a prototype of the rasnik alignment system for the outer tracker detector in lhcb experiment*, CERN-LHCB-2002-016.

[68] J. Christiansen, *Requirements to the l0 front-end electronics*, CERN-LHCB-2001-014.

[69] J. Christiansen, *Requirements to the l1 front-end electronics*, CERN-LHCB-2003-078.

[70] D. Green, *The physics of particle detectors*, Camb. Monogr. Part. Phys. Nucl. Phys. Cosmol. **12** (2000) 1.

[71] V. Gromov and T. Sluijk, *Electrical properties of various types of straw tubes considered for the lhcb outer tracker*, CERN-LHCB-2001-001.

[72] B. Bevensee, F. M. Newcomer, R. Van Berg, and H.H Williams, *An amplifier shaper discriminator with baseline restoration for the atlas transition radiation tracker*, IEEE Trans. Nucl. Sci. **43** (1996) 1725.

[73] B. Bevensee, N. Dressnandt, N. Lam, F. M. Newcomer, R. Van Berg, and H. H. Williams, *Progress in development of the asdblr asic for the atlas trt*, Conference proceedings for the 5th Conference on Electronics for LHC Experiments, Snowmass, CO, USA (1999) 128.

[74] V. Gromov, T. Sluijk, A. Berkien, and E. van den Born, *Study of operational properties of the asdblr chip for the lhcb outer tracker*, CERN-LHCB-2000-054.

[75] M. Millmore, M. French, G. Hall, M. Raymond, and G.F. Sciacca, *Measurements of radiation hardened transistors from harris and dmill technologies*, http://www.imperial.ac.uk/research/hep/preprints/96-13.pdf.

[76] N. Dressnandt, N. Lam, F. M. Newcomer, R. Van Berg, and H. H. Williams, *Implementation of the asdblr straw tube readout asic in dmill technology*, IEEE Trans. Nucl. Sci. **48** (2001) 1239.

[77] Th. Bauer, A. Berkien, L. Hommels, A. Pellegrino, and T. Sluijk, *Noise studies with the lhcb outer tracker asdblr board*, CERN-LHCB-2004-117.

[78] V. Gromov, *Private communication*.

[79] Y. Gouz *et al.*, *Study of the global performance of an lhcb ot front-end electronics prototype*, CERN-LHCB-2004-120.

[80] H. Deppe, U. Stange, U. Trunk, and U. Uwer, *The otis reference manual*, Version 1.1, 2004.

[81] D. Wiedner and F. Eisele, *Aufbau der Ausleseelektronik fuer das aussere Spurkammersystem des LHCb-Detektors*, Ph.D. thesis, Ruprecht-Karls-Universitaet, 2004, CERN-THESIS-2005-051.

[82] U. Trunk, *Private communication*, 2006.

[83] F. Faccio, C. Detcheverry, and M. Huhtinen, *First evaluation of the single event upset (seu) risk for electronics in the cms experiment*, CMS-NOTE-1998-054.

[84] G. Cervelli, A. Marchioro, and P. Moreira, *A 0.13-mu-m cmos serializer for data and trigger optical links in particle physics experiments*, IEEE Trans. Nucl. Sci. **51** (2004) 836.

[85] G. Haefeli, A. Bay, F. Legger, and L. Locatelli, *Tell 1 : A common data acquisition board for lhcb*, Conference proceedings for the 9th Workshop on Electronics for LHC Experiments LECC 2003 , Amsterdam, The Netherlands , 29 Sep - 03 Oct 2003 129.

[86] G. Haefeli, A. Bay, F. Legger, L. Locatelli, and J. Christiansen, *Tell 1 specification for a common readout board for lhcb*, CERN-LHCB-2003-007.

[87] J. Nardulli, A. Pellegrino, and D. Wiedner, *Outer tracker level 1 data format*, CERN-LHCB-2005-0XX.

[88] P.V.C. Hough, *Machine analysis of bubble chamber pictures*, International Conference on High Energy Accelerators and Instrumentation, 1959.

[89] G. Barrand *et al.*, *GAUDI - A software architecture and framework for building HEP data processing applications*, Comput. Phys. Commun. **140** (2001) 45.

[90] P. Koppenburg, *DaVinci: The LHCb Analysis program*, `http://lhcb-comp.web.cern.ch/lhcb-comp/Analysis`, 2004.

[91] M. Cattaneo, *Brunel: The LHCb Reconstruction Program*, `http://lhcb-comp.web.cern.ch/lhcb-comp/Reconstruction/`, 2004.

[92] D.J. Lange, *The EvtGen particle decay simulation package*, Nucl. Instr. and Methods A **462** (2001) 152.

[93] I. Belyaev *et al.*, *Simulation application for the LHCb experiment*, physics/0306035, 2003.

[94] M. Cattaneo, *Boole: The LHCb digitization program*, `http://lhcb-comp.web.cern.ch/lhcb-comp/Digitization`, 2004.

[95] E. Polycarpo and J.R.T de Mello Neto, *Muon identification in lhcb*, CERN-LHCB-2001-009.

[96] J. Albrecht, *Private communication*, 2006.

[97] N. Tuning, *Matching velo tracks to l0 objects for l1*, CERN-LHCB-2003-039.

[98] G. Wilkinson, *Strategies for combating systematics at lhcb*, CERN-LHCB-2005-078.

[99] F. Teubert, I.R. Tomalin, and J. Holt, *The lhcb level-2 trigger*, CERN-LHCB-1998-047.

[100] C. Jacoby and T. Schietinger, *Level-1 decision algorithm and bandwidth division*, CERN-LHCB-2003-111.

Summary

High precision measurements of charge-parity (CP) symmetry violation enhances the knowledge of the mechanisms responsible for the observed dominance of matter over antimatter in the universe.

The Large Hadron Collider (LHC), a powerful pp collider, is foreseen to start operation in 2007. It will be a copious source of $b\bar{b}$ quark pairs, offering an excellent facility to study CP symmetry violation in the B meson system. Situated at the LHC, the LHCb experiment is dedicated to measure B meson decay with high statistics. Its primary goals are the establishment of CP violation parameters with high precision, and the study of rare B meson decays to look for physics processes beyond the Standard Model.

The production of $b\bar{b}$ quark pairs at the LHC is concentrated in small cones around the beam directions. Optimising $b\bar{b}$ acceptance with respect to detector cost, the LHCb detector is designed as a single-arm spectrometer, covering 300 and 250 mrad in the x-z and y-z planes, respectively.

To separate pp collisions containing a B meson from background events, use is made of two characteristics of the B meson: its high mass, of above 5 GeV, and its relatively long lifetime, exceeding 1.5 ps. With a Lorentz boost of about $\beta\gamma \simeq 15$, the typical distance between B meson production and its decay is about 8 cm. Following from its large mass, the tracks of B meson decay particles have large opening angles, resulting in an Impact Parameter (IP) up to a few mm.

The separation of background and signal events profits from high-precision measurements of the B meson mass and lifetime. Both properties are reconstructed using the tracking system consisting of the VELO, TT and T stations.

The VELO detector is installed around the interaction point and is used to reconstruct the position of decay vertices with few tens of microns resolution. The momentum of B meson decay particles is estimated from the particle track slopes before and after passing through a vertically oriented 4 Tm dipole field. In front of the magnet, the Trigger Tracker (TT) station is installed, the T stations T1, T2 and T3 cover the main tracking volume behind the magnet.

Individual T stations consist of two detectors. The region close to the beampipe, where particle fluxes are highest, is covered with a silicon strip detector, the Inner Tracker (IT). The greater part of the T stations is covered with a gas-filled multiwire

proportional detector, the Outer Tracker (OT). The TT station is built using IT technology exclusively.

To reach the required track momentum resolution of 0.6% for momenta up to 150 GeV/c, the OT and IT detectors in a single T station should introduce less than 3% of a radiation length X_0 into the acceptance, and have a resolution better than 212 μm on individual measurements. For the IT, the strip pitch is 198 μm, easily exceeding the resolution requirement.

For the OT, the resolution is obtained with drift detectors filled with an argon-based drift gas at atmospheric pressure. An optimal trade-off between channel size, choice of drift gas, and signal collection time resulted in a 5.25 mm pitch between 25 μm diameter anode wires, which are surrounded by conductive straw tubes with an inner diameter of 4.9 mm. With a drift gas composed of Ar(70%)-CO_2(30%), operated at 1600 V anode voltage, the resolution is better than 200 μm, the drift time accounts 41 ns and the single straw tube efficiency is >99% for the central 3.6 mm of the straw tube. The resulting gas gain of about 7×10^4 is an optimum between high channel resolution and high efficiency, and accelerated detector ageing.

The cathode material was selected by subjecting candidate materials to extensive ageing tests. The OT detector operates in regions with particle fluxes exceeding 60 kHz cm^{-2}, accumulating an integrated dose up to 100 krad in 10 years of operation. The particle flux and the gas gain result in an expected deposit of 1.3C per cm straw tube in the hottest regions of the OT. From the tests, Kapton XC foil emerged as the preferred cathode material.

For robustness of operation, detector maintainability, and ease of production, it was decided to build the OT layers in the T stations out of modules. A single module is built from two halves, each containing a straw tube monolayer. A module is mechanically stable, gas tight and capable of stand-alone operation. During and after production, many properties of individual channels and module (sub)assemblies are tested to ensure proper operation once installed in the experiment. For occupancy reasons, straw tubes are separated at the $y = 0$ plane, limiting the maximum tube length to 2.4 m. Modules are individually equipped with readout electronics at both ends.

The amplification and shaping of the straw tube signals is performed by the radiation tolerant ASDBLR preamplifier. It features 7 ns peaking time, and low intrinsic noise of 2000 electrons RMS. Its active baseline restoration circuitry limits the deadtime to 20-40 ns, making it particularly suitable for the OT readout. Due to their length, the straw tubes must be considered as transmission lines. Consequently, proper termination is mandatory to avoid spurious responses due to reflected pulses.

The ASDBLR signals are digitised by the OTIS Time-to-Digit Converter, a custom development for the LHCb OT. The OTIS contains necessary buffering and logic for the Level-0 (L0) trigger, reducing the volume of the data shipped off-detector.

Upon the readout of L0 accepted events, the primary vertex and high-IP tracks are reconstructed using data from the VELO detector. To avoid event selection based on

low momentum tracks faking a high IP, track momentum information is required.

In the readout system, bandwidth for shipping data towards the trigger algorithm is limited, allowing for the transfer of binary hit data of T station channels only. To use this information for track momentum measurement, an online tracking algorithm, T-tracking, was developed.

Besides efficient and precise track momentum measurement, the T-tracking execution time must be within a few ms trigger time budget and it must be robust with respect to detector inefficiencies and an imperfect detector alignment.

The requirements are met by a simple algorithm, searching for straight tracks in the T-stations, using track segments from the VELO and muon detectors as a starting point. The T-tracking algorithm is based on the Hough transform: binary channel hits are parametrised by their slope with respect to a seed point, generated from VELO or muon track segments. By application of a clustering algorithm on the global collections of OT and IT hits in the x-z plane, and subsequently in the y-z plane, continuations of VELO or muon tracks in the T-stations are found, greatly improving the estimate of their momentum.

From Monte-Carlo studies using $B_s^0 \to D_s^{\mp} K^{\pm}$ events, the algorithm performance is assessed. The averaged efficiency for finding continuations of VELO tracks is 90% for $p_T = 0.8$ to 10 GeV. The typical momentum resolution is 1.8%. The average execution time of the current algorithm implementation is 38 ms per event, but a large reduction of the execution time is expected by optimisation of the algorithm code for its designated task.

In the LHCb trigger, the 2 kHz output bandwidth is divided in about 300 Hz for the exclusive selection of B decays, and 1.5 kHz for an inclusive data stream including triggers on single- and dimuons. An inclusive data sample with high statistics is indispensable for the unbiased lifetime analysis of B decays, the determination of systematic effects and detector calibration.

The T-tracking algorithm is applicable in both trigger types. When used in the exclusive trigger to search track continuations of VELO tracks with a high IP, the performance is similar to the current Level-1 (L1) trigger. When combining the L1 trigger and T-tracking, the output rate is reduced by 43% while conserving 90% of the signal events.

When using the T-tracking for online muon reconstruction, gains in selection efficiency up to 15% are obtained for benchmark B decay channels containing single- or dimuons, independent of the exclusive trigger performance for these channels. The increase of the trigger robustness when including the T-tracking is illustrated by the efficiency of a dimuon J/ψ trigger: when VELO data is omitted, 60% of the dimuon trigger performance is conserved by using the muon and T-station detectors only.

Through its efficiency and robustness, including the T-tracking in the trigger could prove its value from the startup phase of the LHCb experiment onwards.

Samenvatting

Het met hoge precisie meten van de breking van Lading-Pariteit symmetrie (CP) kan meer inzicht verschaffen in de mechanismen die verantwoordelijk zijn voor het geobserveerde exces van materie ten opzichte van anti-materie in het heelal.

In 2007 zal de *Large Hadron Collider* (LHC) in werking treden. In de proton-proton botsingen van deze krachtige versneller zullen $b\bar{b}$ quarkparen in groten getale geproduceerd worden, wat een uitstekende gelegenheid biedt om de schending van CP symmetrie in het B meson systeem te meten. Eén van de aan de LHC verbonden experimenten is LHCb, ontworpen om het verval van het B meson met hoge statistiek te bestuderen. Hierdoor kunnen de variabelen die CP schending karakteriseren met ongeëvenaarde precisie worden vastgelegd. Verder zouden door het bestuderen van zeldzame vervalsmodi van B mesonen fysische processen die buiten de de beschrijving van het standaardmodel vallen geobserveerd kunnen worden.

Aan de LHC worden de meeste $b\bar{b}$ quarkparen onder een kleine hoek met de bundellijn geproduceerd. Hierdoor is de LHCb detector ontworpen als een eenzijdige spectrometer. De openingshoeken van de detector bedragen respectievelijk 300 en 250 mrad in het x-z en y-z vlak.

Pp botsingen waarin een B meson is gevormd moeten worden onderscheiden van botsingen waarbij dat niet het geval was: de achtergrond. Hiervoor worden twee karakteristieke eigenschappen van het B meson gebruikt, namelijk de lange levensduur van > 1.5 ps en de grote massa van > 5 GeV. De bundelenergie van de LHC zorgt ervoor dat B mesonen een Lorentz-*boost* faktor van $\beta\gamma \simeq 15$ krijgen, door de lange levensduur bedraagt de afstand tussen productie en verval gemiddeld 8 cm. De grote massa van het B meson zorgt voor grote hoeken tussen de onderlinge sporen van deeltjes afkomstig uit het B verval. Samen met de grote vervalsafstand zorgt dit ervoor dat de *Impact Parameter* van deze sporen tot enkele millimeters kan oplopen.

Door de massa en levensduur van het B meson met hogere precisie te reconstrueren kan de achtergrond beter worden onderdrukt. Beide grootheden worden in LHCb gemeten met systemen voor spoorreconstructie: de VELO, TT en T detectoren. De VELO bevindt zich vlak om het punt waar de bundels kruisen. Hierdoor kan de positie van de pp botsing, en daarmee ook de vervalsafstand van het B meson, binnen enkele tientallen microns nauwkeurig worden vastgelegd. De massa van het B meson wordt gereconstrueerd uit de impuls van de vervalsproducten. Door de richting van

de deeltjessporen te meten voor en na passage door een magnetisch dipoolveld met een integrale sterkte van 4 Tm, kan de impuls worden berekend. Hiervoor zijn de VELO en *Trigger Tracker* (TT) detector vóór de magneet geplaatst, en zijn de planaire T-detectoren T1, T2 en T3 achter de magneet opgesteld.

In elke T-detector is een *Inner Tracker* (IT), een silicium-strip detector, in het gebied rond de bundelpijp geplaatst waar de deeltjesflux het hoogst is. Het grootste oppervlak van de T-detectoren wordt bedekt door de *Outer Tracker (OT)*, een gasgevulde proportionele teller. De TT detector is uitsluitend uit silicium detectoren opgebouwd.

Om de vereiste 0.6% impulsresolutie voor impulsen tot 150 GeV/c te halen, mag de dikte van de OT en IT in een T-detector het equivalent van 3% stralingslengte niet overschrijden, en is een plaatsresolutie van 212 μm voor individuele metingen een vereiste.

In de IT wordt dit bereikt middels strips met een onderlinge afstand van 198 μm. De OT voldoet aan de eisen door gebruik te maken van een Ar(70%)-CO_2(30%) mengsel als telgas op nominale druk. Als compromis tussen de keuzes voor het telgas, de responstijd en afmetingen en afstand tussen de kanalen is gekozen voor 25 μm dikke anodedraden op een onderlinge afstand van 5.25 mm, omgeven door cylindrische cathodes, 'rietjes', met een inwendige diameter van 4.9 mm. Met een anodespanning van 1600 V is de plaatsresolutie beter dan 200 μm en de responstijd 41 ns. Hierbij is de efficiëntie van een enkel kanaal >99% binnen een straal van 1.8 mm van de anodedraad. De gasversterking bedraagt 7×10^4, wat een compromis is tussen een hoge efficiëntie en resolutie enerzijds, en versnelde detectorveroudering door stralingsschade anderzijds.

Het materiaal voor de cathode is geselecteerd op basis van zijn stralingbestendigheid. Immers, in het experiment kan de deeltjesflux 60 kHz cm^{-2} bedragen, wat overeenkomt met een ladingsdepositie van 1.3 C in 10 jaar per strekkende centimeter van een rietje. Daarbij kan de totale dosis tijdens de looptijd van het experiment oplopen tot 100 krad. Uit de tests kwam Kapton XC als beste materiaal naar voren.

Met het oog op onderhoud, eventuele reparaties en de mogelijkheden voor massaproductie is gekozen voor een modulair ontwerp van de OT. Een module is gebouwd van twee helften, elk uitgerust met een enkele laag rietjes. Een module is een onafhankelijke detector; gasdicht en mechanisch stabiel. Tijdens de productie procedure worden individuele kanalen en gehele modules onderworpen aan een aantal tests, om een correcte werking te garanderen als ze eenmaal in het experiment zijn opgenomen.

De verdeling van deeltjesflux in het experiment maakt een onderbreking van de rietjes halverwege de module noodzakelijk. Daardoor zijn beide einden van de modules uitgerust met uitleeselektronica. De ASDBLR zorgt voor de versterking en bewerking van de signalen afkomstig van de anodedraden. Deze voorversterker heeft een integratietijd van 7 ns en een laag ruisniveau van 2000 electronen RMS. Dankzij de geïntegreerde circuits voor nulniveau-herijking blijft de dode tijd beperkt tot 20-40 ns. Individuele kanalen moeten door hun grote lengte beschouwd worden als transmissielijnen. Een goede afsluiting aan minstens één zijde is noodzakelijk om valse

signalen van reflecties te voorkomen. De OTIS, een speciaal voor de OT ontwikkelde chip, meet de aankomsttijd van ASDBLR signalen. Ook zijn de voor de *Level-0* (L0) noodzakelijke geheugens en logische schakelingen geïntegreerd in de OTIS, wat de hoeveelheid te transporteren gegevens aanzienlijk vermindert.

Van de door de L0 geselecteerde botsingen wordt in de volgende selectiestap de locatie van de primaire botsing en sporen met een hoge IP gereconstrueerd. Om te vermijden dat botsingen geselecteerd worden op basis van sporen van deeltjes met een lage impuls maar een schijnbaar hoge IP, is impulsinformatie in dit stadium noodzakelijk. Met gebruikmaking van de T-detectoren is een nauwkeurige impulsmeting zeer goed mogelijk.

In het uitleessysteem van de detector is beperkte bandbreedte ingeruimd om de selectiesystemen te voorzien van gegevens. Voor de T-detectoren heeft dit tot gevolg dat van kanalen slechts de binaire respons gebruikt kan worden: een kanaal is òf wel, òf niet geraakt door een deeltje. Om met deze beperkte gegevens de impuls van een geladen deeltje te kunnen bepalen is het *T-tracking* algoritme ontwikkeld. Behalve een hoge efficiëntie voor spoorreconstructie en een hoge nauwkeurigheid voor de impulsmeting moet het algoritme binnen een tijdbudget van ettelijke millisecondes kunnen opereren, en tolerant zijn voor inefficiënties en uitlijnfouten van de detector. Hierdoor is gekozen voor een eenvoudig algoritme: vanuit reeds gevonden sporen in de VELO en/of muon detectoren wordt gezocht naar een bijbehorend recht spoor in de drie T-detectoren. Het hart van het algoritme wordt gevormd door de z.g. Hough-transformatie. In dit geval worden de actieve kanalen geparametriseerd door hun richting ten opzichte van een startpunt. Dit startpunt is berekend vanuit sporen in de VELO of muon detectoren. Door in de verzamelingen van geraakte OT en IT kanalen te zoeken naar groepen met overeenkomstige parameters, eerst in het x-z vlak, daarna in het y-z vlak, kunnen voortzettingen van sporen worden gevonden, waarna de impuls binnen 9% nauwkeurig kan worden bepaald.

Met behulp van simulaties van botsingen waarbij B meson verval optreedt, o.a. het $B_s^0 \rightarrow D_s^{\mp} K^{\pm}$ verval, zijn de prestaties van de T-tracking gemeten, waarbij gebruik gemaakt is van met behulp van VELO sporen bepaalde startpunten. Voor deeltjes met een transversaal momentum p_T tussen 0.8 en 10 GeV is de gemiddelde kans dat ze correct teruggevonden worden 90%. Daarbij bedraagt de impulsresolutie 1.8%. Gemiddeld heeft het algoritme 38 ms per botsing nodig om de reconstructie te voltooien. Echter, grote snelheidsverbeteringen zijn te verwachten als de implementatie van het algoritme wordt toegesneden op zijn specifieke taak.

De uiteindelijk beschikbare bandbreedte voor geselecteerde botsingen is 2 kHz. Hiervan is 300 Hz gereserveerd voor botsingen waarin een aantal specifiek geselecteerde B vervalsmodi optreedt. 1.5 kHz is gereserveerd voor een generieke selectie, vooral gebaseerd op enkele of dubbele muonen. Een grote collectie van generiek geselecteerde botsingen is onmisbaar voor calibratie, het bestuderen van systematische effecten en het

analyseren van B meson verval, zonder vooraf te selecteren op de leeftijd van het meson.

De T-tracking kan in beide selectiealgoritmes gebruikt worden. Voor de specifieke selecties, waarbij sporen in de T-detectoren gezocht worden uitgaande van sporen in de VELO detector, zijn de prestaties ongeveer gelijk aan het huidige *Level-1* (L1) algoritme. Als de huidige L1 implementatie gecombineerd wordt met T-tracking, blijft 90% van de botsingen met een B meson behouden, terwijl door verbeterde onderdrukking van de achtergrond de omvang van de selectie gereduceerd wordt met 43%. Als de T-tracking gebruikt wordt voor selecties gebaseerd op muonen, zijn verbeteringen tot 15% te verwachten voor de effectiviteit van de selectie van B vervalsmodi. Een bijkomend voordeel is dat de bedrijfszekerheid van deze selectie zeer hoog is. Dit wordt geïllustreerd met het feit dat 60% van de selectie-effectiviteit behouden blijft als slechts gebruik wordt gemaakt van de muon- en T-detectoren, waarbij gegevens van de VELO worden weggelaten.

Door zijn effectiviteit en bedrijfszekerheid kan het T-tracking algoritme zijn waarde bewijzen vanaf het moment dat het LHCb experiment in bedrijf zal worden genomen.

Dankwoord

Promoveren doe je niet alleen, en dat is maar goed ook. Zonder de hulp en steun van vele anderen was dit proefschrift er nooit gekomen, en ik wil graag iedereen die direct of indirect bijgedragen heeft hartelijk bedanken.

Allereerst ben ik natuurlijk veel dank verschuldigd aan Marcel Merk, mijn promotor. Zijn onvoorwaardelijke steun en vasthoudendheid heeft ervoor gezorgd dat ik vaak nog 'een tandje erbij kon zetten', ook als ik het zelf eigenlijk wel genoeg vond. Daarnaast is de gezonde mix van gedrevenheid, relativeringsvermogen, vrolijkheid en niet te vergeten plat *Mestreechs* de hoofdverdachte voor de fijne atmosfeer in de B-fysica groep, waar niet alleen ik van heb geprofiteerd.

Ook heb ik erg veel te danken aan Niels Tuning. Zonder de soms letterlijk dagelijkse begeleiding had dit proefschrift, met name de hoofdstukken 5 en 6, er heel anders uitgezien. De prima samenwerking, de discussies en gezamenlijke 'kwartiertjes' achter het beeldscherm hebben enorm bijgedragen aan mijn begrip van triggering in LHCb. Als neveneffect heb ik geleerd hoe met maximale efficiëntie en toch minimale zorgen met andermans programmatuur om te gaan. Een verdiende eerste vermelding als co-promotor is wel het minste wat hier tegenover kan staan.

Wat minder recent, maar zeker niet minder belangrijk is de samenwerking met Bert Koene geweest. Ik ben erg dankbaar voor de kans die ik gekregen heb om onder zijn begeleiding als projectleider aan het LHCb Outer Tracker project bij te dragen. Hierdoor heb ik de ontwikkeling van de Outer Tracker van dichtbij kunnen meemaken en deel kunnen nemen in allerlei samenwerkingsverbanden, binnen NIKHEF, in het experiment, en op CERN. Beide aspecten hebben ervoor gezorgd dat het twee zeer leerzame jaren zijn geweest.

Door het werk aan de Outer Tracker heb ik ook de weg op de begane grond en de eerste verdieping van het NIKHEF leren kennen. Gelukkig hebben Tom Sluijk en de zijnen altijd goed kunnen verbergen dat ik natuurlijk eigenlijk bij de tegenpartij hoorde. Zo waren ze altijd bereid om me uit te leggen hoe de electronica nou precies werkte, waardoor ik ook van hen veel heb kunnen opsteken, zowel in het lab als in de bundeltesten op CERN. Mede door hun enthousiasme en liefde voor het vak heb ik nog steeds geen partij kunnen kiezen...

On the frontier between physics and electronics, I owe much to our two Russian fellows: Vladimir Gromov and Youri Gouz. A substantial part of Chapter 4 is based on their work. Special thanks go to Youri, a true allround physicist, for his contribution to the Outer Tracker project and his pleasant company, especially during the OT beamtests at CERN.

Aan het werken op NIKHEF heb ik altijd veel plezier beleefd. De dagelijkse uitwisseling van zin en onzin binnen en buiten de B-fysica groep was voor de sfeer in ieder geval altijd zinvol. Hierdoor is promoveren veel minder een eenzame en solistische bezigheid gebleken dan vaak voorgesteld wordt.

Een belangrijk deel van mijn vrije tijd is opgegaan aan 'ontspanning door inspanning', en dankzij alle SKITSers heb ik geen seconde spijt van de vele trainingsuren in en om Amsterdam!

Tenslotte wil ik mijn ouders bedanken, niet alleen voor de hulp als er weer eens verhuisd moest worden, maar voor hun niet aflatende steun, interesse, geduld en vertrouwen.